Ph.D. Thesis

Anomalous atmospheric flows captured by multiple radiosonde sounding

- Strong local wind from Iga to Tsu and Atmospheric Rivers from Siberia to the Arctic -

“局地”と“極地”でのラジオゾンデを用いた直接観測から捉える極端気象現象

- 伊賀から津に吹く鈴鹿おろしと，シベリアから北極に流れる Atmospheric Rivers -

Graduate School of Bioresources
Mie University

Kensuke Komatsu

Jul 2018

Contents

General Introduction

Large gradient of a bottom boundary condition, such as local topography and sea surface temperature (SST), strongly influences on a behavior of upper atmosphere. The surface-driven upper atmosphere occasionally induces curious atmospheric phenomena. For example, the atmosphere flowing over a mountain range generates a severe wind storm at a leeward side. This is referred to as a downslope wind storm, and sometimes damages human living [e.g. Lilly and Zipser 1972]. A sea surface condition, such as a strong horizontal SST gradient formed at the front of the warm Kuroshio current, locally influences an atmospheric horizontal pressure gradient, and its resultant a lower tropospheric wind [e.g. Nishikawa et al. 2015]. These surface-driven atmospheric phenomena are within a small scale, because the horizontal scale of these surface conditions is also small. Although global-scale climatic assessment tends to ignore these small-scale phenomena as a 'noise' of large-scale atmospheric circulation, we must consider that small-scale phenomena driven by individual small-scale boundary conditions modifies larger-scale phenomena.

An in-situ observation is one of the most effective approach in order to clarify the structure and mechanism of a local atmospheric phenomena cooperated with a boundary condition. The radiosonde observation, which releases a balloon attached with a meteorological sensor, is one of the most straightforward method to measure an accurate vertical structure of the atmosphere. Although this observation provides us with the truth of atmospheric vertical condition by "a direct measurement", there are some shortcomings for fully measuring atmosphere driven by the horizontal gradient of surface conditions. Because the radiosonde sounding generally operates at a single site, the observed vertical

structure means just only a part of the atmospheric flows passed over the observation site, thus it is difficult to clarify the horizontal structure associated with the horizontal gradient of the surface conditions. To overcome this weakness, a multiple sounding by multiple sites or by moving the location with time from windward side to leeward side is an ideal method to capture the horizontal-vertical structure (Off course, it does not perfectly cover). Another approach is using reanalysis products and their dynamical downscaling by a regional numerical model. The reanalysis products are uniformly gridded dataset computed by a numerical model based on dynamical and thermodynamic equations and assimilated several observation data (ground base, ship, upper-air, satellite and etc.) [e.g. Dee et al. 2000]. Studies on climate change or large-scale atmospheric phenomena tend to use reanalysis datasets because these products contain a long range of data records. However, there are large uncertainly over the ocean and polar regions where routine observation network does not exist. In addition, the gird scales of many reanalysis are not sufficient to resolve a detail topography and sea surface condition such as strong horizontal SST gradient and existence of a sea-ice margin. The dynamical downscaling would bring about a solution to this problem, but the results estimated by the dynamical downscaling does not always replicate the true atmospheric state. Although their grid resolution recently tends to increase to finer one with the development of a computer, the reproducibility of the downscaling must be compared with in-situ observation. Therefore the knowledge of locally atmospheric structure driven by bottom boundary must be increased at time coming age of very high resolution simulations.

This thesis addressed two case studies by radiosonde observations related with bottom boundary. One is a special campaign of multiple radiosonde soundings to

a severe local atmospheric phenomenon, i.e., anomalous wind event called as "Suzuka-oroshi" in Japan. The other is anomalous moisture intrusion referred to as "Siberian atmospheric rivers" in the Arctic. The former was documented by a new method manipulated the multiple radiosondes which released in multiple sites to capture the horizontal-vertical structure of atmospheric flow over the mountain range. The latter was documented by multiple soundings released on the icebreaker traveling from an open-ocean to a thick ice zone in the Arctic where the observational evidence is scant. The thesis revealed hidden phenomena driven by their boundary conditions through in-situ observation cooperated with numerical modeling. The thesis aims to signify the importance of in-situ observation. The briefs of each chapter are presented as below for the help to the readers.

Chapter 1 presents a radiosonde observation method, consisting of simultaneous radiosonde observations at closely spaced multiple sites using balloons with varied buoyancies. This method was employed during a strong wind event (Suzuka-oroshi) on the lee side of the Suzuka mountain range, Japan, in order to derive the detailed horizontal-vertical structure of the wind as it crossed the mountains. Batches of six radiosondes were launched simultaneously from a line of four sites, using balloons with three different degrees of buoyancy. Four sites were 13 km apart along a 35-km-long transect roughly aligned with the prevailing wind. The observations documented two flow regimes: a downslope flow perpendicular to the mountain range, similar to a windstorm, and an unexpectedly strong low-level jet flowing parallel to the mountain range. The first regime was well simulated by a numerical experiment, but the second regime was not. These results and their conclusions were published in *Monthly Weather*

Review 144 [Komatsu and Tachibana, 2016].

Chapter 2 presents the radiosonde observation during the summer over the Arctic Ocean from an icebreaker moving poleward from an ice-free region, through the ice edge, and into a region of thick ice. We showed a new potential contributing process to the Arctic temperature increase, based on our direct observations and supporting numerical simulations and statistical analyses using a long-term reanalysis dataset. We refer to this new process as "Siberian Atmospheric Rivers (SARs)". Poleward upglides of SARs over cold air domes overlying sea ice provide the upper atmosphere with extra heat via condensation of water vapour. This heating drives increased buoyancy and further strengthens the ascent and heating of the mid-troposphere. This process requires the combination of SARs and sea ice as a land-ocean-atmosphere system, the implication being that large-scale heat and moisture transport from the lower latitudes can remotely amplify the warming of the Arctic troposphere in the summer. These results and their conclusions were published in *Scientific reports*, 8 [Komatsu et al. 2018].

References

Dee, D. et al., 2011: The era-interim reanalysis: configuration and performance of the data assimilation system. *Q. J. R. Meteorol. Soc.,* **137**, 553–597

Komatsu, K. K., V. A. Alexeev, I. A. Repina, and Y. Tachibana, 2018: Poleward upgliding Siberian atmospheric rivers over sea ice heat up Arctic upper air. *Scientific reports*, **8**, 2872

Komatsu, K. K., and Y. Tachibana, 2016: Two Types of Strong Local Wind Captured by Simultaneous Multiple-Site Radiosonde Soundings across a

Mountain Range. *Mon. Wea. Rev.,* **144**, 3915-3936

Lilly, D. K., and E. J. Zipser, 1972: The Front Range Windstorm of 11 January 1972 a Meteorological Narrative. *Weatherwise*, **25,** 56–63, doi: 10.1080/00431672.1972.9931577

Nishikawa, H., Y. Tachibana, Y. Kawai, M. K. Yoshioka, and H. Nakamura, 2016: Evidence for SST-forced anomalous winds revealed from simultaneous radiosonde launches from three ships across the Kuroshio extension front. *Mon. Wea. Rev.,* **144**, 3553-3567

Chapter 1. Two Types of Strong Local Wind Captured by Simultaneous Multiple-Site Radiosonde Soundings across a Mountain Range

1.1 Introduction

Radiosondes are one of the most accurate tools for observing the vertical structure of the atmosphere. For example, a single radiosonde sounding, recording a single atmospheric profile along its trajectory, is able to provide the propagation direction of a gravity wave [e.g., Vincent et al. 1997]. However, a single radiosonde sounding cannot provide the data needed to map two-dimensional airflows over a mountain range, such as the structure of a downslope wind. To construct such a map, the ideal observation program would be to launch many radiosondes simultaneously from a line of stations parallel to the prevailing wind that extends across a mountain range, including its windward and leeward sides. This scheme could provide a detailed profile of a narrow, mountain-induced strong wind in a vertical plane. In an attempt to realize this scheme, we launched six radiosondes simultaneously from a line of four closely spaced (~13 km apart) sites that was aligned with the wind direction, using a range of buoyancies at some sites to better sample the vertical space. The purpose of this paper is to document this observational method and its results, and to apply the results in an investigation of a local wind, the Suzuka-oroshi, by observational, numerical, and statistical approaches.

Previous observational studies of strong winds over a mountain range, such as downslope winds, have employed multiple direct observations by radiosondes, dropsondes, or airplanes in traverses across a mountain range. A famous study of this type which captured the flow over a mountain [Lilly and Zipser 1972] combined an airplane traverse with radiosonde launches from a single site on the

lee side of the Front Range of the Rocky Mountains. The resulting vertical-horizontal schematic map of a downslope windstorm is still recognized as exemplary. Later projects involving observations of orographic flow produced such maps on the basis of observation campaigns that included an airplane. For example, Jiang and Doyle [2004] used Global Positioning System (GPS) dropsonde and flight-level data to document the hydraulic jump associated with wave breaking in the eastern Alps during the Mesoscale Alpine Program. Doyle et al. [2005] similarly observed large-amplitude wave-breaking in Greenland during the Fronts and Atlantic Storm-Track Experiment, creating a three-dimensional model of the flow structure. The Terrain-induced Rotor Experiment combined in situ and airborne measurements to capture the vertical atmospheric structure in the Owens Valley of California, on the lee side of the Sierra Nevada [Grubišić et al. 2008; Wang et al. 2009]. However, the costs of aircraft, in particular, make such projects difficult to carry out. Although the combination of GPS dropsondes with airplanes is effective for delineating vertical-horizontal flow, the observations cost much more than those made by GPS radiosondes. We therefore designed a low-cost observation scheme based solely on GPS radiosondes.

Researchers have devised methods of manipulating balloon trajectories to investigate air flows across mountain ranges. Booker and Cooper [1965] pioneered the use of constant-volume superpressured balloons to investigate trajectories related to mountain waves. Vergeiner and Lilly [1970] used this method to capture part of the structure of a lee wave in the Front Range of the Colorado Rockies. They concluded, however, that constant-volume balloons were inferior to instrumented aircraft. Glenn Shutts introduced multiple sounding techniques that relied on control of balloon trajectories. During a field experiment

in the Welsh Mountains in October 1989, three radiosondes were launched at 10-minute intervals from a single station [Shutts et al. 1994]. The buoyancies of the three radiosondes were varied by inflating them with different amounts of helium. Shutts [1992] examined fluctuations in the ascent rates of the three radiosondes and compared them with ascent rates calculated with a non-hydrostatic mesoscale model to demonstrate the feasibility of using them to map lee wave structures. Shutts and Broad [1993] employed five radiosondes with different buoyancies to observe waves over the Lake District in northern England and constructed a map of the vertical velocity field from radiosonde and airplane observations. All of these studies used multiple sounding balloons launched from a single site. Avoiding the use of airplanes would require many radiosondes to be launched simultaneously from a line of stations across a mountain range parallel to the prevailing wind. To attempt such a program, we designed a method that can be described briefly as simultaneous multiple-site radiosonde observations with varied buoyancies. To provide wider horizontal coverage in the troposphere than done by Shutts et al. [1994], the method combines multiple soundings at a single station and multipoint sounding stations along a transect across a mountain range. Modern radiosondes with GPS receivers provide more accurate location data than those used by previous studies.

We conducted a successful pilot experiment using this method on 21 March 2010 in Japan, observing the local strong mountain wind called the Suzuka-oroshi [Yoshino 1975]. The area of our observational study, the Suzuka Mountains, is famous in Japan for the occurrence of strong local winds in winter. These are locally called Suzuka-oroshi, *oroshi* being a term for a strong, cold downslope wind. An *oroshi* is therefore similar to the Bora wind of eastern Europe [e.g.,

Smith 1987; Grisogono and Belušić 2009]. Owada and Harada [1978] suggested from a study of the orientation of wind-sculpted trees that the Suzuka-oroshi is a westerly lee wave over the Suzuka Mountains. Owada [1994] described the general features of the Suzuka-oroshi and reported that six different synoptic-scale weather patterns are associated with it. However, the mechanism, process, and vertical structure of the Suzuka-oroshi remain poorly known. For example, it is not clear whether the Suzuka-oroshi is similar to other typical downslope wind storms.

The first objective of this paper is to explain our radiosonde observation strategy. The second objective is to show its results in a detailed two-dimensional profile of a strong wind crossing a mountain range and to compare the results to those of an analogous numerical experiment. We show that simultaneous multiple-site radiosonde soundings can directly capture a downslope windstorm. We also show that the ascent rate of a radiosonde balloon can provide reliable estimates of the vertical wind direction through a comparison with estimates based on the changing slopes of observed potential temperature isentropes and estimates based on numerical experiments. In addition, our observations captured an interesting strong wind regime associated with a low-level jet, which was not anticipated. This paper describes the two-dimensional structure of this regime. The third objective is to discuss the synoptic conditions associated with the onset of the low-level jet regime. We describe our statistical investigation of climatological conditions associated with the low-level jet and compare these conditions with the synoptic conditions during our observations and with the results of a numerical simulation.

Section 1.2 of this paper describes the field experiment, our method, and the

resulting data. Section 1.3 shows examples of the flow structures captured by our method and presents a comparison with numerical experiments to clarify the observational results. Section 1.4 is a discussion of the results as informed by an additional statistical analysis. Section 1.5 presents our conclusions.

1.2 Observation method and targeted phenomena

a. Simultaneous multiple-site radiosonde observations with varied buoyancies

Our experimental method (Fig. 1.1) expands upon the multiple sounding method employed by Shutts et al. [1994], in which balloons with different buoyancies were launched at 10-minute intervals from a single site. At seven separate times during the same day, we launched six GPS radiosondes simultaneously at four sites: the Iga Research Institute of Mie University (IGA), the Aoyama-kogen Wind Farm (AOYAMA), the Experimental Farm of Mie University (FARM), and Mie University (UNIV) (Fig. 1.2). Ideally, the location and spacing of launching sites are determined by the horizontal scale or the wavelength of targeted phenomena. However, in the Suzuka Mountains the choice of launching sites is restricted by various requirements such as sufficient space for preparing and launching balloons, electrical power sources for radiosonde receivers, and authorization to conduct observations. It was impossible to set up a strictly linear array across the mountain range during our experiment. However, the four selected launching sites formed a roughly linear west-to-east transect about 35 km long with Mt. Kasatori in the center. During westerly or northwesterly synoptic winds, sites UNIV and FARM are on the leeward side of the mountains, IGA is on the windward side, and AOYAMA is at the crest of Mt. Kasatori. The distance between sites along the prevailing wind direction was extremely short, about 13 km. The transect was roughly parallel to the wintertime prevailing winds in this region. The topography around sites FARM and UNIV, on the leeward side, is nearly flat and thus local effects on the wind in the lower boundary layer were negligible.

In addition to the simultaneous launches at four sites, the amount of helium in

the balloons was varied to control the balloon trajectories and thus provide better coverage in the vertical plane of the transect. During our observations, we deployed three sizes of balloons: large, normal, and small. Their rates of ascent were fast, normal, and slow, respectively. We ensured that the buoyancy of each type of balloon was consistent at all launch sites by using a weight measurement scale. First we injected helium into the balloons, with radiosonde and parachute attached, inside a shelter until they reached neutral buoyancy. The balloons were then inflated further to a buoyancy of 1.0–1.2 kgf (1.0–1.2 × 9.8 N) for the fast balloons, 0.6–0.7 kgf for the normal balloons, and 0.5 kgf for the slow balloons. These settings were chosen empirically. Because it is difficult to measure accurately the weight lifted by a balloon, buoyancies could not be kept strictly constant for each size of balloon, but we were able to roughly control their rates of ascent. When launched simultaneously, the slower balloons were more strongly influenced by strong winds in the lower troposphere and moved farther downwind. The average ascent rates in the troposphere (<10 km) were 7.58 m s^{-1} (fast), 5.59 m s^{-1} (normal), and 4.78 m s^{-1} (slow) during our experiment.

Observations were made on 21 March 2010. The launch times and types of balloons are summarized in Table 1.1. Human errors led to some failures in data transmission after the balloon releases.

b. Construction of transect profiles

Because the balloon trajectories during each set of observations varied temporally and spatially depending on the wind direction, we projected the dataset from each radiosonde release onto a vertical plane parallel to the prevailing wind (Fig. 1.3). We determined the orientation of this plane subjectively by examining

all three-dimensional trajectories and identifying the plane that was in the middle of the trajectories. Figure 1.4 shows an example of this projection based on the trajectories shown in Fig. 1.3a. Each balloon's sounding line was determined from its position information (longitudes, latitudes, and elevations). We projected each balloon location (longitude and latitude) onto the chosen plane (Fig. 1.4a), then arranged the projected sounding lines into a 2D longitude–altitude section (Fig. 1.4b). Next, we constructed transect profiles interpolated by the triangulation method of Watson [1982] using Generic Mapping Tools [Wessel et al. 2013]. The degree of error in a vector variable (wind) depends on the orientation of the chosen plane, which affects the transverse and parallel components of the wind with respect to the plane. The scalar variables of temperature, relative humidity, and wind direction are unaffected by the choice of profile plane. We verified that the results were not sensitive to small changes in the orientation of the plane. Lacking other instrumental data to compare with the sounding data, we had to assume that atmospheric conditions did not change during the period of roughly 1 hour during which the balloons were ascending. The resulting profiles provided snapshots of the two-dimensional vertical and horizontal structure of meteorological variables defined by the several balloon trajectories in each radiosonde release (shaded area in Fig. 1.1).

c. Sounding data

We used radiosondes (RS-06G, Meisei Electric Co., Ltd., Japan) that record temperature, relative humidity, wind, and air pressure. The GPS receiver mounted on each radiosonde measured highly accurate longitudes, latitudes, and elevations. According to the manufacturer's specifications, the accuracies of GPS height and

pressure are ±5 m and ±1 hPa, respectively. Data were recorded at intervals of 1 s. To make the vertical resolution of the radiosonde data uniform, we averaged the data vertically over intervals of 20 m. In addition, we smoothed the data by the weighted running mean over 100-m intervals to remove high-frequency perturbations.

The structure of atmospheric vertical motion provides important information such as the structure of gravity waves and the location of hydraulic jumps. Although radiosonde trajectories do not indicate atmospheric vertical motions directly, we calculated vertical motions by the following procedure. First, we calculated the fluctuations in the balloon ascent rate, from which the atmospheric vertical motion can be deduced with considerable accuracy [e.g., Corby 1957; Reid 1972; Reeder et al. 1999]. We defined the simplified ascent rate (m s^{-1}) as $z_{i+1} - z_i$, where z_{i+1} and z_i are the (i+1)-th and i-th height measurements (meters) respectively. Because the height was also recorded at 1-s intervals, the ascent rate data yield the vertical displacement per second of the balloon. Then we calculated the ascent rate averaged over 20-m intervals and smoothed by the weighted running mean over 100-m intervals. Second, we calculated the anomaly of the ascent rate relative to the average ascent rate in the troposphere (altitude < 10 km) for each launch. Figure 1.5 shows examples of the smoothed and average ascent rates at two observation times for IGA and FARM. Note that we assumed here that the anomalies in the ascent rates represent the relative upward or downward motion compared with the mean ascent rate, rather than actual vertical motions. A method previously used to evaluate vertical velocity from sounding data is that of Wang et al. [2009], who estimated vertical velocities by subtracting the balloon rise-fall rate in still air from the actual rise-fall rate. That method is better for

estimating actual vertical velocity, because the rise-fall rate in still air includes the effects of changing air density with height. However, the rise-fall rate in still air is subject to uncertainty (e.g., in the drag coefficient and the balloon volume), and the method used by Wang et al. [2009] may not have been appropriate for our campaign because we had no parameters for calculating the rise-fall rate in still air. In this study we sought to deduce vertical motions by two independent ways: by the anomaly in the balloon ascent rate and by isentropic analysis. The structure of potential temperature in a vertical plane can be used to diagnose the trajectory of a particular air mass because the potential temperature within the air mass is conserved if diabatic heating is sufficiently small and the flow is steady. Because the air mass travels parallel to an isentropic surface if the flow is both steady and adiabatic, the ascent or descent of an isentropic surface provides the vertical displacement of an air parcel.

1.3 Results

a. Synoptic-scale atmospheric conditions and surface winds

Figure 1.6 displays the patterns of sea-level pressure on 21 March 2010, derived from the Japanese 25-year Reanalysis (JRA-25) / JMA Climate Data Assimilation System (JCDAS) [Onogi et al. 2007]. At 06 JST on 21 March, an intense cyclone located over the north-east side of Japan, nearly over Hokkaido islands. After that, the cyclonic system moved to far north-east and a high pressure system intruded to the Japan Sea in a configuration similar to the common winter sea-level pressure pattern around Japan known as "west high and east low," associated with winter monsoon winds (Fig. 1.6 b and c). The probability of a Suzuka-oroshi event was high because the synoptic conditions resembled those described by Owada [1994].

Besides the radiosonde sounding, we used observations of surface winds at Tsu and Mt. Kasatori to evaluate the occurrence of the Suzuka-oroshi (Fig. 1.2). The city of Tsu, where there is a meteorological station of the Japan Meteorological Agency (JMA), is commonly affected by the Suzuka-oroshi [Owada and Harada 1978]. At the peak of Mt. Kasatori, an instrumented tower records wind speed and direction at 25 m, 45 m, 60 m, and 75 m above the ground. The wind speed at the Tsu station and Mt. Kasatori strengthened suddenly between 0400 Japan standard time (JST, UTC+9) and 0500 JST (Fig. 1.7). The wind at Tsu was generally westerly from 0400 JST to 1200 JST and northwesterly from 1200 JST to 2400 JST. The maximum wind speed at Tsu, 13.0 m s^{-1}, was observed at 1650 JST during the latter period. Conversely, at Mt. Kasatori the maximum wind speed, with the largest vertical wind shear, was observed between 0400 and 0500 JST, after which the wind gradually abated until 1500 JST, then

intensified again.

b. Flow regimes

We constructed longitudinal profiles using the data from each of our seven radiosonde releases during the Suzuka-oroshi event of 21 March 2010. The profiles showed two distinct flow regimes during the course of the day, the first resembling that of a downslope windstorm and the second resembling that of a low-level jet. Figure 1.8 displays vertical profiles of wind speed and wind direction for each site in the two different flow regimes. At elevations below 2000 m in the first regime (Fig. 1.8a), wind speeds at the mountain top (AOYAMA) and in its lee (FARM, UNIV) were higher than on the upwind side of the mountain (IGA). This difference was greatest (17 m s^{-1}) at 1100 m elevation, where wind gusts at AOYAMA reached 36 m s^{-1}. The average wind direction was westerly (Fig.1.8b). In the second regime, wind speeds were nearly the same at all four stations below 3000 m, except at UNIV below 500 m, where the maximum speed reached about 19 m s^{-1} and the wind direction was northwesterly (Figs. 1.8c, 1.8d). The horizontal wind maps, when two flow regimes are observed, are depicted in Figure 1.9 which is constructed by 1-hour averaged surface wind recorded by meteorological stations of JMA. In the former regime (Fig. 1.9a), a relatively strong westerly wind region, over 6 m s^{-1}, expanded from Mt. Kasatori to the leeward side where UNIV and Tsu stations are located. In the latter regime (Fig. 1.9b), a strong north-westerly wind, over 10 m s^{-1}, observed at Tsu station although Tsu station was located on the leeside of Suzuka-Mountain range and wind speed of the windward side was relatively weak.

1) DOWNSLOPE WINDSTORM

The profile at 0530 JST depicts a structure similar to that of a downslope windstorm (Fig. 1.10). During this radiosonde sounding, the surface wind was strong at both stations, and the instrumented tower at Mt. Kasatori recorded a large vertical wind shear between 25 m and 75 m (Fig. 1.7). The prevailing wind was southwesterly, so the vertical structure was profiled from southwest to northeast (Fig. 1.3a). Figure1.10a shows the potential temperature and the anomalies in ascent rate along this profile plane. Some of the balloon trajectories crossed, but on the whole our launching strategy succeeded in covering an expanded area of the atmospheric field in detail.

Figure 1.10a shows that the isentropic surfaces inferred from our data formed a wave pattern in the troposphere. It is noteworthy that the ascent rate anomaly along the sounding line, interpreted as the relative vertical velocity, agrees with the flow structure expected from the curvature of isentropes. For example, a strong negative ascent rate anomaly was inferred above the top of Mt. Kasatori that extended up to the 294 K isentropic surface. The fact that isentropes from 292 K to 300 K were consistently concave downward over the top of the mountains is consistent with the negative ascent rate anomaly. This correspondence of ascent rate anomalies and isentropic slopes was also apparent in other areas. The strong positive ascent rate anomalies along the FARM-Fast balloon trajectory from 292 K to 300 K are consistent with the upward slope of the isentropes on the leeward side of the mountains, which signify the presence of updrafts there. At higher altitudes, for example along the 312 K contours, this same consistency was apparent. The fact that the slopes of the isentropes, both at lower and upper altitudes, were in accord with the positive and negative signs of the ascent rate anomaly signifies the presence of updrafts and downdrafts associated with a

gravity wave. This agreement indicates that our method for estimating atmospheric vertical velocity from balloon ascent rate is reliable. Quantitative estimates of radiosonde-derived vertical velocity are described in subsection *c* and compared with a numerical simulation. It should be noted that the wave potential temperature contours tended to have large amplitudes at levels where vertical stratification was strong.

Figure 1.10b shows details of the 0530 JST profile in the lower troposphere, including the derived wind speed anomaly. Positive wind speed anomalies reached two peaks under 2000 m, one where the isentropes descended in the lee of the mountain and the other where the isentropes regained their elevation, around FARM station. This strong wind corresponded with the downward wind leeward of the mountain top, where the isentrope descended sharply and the ascent of the balloon was strongly inhibited.

Figure 1.10c shows the wind direction along the profile and the transverse component of the wind, defined as the degree to which it blew to the right of the plane of the profile as seen facing leeward. The troposphere had a two-layered wind flow in which the wind was west-southwesterly in the upper layer and westerly in the lower layer (thus having a large transverse component). The resulting shear at the boundary between the two layers, at about 2000 m, caused the boundary to form wave patterns.

Figure 1.10d displays profiles of relative humidity and equivalent potential temperature. High humidities showed that a cloud layer was present around 2000–3500 m, where the potential temperature was not conserved along the path of an air parcel. The equivalent potential temperature, which is conserved under moist adiabatic processes, showed better agreement with fluctuations of the ascent rate

anomaly than the potential temperature. Especially in the unsaturated layer below the cloud base (<2500 m), both the equivalent potential temperature and the potential temperature had almost the same isentropic structure. Both the isentropes descended in the lee of the mountain and regained altitude farther downwind; thus the isentropes of the potential temperature (Fig. 1.10b) and equivalent temperature (Fig. 1.10d) were interchangeable below 2500 m. It is reasonable to assume that the air parcel traveled along the isentrope, at least below the cloud base.

The lower layer corresponded to the layer with positive wind speed anomaly (Fig. 1.10b) where the westerly wind approached the mountain perpendicularly and generated strong winds on the downstream side. The rise-and-fall pattern of the isentrope associated with a strong wind in the lower layer resembles the pattern of a hydraulic jump. The large transverse component of the lower wind (Fig. 1.10c) raises the possibility that the structure is distorted by its projection onto the profile plane. However, the westerly wind was closely aligned with the observation sites (Fig. 1.3a), and the results shown in Fig. 1.10 were not sensitive to differences in the chosen azimuth of the profile plane.

Figure 1.10 implies that our observations qualitatively captured the downslope windstorm. Atmospheric conditions on the windward side of a range are known to control the flow regimes across a mountain barrier [e.g., Vosper 2004; Reinecke and Durran 2008]. The vertical profiles of zonal wind, wind direction, relative humidity, and potential temperature observed at the westernmost (upwind) end of our transect are shown in Fig. 1.11. The profiles at 0530 JST had two distinguishing features compared to those at other times. First, a strong zonal wind layer, corresponding to westerly winds, was observed at 1500–2500 m height at

0530 JST (Figs. 1.11a and 1.11b). These winds were perpendicular to the mountains, were associated with very dry air, and were located below the cloud base (Fig. 1.11c). Whereas the other potential temperature profiles showed well-mixed air overlain by an intense inversion layer (Fig. 1.11d), the 0530 JST profile displayed warmer conditions and stable stratification above 1500 m. The level of the inversion layer corresponded to the level of incoming dry air.

Using these upwind soundings, we evaluated the conditions associated with the occurrence of downslope winds in terms of the Froude number Fr, the ratio of the flow velocity divided by the phase speed of a gravity wave. In terms of shallow-water wave theory, the occurrence of a downslope windstorm is associated with a transition from subcritical (Fr < 1) to supercritical (Fr > 1) flow [Durran and Klemp 1987; Durran 1990]. In addition, it is known that the flow regimes of simple shallow water fluid over a mountain are characterized by the relation between Froude number of an upstream side and non-dimensional mountain height [e.g., Fig. 1 in Saito 1992]. We assumed a simple two-layer flow, with the layers divided by the change in gradient of the isentrope.

For the calculation of Fr,

$$Fr = U / \sqrt{g H}, \quad (1)$$

$$M_c = m_c / H , \quad (2)$$

where the parameter U is the averaged zonal wind component in H, the thickness of the fluid from the surface to the altitude associated with the inversion layer and g is the acceleration of gravity. M_c is a non-dimensional mountain height which is a mountain height m_c divided by the depth of flow H. In case of 0530 JST, we evaluated Fr = 0.141 (H = 1500 m, U = 17.06 m s^{-1}, and g = 9.8 m s^{-2}) and Mc = 0.54 (height of Mt. Kasatori is about 810 m). These values are not

fully satisfied the critical levels of the regime that a steady flow with a stationary lee jump in the diagram of Saito [1992] but the value of Mc is nearly critical.

We additionally evaluate an internal Froude number Fr,

$$Fr = U / \sqrt{(\Delta\theta / \overline{\theta}) gH} , \qquad (3)$$

where $\overline{\theta}$ is the mean potential temperature in the fluid and $\Delta\theta$ is the difference in potential temperature between the two layers. The term $(\Delta\theta / \overline{\theta})g$ is the reduced gravity, from which the phase speed is calculated. Table 1.2 shows the values of Fr and each relevant parameter during the observation period. The value of Fr at 0530 JST was nearly 1.0, meaning that the state of flow over the mountain was nearly critical and suggesting that atmospheric conditions were likely to induce a downslope wind. At all other times, however, Fr was less than 0.5 because the phase speed was greater than at 0530 JST; thus the upstream flow was in a subcritical state.

2) LOW-LEVEL JET

At 1430 JST, the Tsu station observed strong surface winds whereas the wind at Mt. Kasatori was near its weakest point during the windstorm (Fig. 1.7). The profile at that time (Fig. 1.12a; orientation shown in Fig. 1.3b) consisted of two layers separated by a stratified layer at about 3000–4000 m featuring a steep gradient in potential temperature and wavy isentropic lines. In the lower layer, below 3000 m, there was little atmospheric stability. The upper layer had a stratified wavy structure and was located above the cloud top. The equivalent potential temperature in the upper layer had almost the same structure as the potential temperature, although with weaker amplitude (Fig. 1.12d). The balloons showed little fluctuation in their ascent rates and had fairly linear trajectories,

unlike the large fluctuations seen in the 0530 JST profile. A positive wind anomaly at low elevations on the leeward side (Fig. 1.12b) corresponded to the strong low-level winds observed at UNIV (Fig 1.8c). In addition, a cold air mass was observed only over the leeward side where the low-level air was well mixed (Fig. 1.12b). The wind direction data were also peculiar (Fig. 1.12c): whereas westerly winds dominated the flow over the mountains, a strong northwesterly wind was recorded at low levels on the downwind side that was almost perpendicular to the profile plane.

Figure 1.13 shows time series of wind speed, wind direction, potential temperature, and meridional wind observed at UNIV on the leeward side and IGA on the windward side. The vertical structures of wind direction at both sites rotated clockwise with time similar to the surface winds shown in Fig. 1.7a, indicating that synoptic-scale conditions associated with a dominant wind gradually changed with time. A northwesterly wind was observed in the lower boundary layer at both sites, but it appeared earlier on the leeward side (UNIV) than on the windward side (IGA) (Figs. 1.13a and 1.13c). The meridional wind component was northwesterly at UNIV forming a jet-like structure associated with a large wind shear below 3000 m, where the lower and upper layers had strongly differing wind directions (Fig. 1.13b). Because the topography is nearly flat around UNIV, this northwesterly wind was not of local origin. The potential temperature at both sites gradually decreased during the day, but the cold air mass associated with the northwesterly was also observed at UNIV earlier than at IGA (Figs. 1.13b, d). It should be noted that the potential temperature in the lower layer was lower at 1430 JST, in daytime, than it was around dawn at 0530 JST. Therefore the near-mixed layer was not the result of the diurnal temperature cycle.

These results imply that the northwesterly wind observed at UNIV was a low-level jet that did not originate on the windward side (IGA) of the mountain range. Note that the strong wind accompanying the low-level jet occurred when the Froude number was small, which suggests that the Froude number alone is not a strong indicator of whether a strong wind event will occur on the lee side of the mountain.

c. Numerical simulation of two flow regimes

1) MODEL CONFIGURATION

We conducted a numerical experiment by using version 3.5.1 of the Weather Research and Forecasting Model, Advanced Research WRF [Skamarock et al., 2008] to simulate the two observed flow regimes (Figs. 1.10 and 1.12) for comparison with the profile plains constructed from radiosonde observations, to confirm the basic feasibility of the radiosonde technique and to assess the reliability of the observations. Four nested domains (Fig. 1.14) were used with horizontal grid sizes of 27 km, 9 km, 3 km, and 1 km. The innermost of these domains covers the windward and leeward side of the Suzuka Mountains. We used a two-way nesting simulation, in which the results of a child domain were fed back to a coarser resolution domain. The time step of each domain was 162 s, 54 s, 18 s, and 6 s, respectively. The model top was at 50 hPa (approximately 20 km), and the model contained 50 vertical layers with thicknesses that increased with altitude from approximately 39 m at the bottom to 490 m in the middle troposphere. The initial and lateral boundary conditions for the simulation were taken from the National Centers for Environmental Prediction's Global Forecast System Final Operational Global Analysis (FNL). For topography, we used the

United States Geological Survey's Global 30 Arc-Second Elevation (GTOPO30) dataset, in which the horizontal scale is approximately 1 km. The physical schemes chosen for the simulation variables are summarized in Table 3. The simulation started at 2100 JST 20 March 2010, which was 8 hours before the first radiosonde observations during the downslope windstorm. The period of the simulation was 30 hours, covering the entire day of radiosonde observations. Here we focus on the innermost domain at the same times that the downslope windstorm (0530 JST) and low-level jet (1430 JST) were observed.

2) COMPARISON WITH OBSERVATIONS

To compare the observations (Figs. 1.10 and 1.12) with the simulation, we adopted the same projection plane as was used for the observations (Fig. 1.3). Figure 1.15 presents the simulation results that correspond to the observations shown in Figs. 1.10b, 1.10c, 1.12b, and 1.12c. The simulation data in Fig. 1.15 were picked along the sounding lines. The vertical wind anomaly shown in Fig. 1.15 was calculated as the difference from the average simulated vertical wind profile from the surface to 10 km height, analogous to the calculation of the balloon ascent rate anomaly used for the radiosonde observations.

In the case of the downslope windstorm (Figs. 1.15a and b), the numerical model simulated the observations well. The isentrope descended sharply in the lee of the mountain and then regained altitude where the strong wind was accompanied by meandering of the isentrope. The vertical velocity anomaly was in accord with the shape of the horizontal isentropes and also showed good agreement with the observed ascent rate anomaly (compare Figs. 1.15a and 1.10b). The westerly wind in the lower troposphere was also well simulated in the

numerical model (compare Figs. 1.15b and 1.10c).

To confirm that the projected section represented the actual vertical–horizontal structure, we rendered the simulated variables in altitude–longitude sections onto the two different planes shown in Fig. 1.16, one matching the line used for the observations and the other running due east–west. The results are shown in Fig. 1.17. Compared to the observations (Figs. 1.8a and b), the simulated wind speeds along the sounding lines from stations AOYAMA and FARM were generally overestimated at every level, and along the sounding line from station IGA a constant westerly wind layer below 2000 m was simulated blowing toward the mountain, in contrast to the observations (Figs. 1.17a and c). Analogous to the observations (Fig. 1.10b), the wind speed anomaly appeared on the downstream side of the simulated profile, and the isentropic surface also corresponded to the regime of downslope windstorm (Figs. 1.17b and d). Overall, the simulated and observed wind anomaly structures closely matched each other, but the simulated windstorm was more intense than the actual windstorm. The similarity of these structures on the two different planes indicates that the observational results were substantially independent of the profile orientation.

The vertical wind speed can be deduced from the slope of the observed isentropic curve. The isentropic vertical wind, W_θ, defined as the vertical component of the wind blowing along an isentropic surface, is estimated by the following equations:

$$\phi = \arctan\left[\left(Z_\theta(i+1) - Z_\theta(i)\right)/\delta x\right] \tag{4}$$

$$U_\theta = U_{obs}\cos\phi \tag{5}$$

$$W_\theta = U_\theta \sin\phi \tag{6}$$

The slope angle of the isentrope, ϕ, is calculated by the difference in height of a potential temperature between two neighboring sounding lines. For example, ϕ between IGA Fast and IGA Normal is estimated by Eq. (4), where the height of a specific potential temperature is $Z_\theta(i)$ at IGA Fast (on the windward side) and $Z_\theta(i+1)$ at IGA Normal (on the leeward side), and δx is the horizontal distance of an isentrope between soundings at the *i*-th (windward) and *i*+1-th (leeward) stations. In Eq. (5), U_θ is the component of the wind blowing along an isentropic surface with slope ϕ, and U_{obs} is the parallel wind component along the plane of the profile. Note that W_θ along the plane including UNIV was not estimated because there was no sounding leeward from UNIV.

Figure 1.18 displays the simulated and observed ascent rate anomalies, along with the vertical wind anomaly estimated with Eq. (6), at stations along the sounding lines. The observed ascent rate and the isentropic vertical wind were smoothed by the running mean over 500-m intervals, and the anomalies were calculated with respect to the vertical average below 10 km for a sounding line. At 0530 JST (Fig. 1.18a), during the downslope windstorm period, the ascent rate anomalies of the balloons were in agreement with those of the isentropic vertical wind and the numerical simulation at stations on the windward side (IGA and AOYAMA), especially for IGA, where an intense downward wind at 3500–4000 m was seen in all estimates. At FARM, the isentropic vertical wind showed smaller fluctuations than the other measures. Figure 1.18b shows the correlation coefficient between the ascent rate and isentropic vertical wind anomalies for all the stations, calculated from the bottom to each level. The correlation coefficient exceeded 0.4 below 4000 m and decreased with greater height. It is noteworthy

that the isentropic vertical wind calculated by the potential temperature was correlated well with the balloon ascent rate even in the saturated cloud top layer at about 3500 m (Fig. 1.10d). The simulated, observed, and isentropic estimated vertical wind anomalies were overall in good agreement over the stations, the indication being that the balloon ascent rate measured using our methodology was a reliable indicator of vertical wind speed. To evaluate the reliability of this indicator, we estimated correlation coefficients for each station and for the times of all eight radiosonde launches (Table 1.4). These correlation coefficients were positive at 0530 JST during the downslope windstorm period, averaging 0.47, and the correlations were strong for IGA (0.74) and AOYAMA (0.8). During the other observation periods, however, the overall correlation between the ascent rate anomaly and the simulated vertical wind was weak except at 0830 JST (Table 1.4).

Our results show that for the downslope windstorm regime, the technique of multiple sounding with varied buoyancies [Shutts et al. 1994] can be used to better cover the space between multiple observation sites (Fig. 1.10a). The differing trajectories of fast and normal balloons launched at IGA produced more data in the region between IGA and AOYAMA, and the slow balloon launched at UNIV on the leeward end of the profile expanded the area of observations to the east. This strategy thus offers advantages when the possible observation sites for balloon launches are restricted, as is often the case in Japan. It offers a way to achieve higher resolution and cover wider ranges. The 13 km horizontal distance between our observation sites was appropriate to capture the structure of the downslope windstorm. The technique is also significant in enabling us to discern vertical and horizontal air motions on the basis of both isentropes and ascent rate

anomalies of radiosonde balloons. It is surprising that the vertical wind field deduced from balloon ascent rates shows good agreement with vertical winds inferred independently from the horizontal shape of isentropes (Figs. 1.10a and 1.17a). The numerical experiment supported these results.

The low-level jet regime was not fully replicated by our numerical simulation. The simulated wind speed anomaly and the transversal component show that the wind speed was higher at FARM and UNIV than at IGA, matching the observational results (compare Figs. 1.15c, 1.15d, and 1.19 with Figs. 1.12b and 1.12c). However, the simulated potential temperatures had a pattern representing a stably stratified layer between the windward and leeward side below 3000 m, in contrast to the mixed layer that was observed. The simulated wind direction on the windward side of the mountains was north-northwesterly, whereas the observations at IGA showed a westerly wind. These disagreements represent a failure of our numerical simulation to replicate the atmospheric conditions during the low-level jet. As our model configuration was inadequate to resolve the low-level jet, we lack enough evidence to clarify the cause of the jet. The vertical winds estimated from the ascent rate and the slope of the isentrope also disagreed with each other during the low-level regime (Fig. 1.18c); the correlations were negative (Fig. 1.18d). This disagreement may reflect the fact that the variation in vertical motion was small, unlike during the period of the downslope wind, such that the balloons were only weakly influenced by vertical wind during their ascent. Johansson and Bergström [2005] have shown that balloon ascent rates tend to be higher within the boundary layer than above it, owing to a decrease in the drag on the balloon due to turbulence. For example, the ascent rate anomaly at IGA Normal (Fig. 1.18c) was overestimated below 4000 m, a level that corresponded

to the top of the constant potential temperature layer (Fig. 1.11d). This layer was well mixed; thus, the ascent rate anomaly could not be correlated with vertical air motions. Because the slope of the isentrope was also weak at this time, the vertical wind derived from the potential temperature was not reliable.

It appears that two methods of estimating the vertical wind, by the balloon ascent rate and by the slope of the isentrope, worked better during conditions such as the downslope windstorm, when upward or downward motion was vigorous. Although the measurement of vertical winds is one of the most difficult problems in atmospheric science, our method, despite its simplicity, offers a way forward, subject to confirmation by future studies.

Our findings revealed two limitations of our method. The first is that to produce the best results, our method depends on the strength of winds. In our launch at 1430 JST, for example, the two balloons launched from FARM followed almost the same trajectory below 3000 m where the winds were weak (Fig. 1.8c), although they separated in the much stronger winds at higher elevations (Fig. 1.12a). There is an optimum range of wind speeds for sampling the vertical–horizontal profile, given that excessively strong winds will carry the balloons downwind too fast to sample the full vertical profile over the mountain. The second weakness is that the position of launch sites restricts the direction of longitudinal profiles, limiting our ability to trace the low-level jet outside the profile plane. A multiple-sounding program should be designed carefully with respect to the orientation of target phenomena.

1.4 Discussion with statistical analyses

Our observational strategy succeeded in making snapshot-like depictions of the detailed structure of a Suzuka-oroshi event. It is, to our knowledge, the first time that the wavy structure of the potential temperature field over a mountain range at a horizontal scale less than 100 km has been mapped by using only radiosonde soundings. Moreover, our observations revealed two flow regimes associated with the Suzuka-oroshi, a downslope windstorm and a low-level jet. The first regime was characterized by a westerly wind, and the upstream flow represented a critical condition as deduced from the internal Froude number. The second regime, a jet-like structure flowing parallel to the mountain range, was characterized by a cold northwesterly wind that appeared first on the downwind side of our profile. Owada and Harada [1978] suggested that the Suzuka-oroshi is a northwesterly wind originating as a lee wave over the Suzuka Mountains. The low-level jet regime we documented is consistent with their hypothesis. The occurrence of the downslope windstorm regime is reasonable because the Froude number was near the critical level. However, as strong wind event accompanied the low-level jet despite a small value of the Froude number. Because IGA and UNIV stations are located a roughly linear west-to-east transect, IGA could not capture an actual windward condition associated with UNIV when the north-westerly wind dominates at the lee of the mountain. This problem may hide the structure and factor of the occurrence of the low-level jet regime. One possibility of the hidden structure of the low-level jet regime might be a downslope wind generated by a mountain range with a col. In fact, Suzuka-path is located as a col of the Suzuka-mountain range. When a flow passes over such a mountain, a shallow strong-wind area extends to leeward in the lee of the col

[Saito 1993]. The captured jet-like structure might be a part of such shallow strong wind associated with Suzuka-path, but our observational results could not clarify this possibility.

In an attempt to uncover hidden factors in the occurrence of the low-level jet regime, we performed a statistical data analysis comparing the observational and numerical results for periods of strong northwesterly winds. We began with the record of strong winds in the study area in the winter months (December–March) between 1987 and 2011 (Fig. 1.20a), defining windy days as days when the hourly-mean wind speed exceeded 10 m s^{-1} at Tsu or at one of the nearby JMA weather stations Ueno, Kameyama, and Yokkaichi (UN, KM, and YK in Fig. 1.2). This definition is the same one used by Owada [1990]. The results show that Tsu clearly experienced more days of strong wind than other stations in each of these months, and the number of windy days increased from December to March. The proportion of northwesterly winds during these days of strong wind also increased from December to March. In March, northwesterly winds accounted for approximately 60% of the windy days at Tsu.

Considering the results of that exercise, we selected a larger set of medium or higher wind speed events from the winter months of the 1987–2011 record in which the hourly-mean wind speed at Tsu exceeded the average of the wind speeds at the three neighboring stations by more than 5 m s^{-1}. We chose this criterion to match conditions during the low-level jet regime, in which the wind at UNIV, the station nearest Tsu (Fig. 1.2), was much stronger than in the surrounding area. First we subtracted the hourly average wind speed at the three stations (Ueno, Kameyama, and Yokkaichi) from the wind speed at Tsu for each hour and determined the hour of the day with the greatest difference. Next, we

selected the days when this greatest difference in wind speed exceeded 5 m s^{-1} and defined them as windy days. The wind direction of a windy day was then defined as the wind direction at Tsu during the hour of the greatest difference in wind speed with respect to its neighboring stations. On some of these windy days the hourly-mean wind speeds at Tsu were less than 10 m s^{-1}, but they were nevertheless much stronger than those at the surrounding stations. Figure 1.20b shows the temporal distribution of these windy days with their wind direction indicated. The seasonal variations in the number of windy days and in the proportion of northwesterly winds are similar to those shown in Fig. 1.20a. Figure 1.20 thus implies that the wind direction was northwesterly during the period of Suzuka-oroshi in March. The 645 windy days with strong northwesterly winds had strong northwesterly winds only on the lee side of the radiosonde sounding line, and their mean wind speed was 10.3 m s^{-1}. This group of "strong northwesterly days" also included the day we conducted the radiosonde observations and observed the low-level jet. Although not every strong northwesterly day may be associated with a low-level jet, the ensemble of such days should display common features associated with the low-level jet.

To identify the synoptic conditions generating the strong northwesterly winds at Tsu, we prepared maps of the average conditions during the 645 strong northwesterly days by using the 6-hourly product of JRA-25/JCDAS, setting the zero hour as the hour in the JRA25 product nearest to the start of the strong northwesterly wind (Fig. 1.21). The average sea-level pressure pattern at hour 0 was a typical winter monsoon wind pattern called "west high and east low" (Fig. 1.21a). Figure 1.21b indicates the average evolution of the geopotential height anomaly (departure from the 24-h average) at the nearest grid point to Tsu over

the 24 hours centered at hour 0. The figure shows that the vertical structure of the geopotential anomaly changed from negative to positive at hour 0. These features signify that the vertical structure changed from one associated with a low-pressure system to one associated with a high-pressure system at the time the strong northwesterly was first detected at Tsu.

Figure 1.21a also shows the average relative vorticity at 925 hPa during the strong northwesterly days at hour 0. The area of negative vorticity, which corresponds to anticyclonic circulation, covers the west side of Japan, and the Tsu area is at its edge. The evolution of the vertical profile of relative vorticity (Fig. 1.21b) indicates that the vorticity below 900 hPa shifted sign from positive to negative, similar to the change in the geopotential anomaly. These features show that the shift from cyclonic to anticyclonic circulation is a diagnostic indicator for the outbreak of a strong northwesterly day. This change corresponds to the eastward progress of synoptic-scale anticyclonic circulation, as shown in the eastward extension of the area of negative vorticity in Fig. 1.21a.

We then investigated whether the low-level jet event of 21 March 2010 satisfies this environmental condition. Figures 1.21c and 1.20d depict the conditions in the reanalysis dataset on the day of the radiosonde observations. Hour 0 was set at 1500 JST 21 March 2010, the onset of the low-level jet. At that time the hourly-mean wind speed at Tsu, 11.5 m s^{-1}, exceeded the mean of the surrounding three stations by more than 7.3 m s^{-1}, the largest wind-speed difference of the day (see bottom of Fig. 1.21d). An area of negative vorticity covered the west side of Japan with its edge reaching the observation area (Fig. 1.21c), and the pattern of vorticity elsewhere was also quite similar to the statistical pattern in Fig. 1.21a. The vertical profiles of the geopotential anomaly

and relative vorticity near Tsu that day (Fig. 1.21d) were also quite similar to the statistical profiles (Fig. 1.21b), with the vertical structure over Tsu changing from a low-pressure system to a high-pressure system and shifting to negative vorticity below 900 hPa. The agreement between the observations and the statistical pattern implies that the synoptic conditions just described are important factors for the occurrence of strong northwesterly winds with a low-level jet.

The vorticity patterns on 21 March 2010 in our numerical simulation are shown in Figs. 1.21e and 1.20f. Note that the simulation did not reproduce the low-level jet (see Fig. 1.19). The synoptic features in Fig. 1.21e roughly correspond to those of the reanalysis dataset in Fig. 1.21c, but the positive relative vorticity in the observation area does not agree with the negative vorticity in the reanalysis and in the statistical results in Fig. 1.21a. The vertical profiles were well simulated (Fig. 1.21f), except that the relative vorticity in the lower layer in the simulation was positive from 09z to 15z, indicating cyclonic circulation over the Suzuka Mountains, in conflict with the reanalysis (Fig. 1.21d) and the statistics (Fig. 1.21b). The reason our numerical experiment failed to simulate the strong northwesterly regime with the low-level jet may be its failure to reproduce the synoptic-scale vorticity change from cyclonic to anticyclonic.

This comparison suggests that a synoptic-scale shift in vorticity from positive to negative (from cyclonic to anticyclonic circulation) is a key factor in the occurrence of strong northwesterly winds at Tsu. Our radiosonde observations revealed that the low-level jet regime occurred when strong northwesterly wind was observed only at Tsu, and when synoptic-scale conditions indicated a change in sign of the vorticity.

1.5 Concluding remarks

Our observational strategy of simultaneous multiple-site radiosonde observations with varied buoyancies yielded detailed two-dimensional profiles of the strong Suzuka-oroshi wind crossing the Suzuka Mountains. Our observations also documented two flow regimes associated with the Suzuka-oroshi, a downslope windstorm and a low-level jet. The second of these regimes, although not yet characterized in detail, may offer important insights into the Suzuka-oroshi. Our comparison of the observations with a numerical simulation and a statistical data analysis offers evidence that synoptic-scale negative vorticity (anticyclonic circulation over the domain) is a favorable condition for generating strong northwesterly winds with a low-level jet. The Froude number is conventionally used as an indicator for the occurrence of leeside strong winds, but it failed in the case of the low-level jet regime. Why this shift in the observation area from positive to negative vorticity, corresponding to the onset of anticyclonic circulation, is a useful indicator for the low-level jet regime in Suzuka-oroshi events will be the subject of future work, including comparisons of observational data with mesoscale simulations.

The ascent rate of the radiosonde balloon and the slope of isentropes both provide a reliable indication of the vertical wind direction (upward or downward) during downslope windstorms. This method offers better coverage of a longitudinal wind profile by varying the ascent paths of simultaneously launched balloons, although its advantage is greatest at high wind speeds. By relying exclusively on radiosondes, it offers useful results at relatively low cost.

Note that our observational method performed well for the downslope windstorm but not for the low-level jet regime. Nevertheless, the multipoint

sounding method holds promise. Conventional upstream sounding succeeded in predicting leeward strong winds, but the upstream soundings alone were not able to detect the low-level jet regime. The advantage of radiosondes over airplane measurements is that radiosonde observations have high vertical resolution from the surface through the troposphere. The method of multipoint sounding, by taking advantage of this high vertical resolution in the boundary layer, was able to detect a low-level jet regime. For a future field campaign, we would add stations on the northwest side of the Suzuka Mountains to capture the structure of the strong northwesterly winds that accompany the low-level jet.

1.6 Tables and Figures

Table 1.1. Observation stations, radiosonde balloon types, and release times.

Observation site	Balloon type	0530 JST	0830 JST	1130 JST	1430 JST	1730 JST	2030 JST	2330 JST
IGA	Fast	0532	0902	1132	failure	1732	2029	2338
	Normal	0532	0830	1132	1440	1732	2029	2338
AOYAMA	Normal	0532	0831	1149	1425	1724	2026	2345
FARM	Fast	0540	failure	1129	1431	1730	2034	2342
	Normal	failure	failure	1127	1434	1731	2030	2337
UNIV	Slow	0530	0830	1130	1505	1732	2033	2332

Table 1.2. Values of parameters used to calculate the Froude number.

Time (JST)	H (m)	U (m s^{-1})	$\bar{\theta}$ (K)	$\Delta\theta$ (K)	Δz (m)	C (m s^{-1})	Fr
0530	1500	17.06	288.36	6.39	500	18.05	0.95
0830	3420	23.53	288.77	20.17	740	48.38	0.49
1130	3680	19.77	287.58	20.41	560	50.59	0.39
1430	3780	16.68	287.28	14.85	400	43.76	0.38
1730	3000	15.27	283.80	14.54	520	38.81	0.39
2030	2680	17.40	281.35	14.37	720	36.63	0.48
2330	2000	11.39	278.80	17.19	1200	34.77	0.33

Δz is a difference from H to the top of the inversion layers.

C is a phase speed calculated from a reduced gravity, define as $C = \sqrt{(\Delta\theta / \bar{\theta})gH}$.

Table 1.3. Model parameters used for the simulation.

Variables	Schemes
Microphysics	WRF Double-Moment 6-class (Lim and Hong 2010)
Planetary Boundary layer	Yonsei University scheme (Hong et al. 2006)
Surface layer	MM5 similarity based on Monin-Obukhov (e.g. Zhang and Anthes 1982)
Long wave radiation	A new version of Rapid Radiation Transfer Model (Iacono et al. 2008)
Short wave radiation	New Goddard scheme (Chou and Suarez 1999)
Land surface model	Noah Land Surface Model (Tewari et al. 2004)
Cumulus parameterization	Kain-Fritsch scheme (Kain 2004)

Table 1.4. Correlation coefficients between the ascent rate anomalies of balloons and the vertical velocity calculated by WRF.

Observation site	Balloon type	0530 JST	0830 JST	1130 JST	1430 JST	1730 JST	2030 JST	2330 JST
IGA	Fast	0.74	0.46	0.29	Failure	0.06	0.11	0.68
	Normal	0.45	0.83	0.36	0.47	0.18	0.24	0.21
AOYAMA	Normal	0.8	0.81	–0.17	–0.48	–0.04	0.0	0.2
FARM	Fast	0.28	Failure	0.08	–0.14	–0.56	–0.29	–0.09
	Normal	Failure	Failure	0.36	0.6	–0.26	–0.34	–0.04
UNIV	Slow	0.6	–0.11	–0.35	0.06	–0.38	–0.26	0.27
All		0.47	0.5	0.22	0.13	–0.09	0.03	0.17

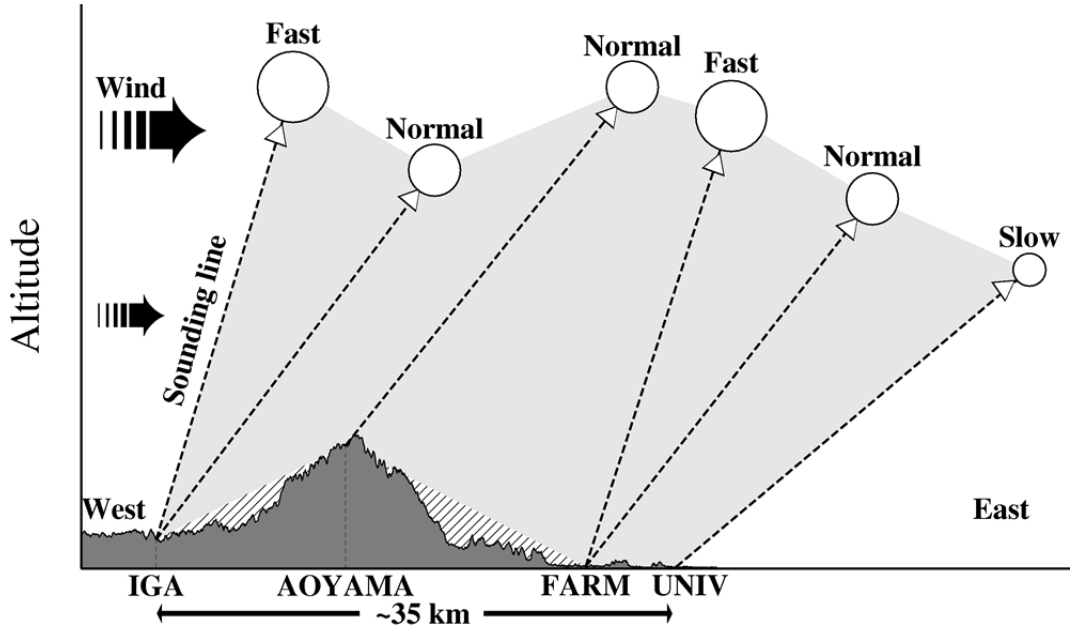

FIG. 1.1. Schematic diagram of the experimental profile showing how variable vertical trajectories (dashed lines) of balloons (circles) improves coverage of the profile.

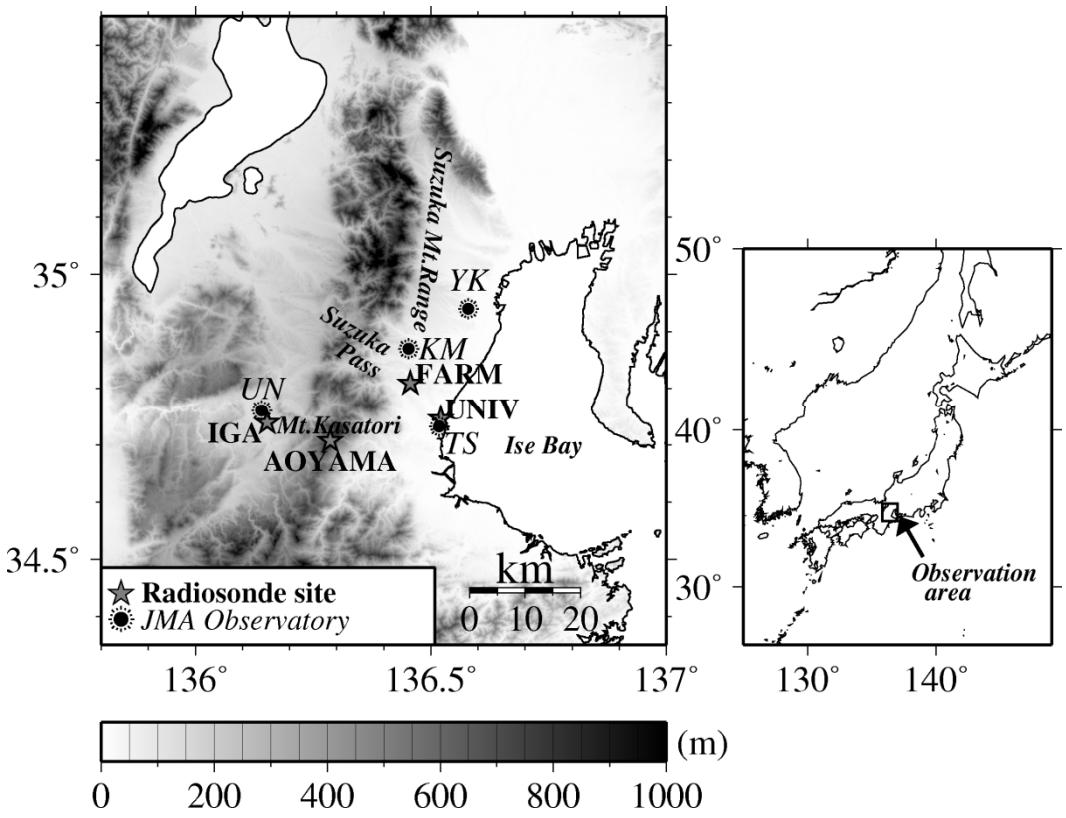

FIG. 1.2. Map of the observation area. Gray shading indicates elevation; stars indicate observatories used in this study; circles indicate JMA meteorological stations. TS, TSU; KM, Kameyama; UN, Ueno; and YK, Yokkaichi.

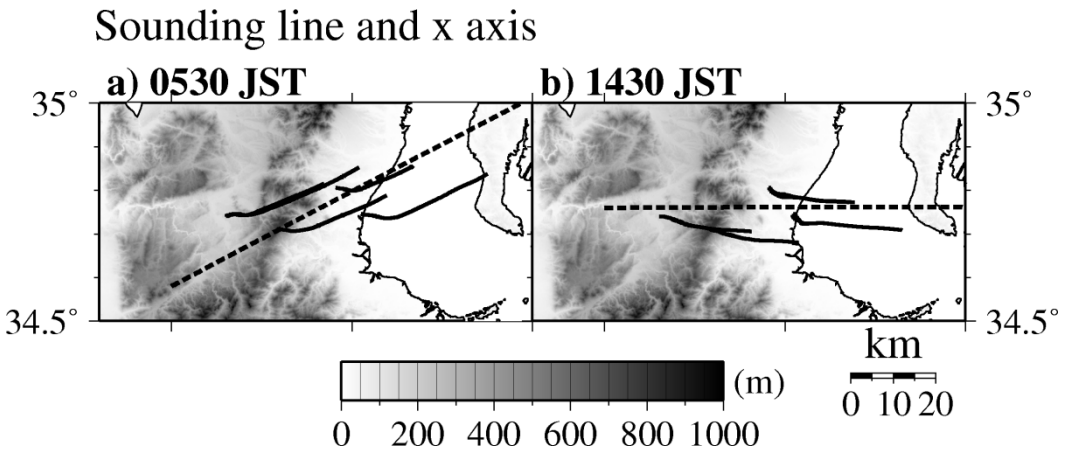

FIG. 1.3. Balloon trajectories at elevations <5000 m (solid lines) and orientation of profile planes (dashed lines) at (a) 0530 JST and (b) 1430 JST.

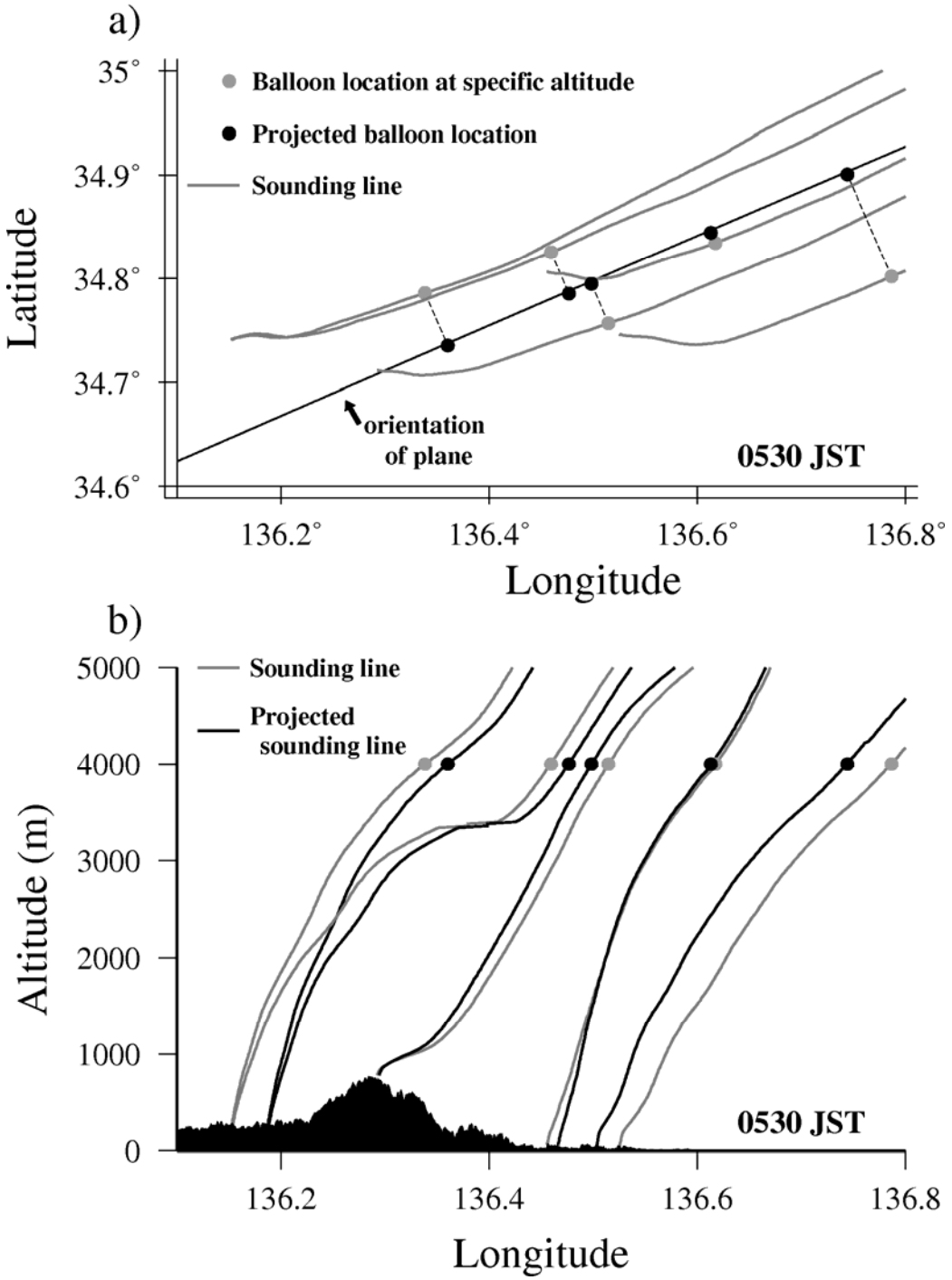

FIG. 1.4. Schematic diagram of the method for projection to a two-dimensional longitudinal plane. (a) Horizontal projection of sounding lines onto a specific plane. (b) Location of sounding lines projected onto a longitudinal plane.

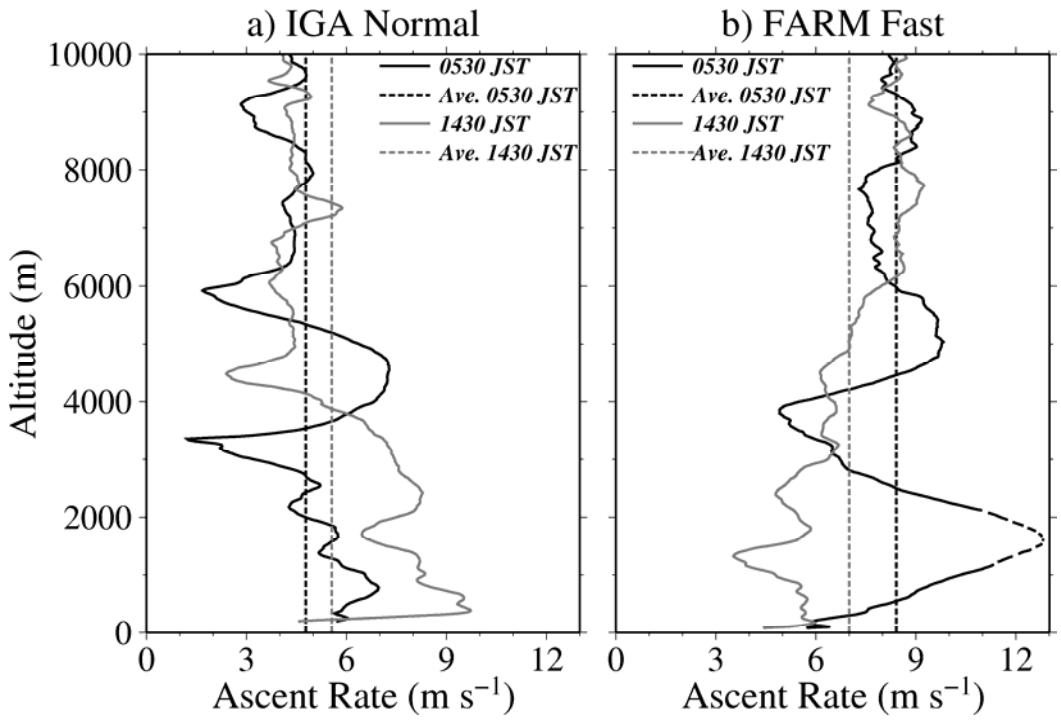

FIG. 1.5. Vertical profiles of balloon ascent rate (solid lines) and vertically averaged value from the surface to 10 km (dashed lines) observed by (a) the IGA normal radiosonde and (b) the FARM fast radiosonde at 0530 JST (black) and 1430 JST (gray).

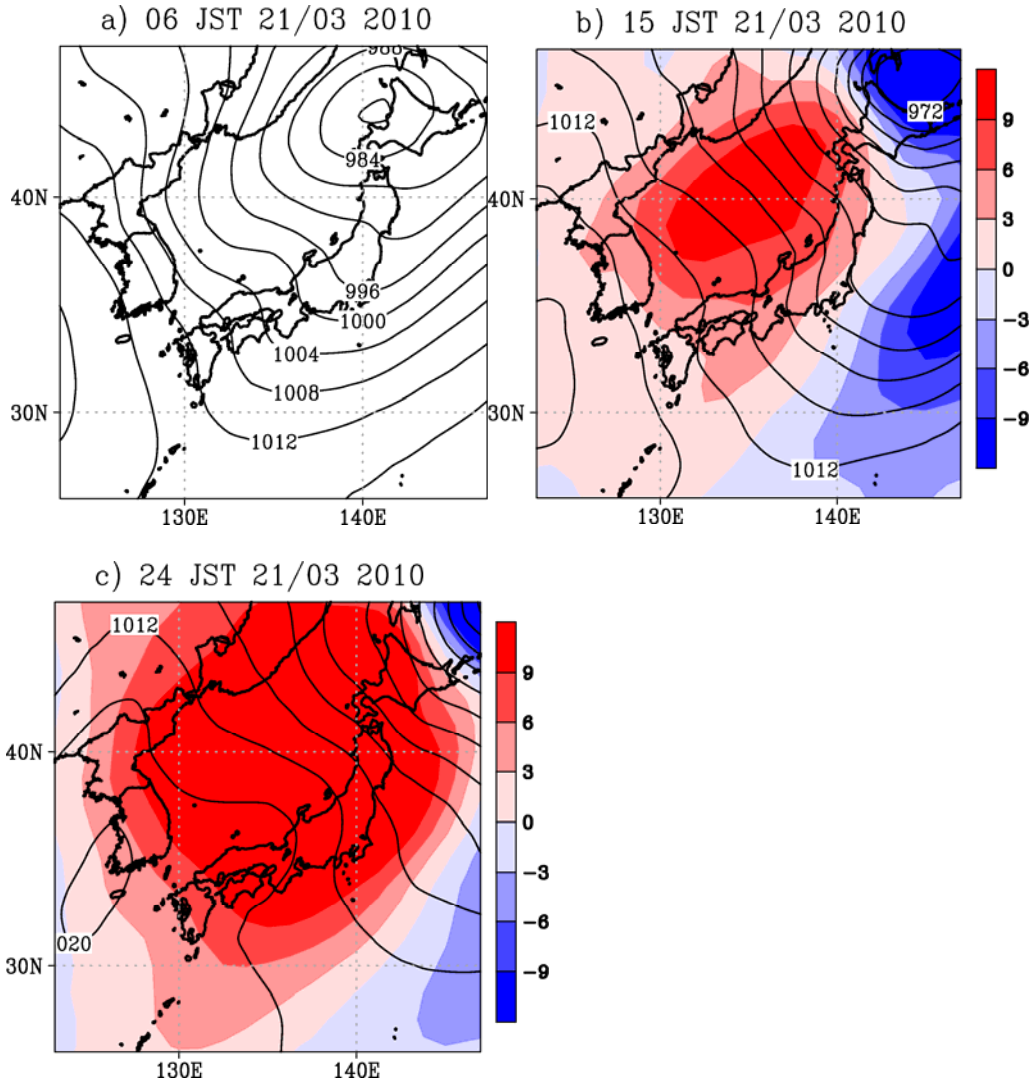

FIG. 1.6. Synoptic weather map of Japan at a) 06 JST, b) 15 JST and c) 24 JST on 21 March 2010. Sea-level pressure is indicated by contours. Contour interval is 4 hPa. Color indicates the anomaly of sea level pressure from 06 JST.

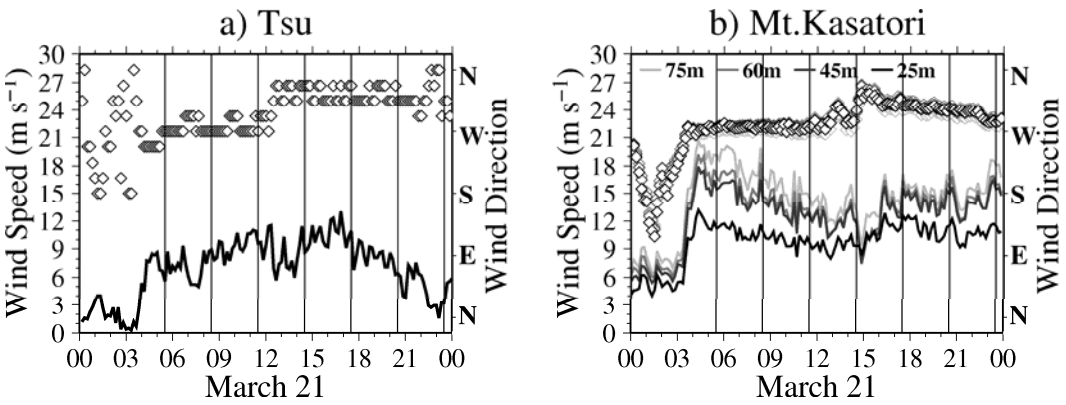

FIG. 1.7. Time series of wind speed (lines) and wind direction (symbols) recorded at (a) the Tsu station and (b) Mt. Kasatori averaged over 10-minute intervals on 21 March 2010. Vertical lines show the times of the radiosonde observations.

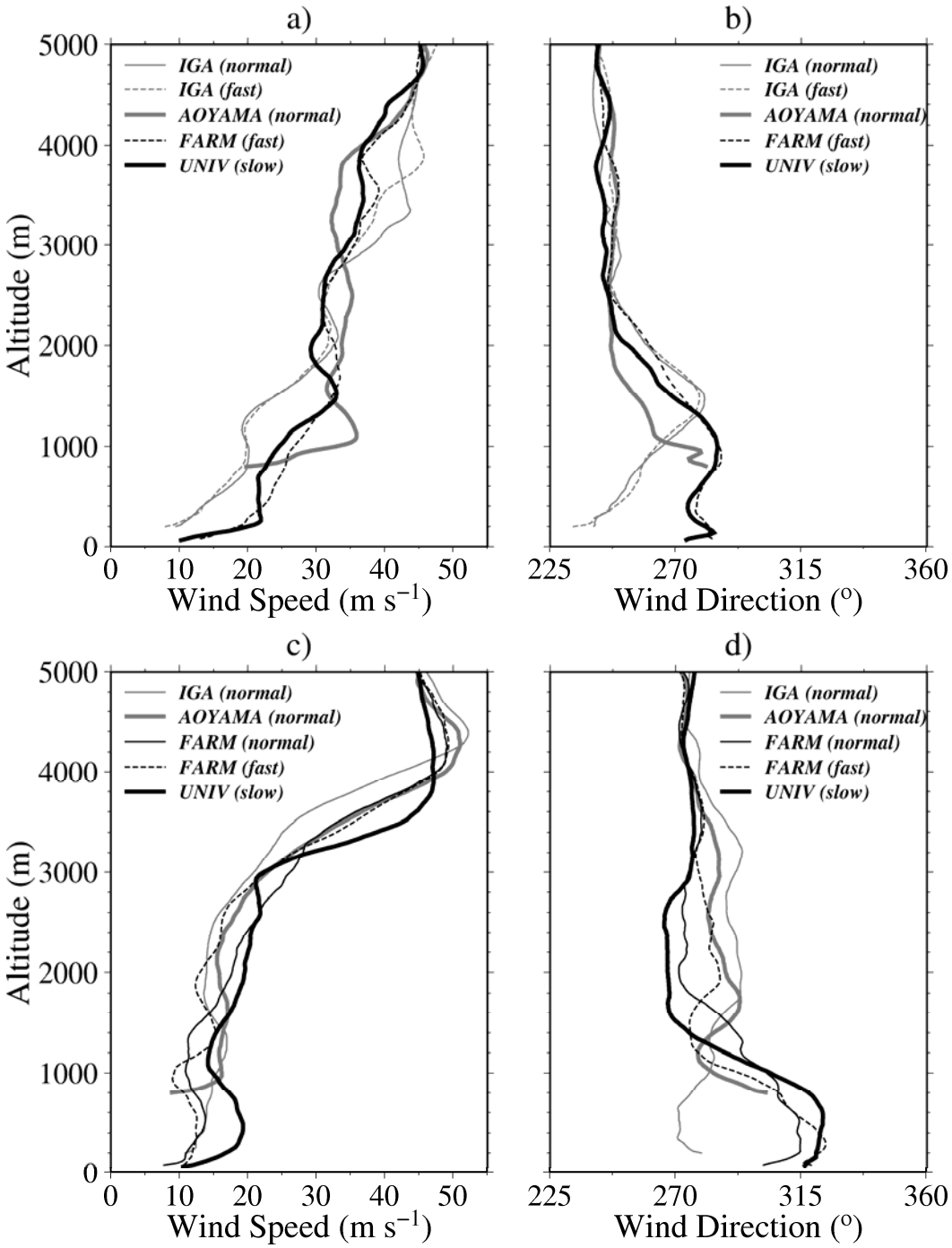

FIG. 1.8. Vertical profiles of (a) wind speed and (b) wind direction observed at 0530 JST and (c) wind speed and (d) wind direction observed at 1430 JST.

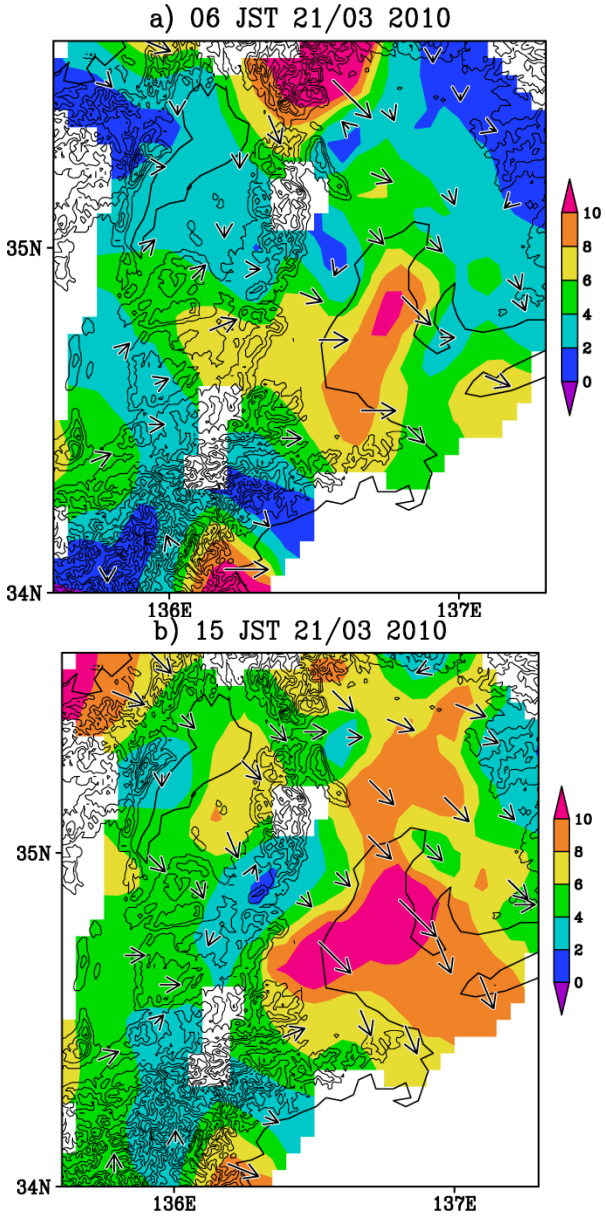

FIG. 1.9. 1-hour averaged horizontal wind maps at a) 06 JST and b) 15 JST on 21 March 2010. Vector indicates horizontal wind observed by the meteorological stations of JMA. Color indicates the map of surface wind speeds constructed by the value of JMA stations. It should be noted that the map of wind speeds was interpolated by using only land observatories, thus the area without observatories, e.g., over the ocean, might not indicate an actual wind speed.

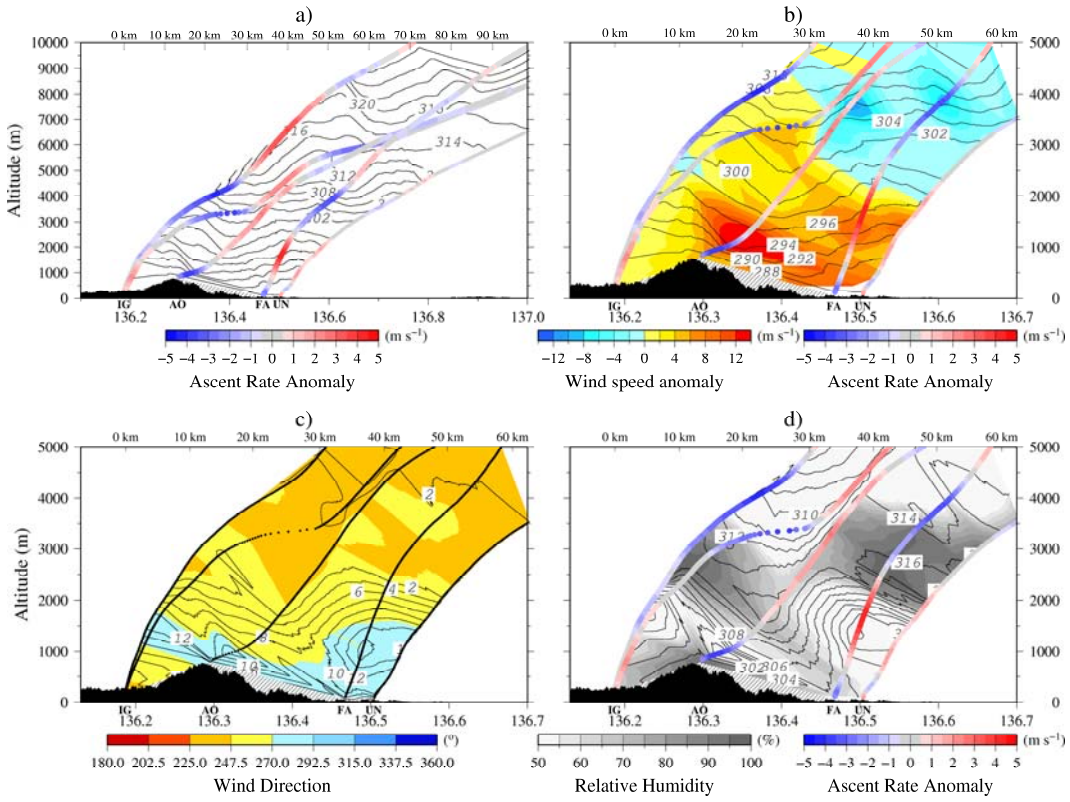

FIG. 1.10. Longitudinal profiles at 0530 JST. (a) Potential temperature (contours, interval 2 K) and ascent rate anomaly of balloons (color). (b) Enlarged profiles of the wind speed anomaly (color shade), ascent rate anomaly of balloons (color line), and potential temperature (contours, interval 2K). (c) Transverse wind component (contours, interval 2 m s^{-1}) and wind direction (color shade). The black curves indicate the balloon trajectories. (d) Equivalent potential temperature (contours, interval 2 K), relative humidity (gray shade), and ascent rate anomaly of balloons (color). IG, AO, FA, and UN denote the locations of stations IGA, AOYAMA, FARM, and UNIV, respectively. The horizontal axes are east longitude (bottom) and the distance from IGA (km). The black area indicates the surface topography; hatching indicates regions where data were insufficient to calculate wind speeds.

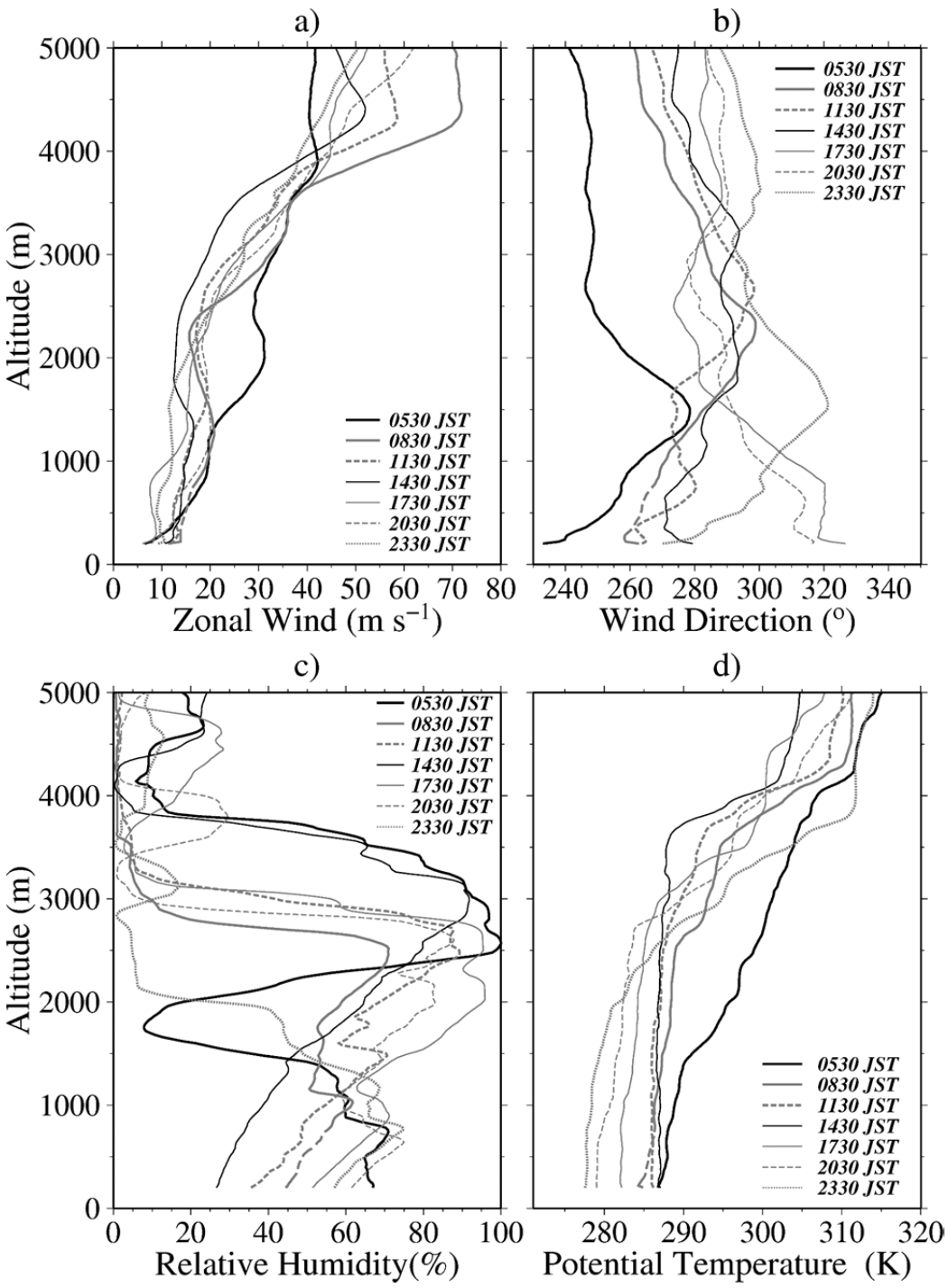

FIG. 1.11. Vertical profiles of (a) zonal wind component, (b) wind direction, (c) relative humidity, and (d) potential temperature observed at the most upstream side during the observation period.

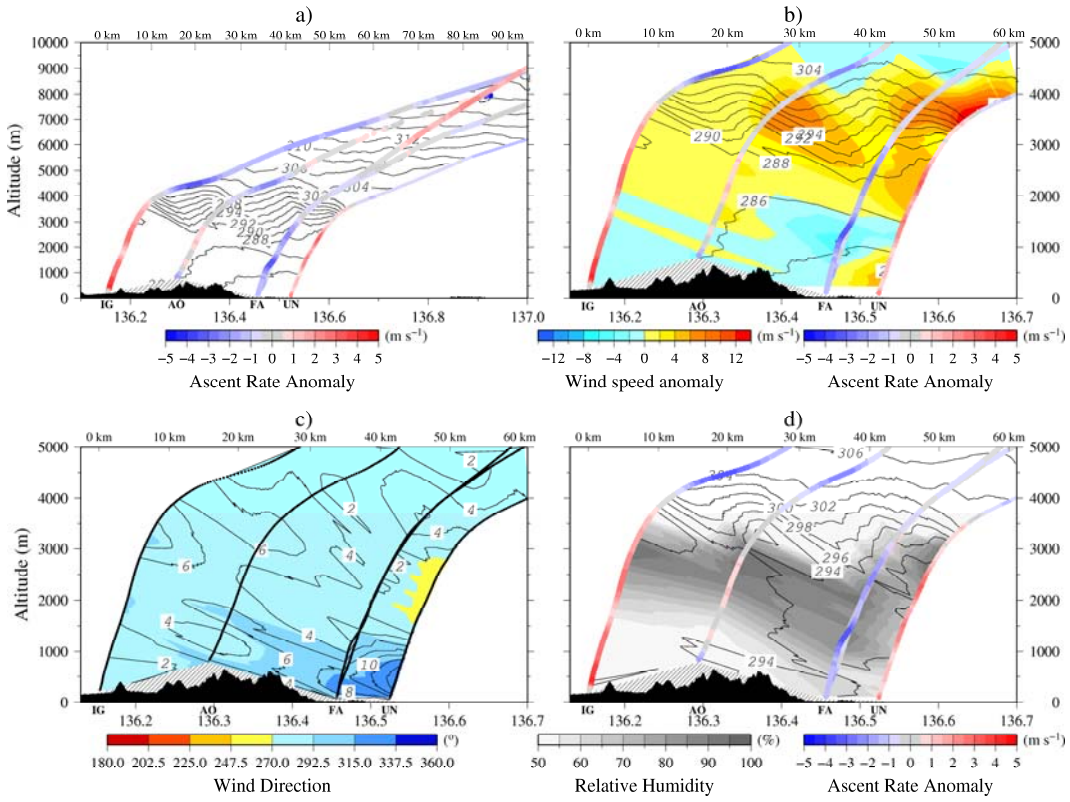

FIG. 1.12. Longitudinal profiles at 1430 JST of (a) potential temperature and ascent rate anomaly of balloons, (b) enlarged profiles of wind speed anomaly, balloon ascent rate anomaly, and potential temperature, (c) transverse wind component and wind direction, and (d) equivalent potential temperature, relative humidity, and balloon ascent rate anomaly. Details as in Fig. 1.10.

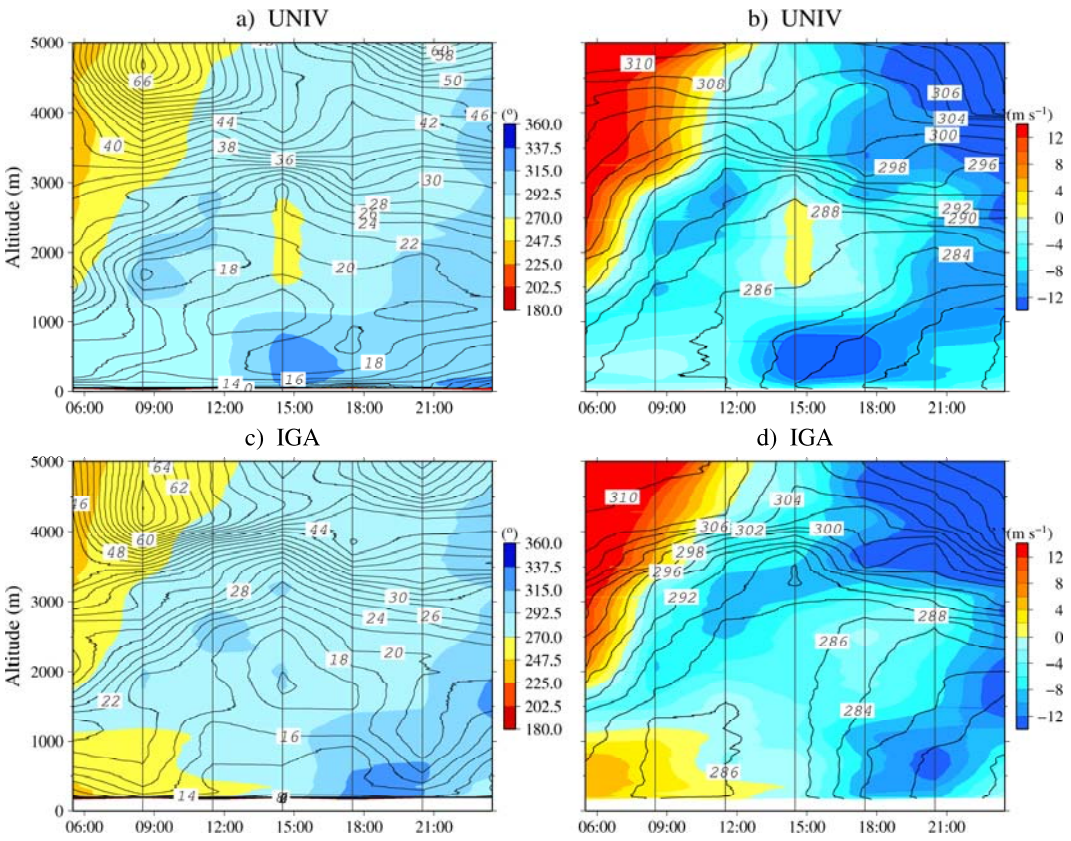

FIG. 1.13. Altitude–time sections of (a) wind speed (contours, interval 2 m s^{-1}) and wind direction (color shade), and (b) meridional wind component (contours, interval 2 m s^{-1}) and potential temperature (color shade) at UNIV, and (c) wind speed and direction and (d) meridional wind component and potential temperature at IGA.

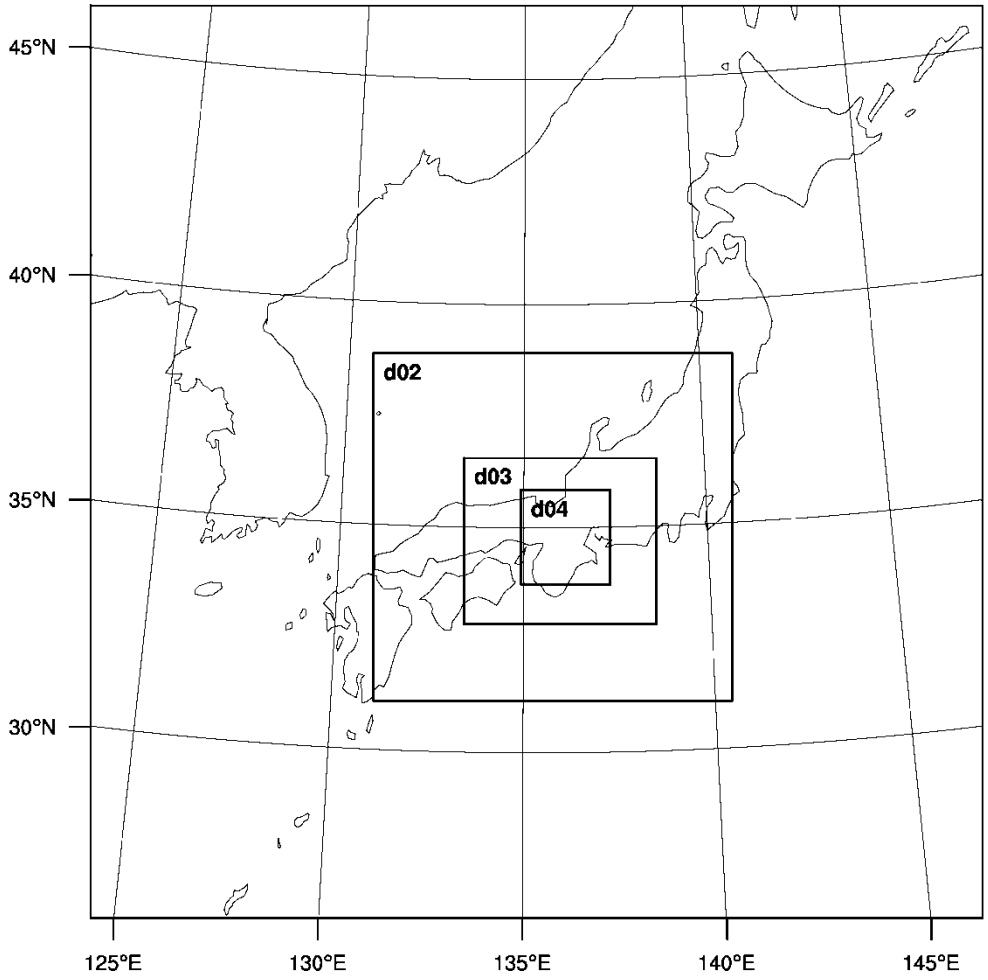

FIG. 1.14. Domain configuration for the simulation. DO2, 3, and 4 are the areas of the three nested domains.

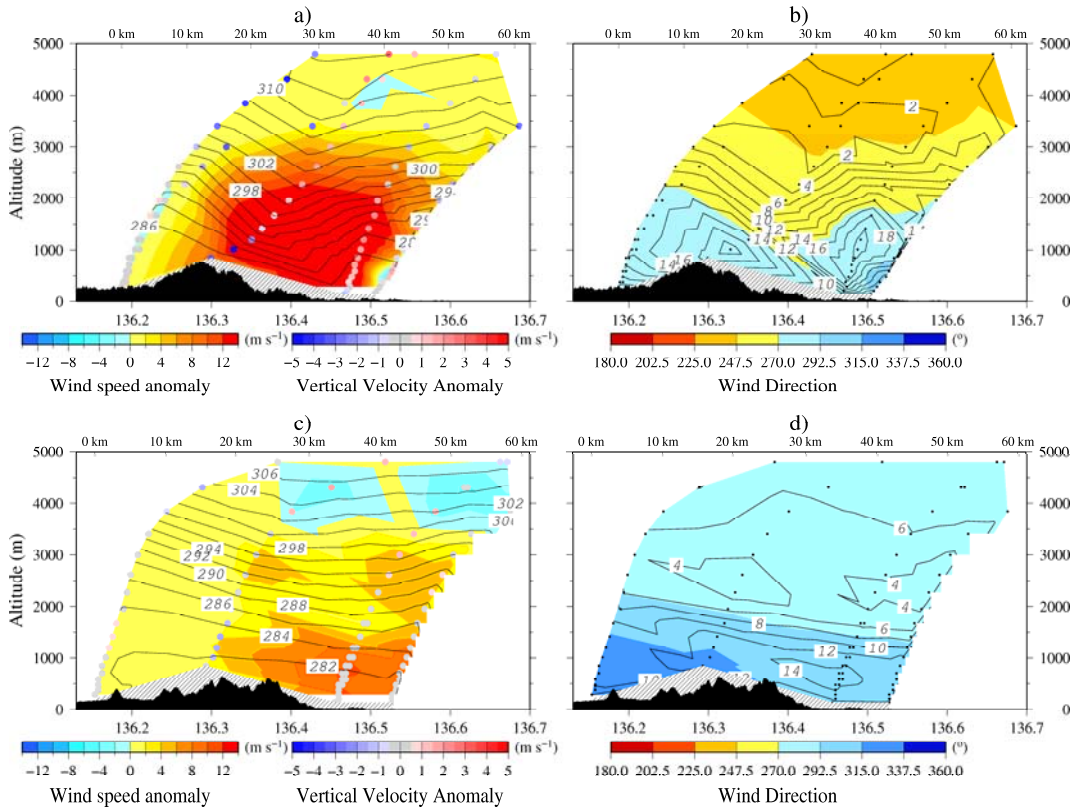

FIG. 1.15. Simulated longitudinal profiles showing (a) potential temperature (contours, interval 2 K), wind speed anomaly (color shade), and vertical wind anomaly (color dots) at 0530 JST, (b) wind direction (shade) and transverse wind component (contours, interval 2 m s^{-1}) at 0530 JST, (c) potential temperature, wind speed anomaly, and vertical wind anomaly at 1430 JST, and (d) wind direction and transverse wind component at 1430 JST.

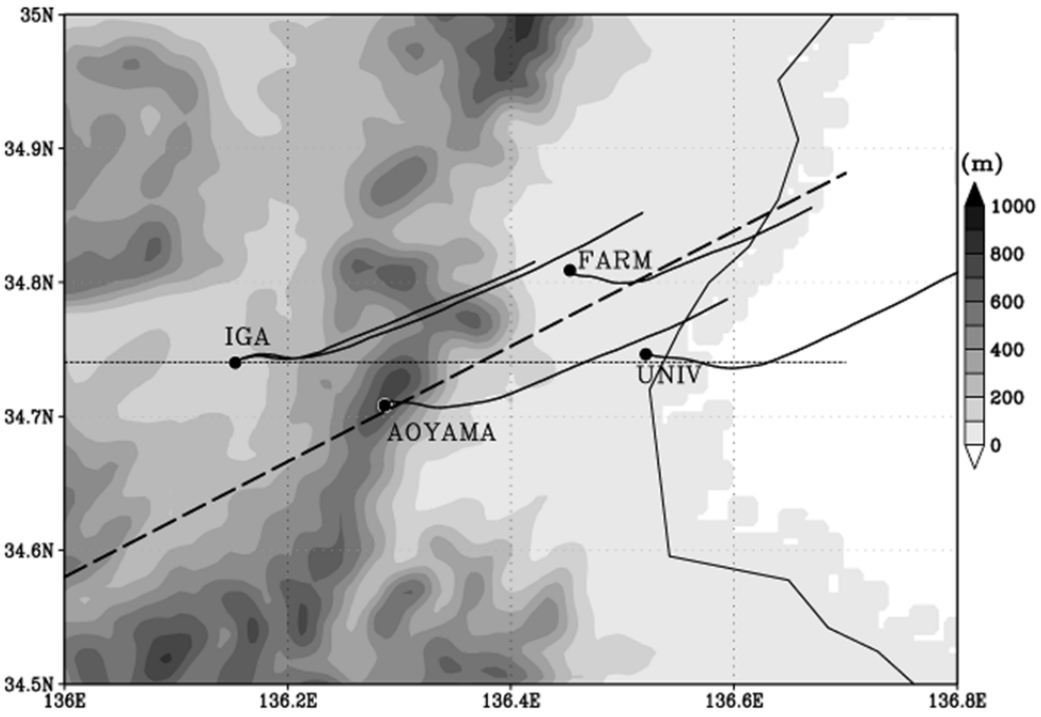

FIG. 1.16. Axes of the two altitude-longitude sections of Fig. 17. The dashed line is the same orientation as the plane in Fig. 3a, and the dotted line is an east-west line originating at IGA. The solid lines are the sounding trajectories. Gray shades represent topography.

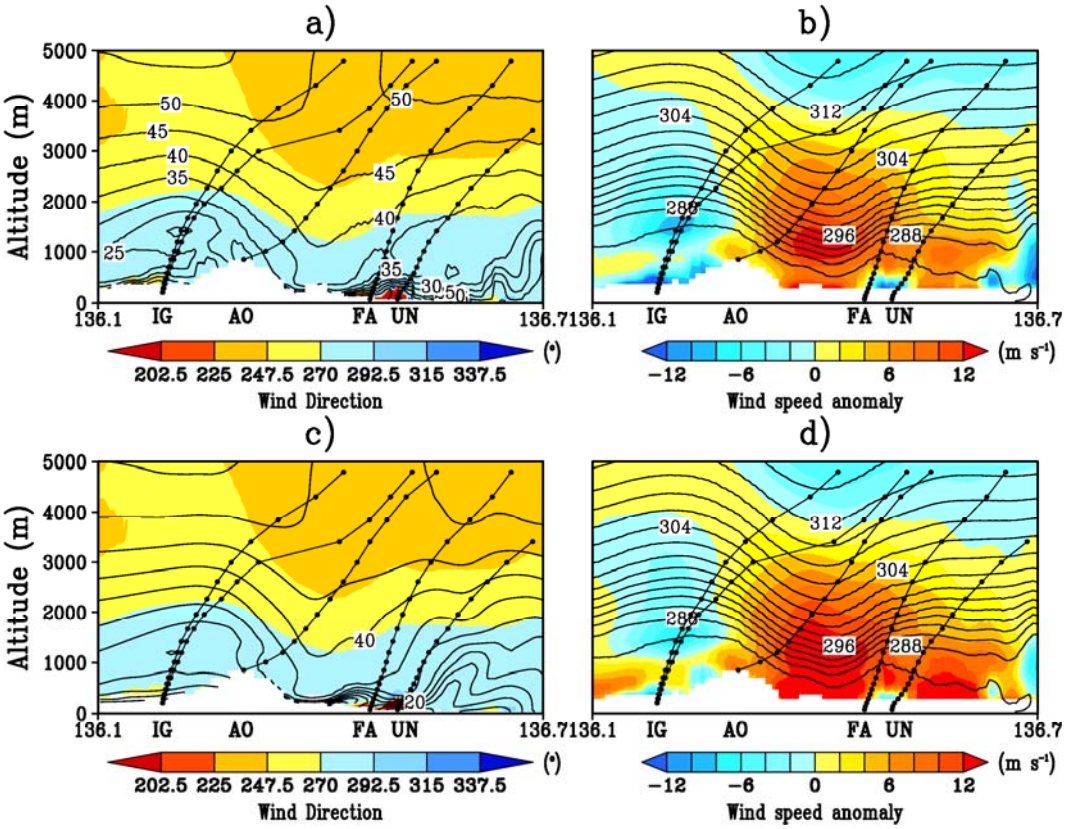

FIG. 1.17. Simulated altitude-longitude sections at 0530 JST along the two lines shown in Fig. 1.16. (a) Wind speed (contours, interval 5 m s^{-1}) and wind direction (color shade) and (b) potential temperature (contours, interval 2K) and wind speed anomaly with respect to wind speed at 136.1°E (color shade) along the orientation used for observations. (c) Wind speed and wind direction and (d) potential temperature and wind speed anomaly with respect to wind speed at 136.1°E along the east-west line. IG, AO, FA, and UN denote the locations of stations IGA, AOYAMA, FARM, and UNIV, respectively. Black dots and connecting lines approximate the radiosonde trajectories.

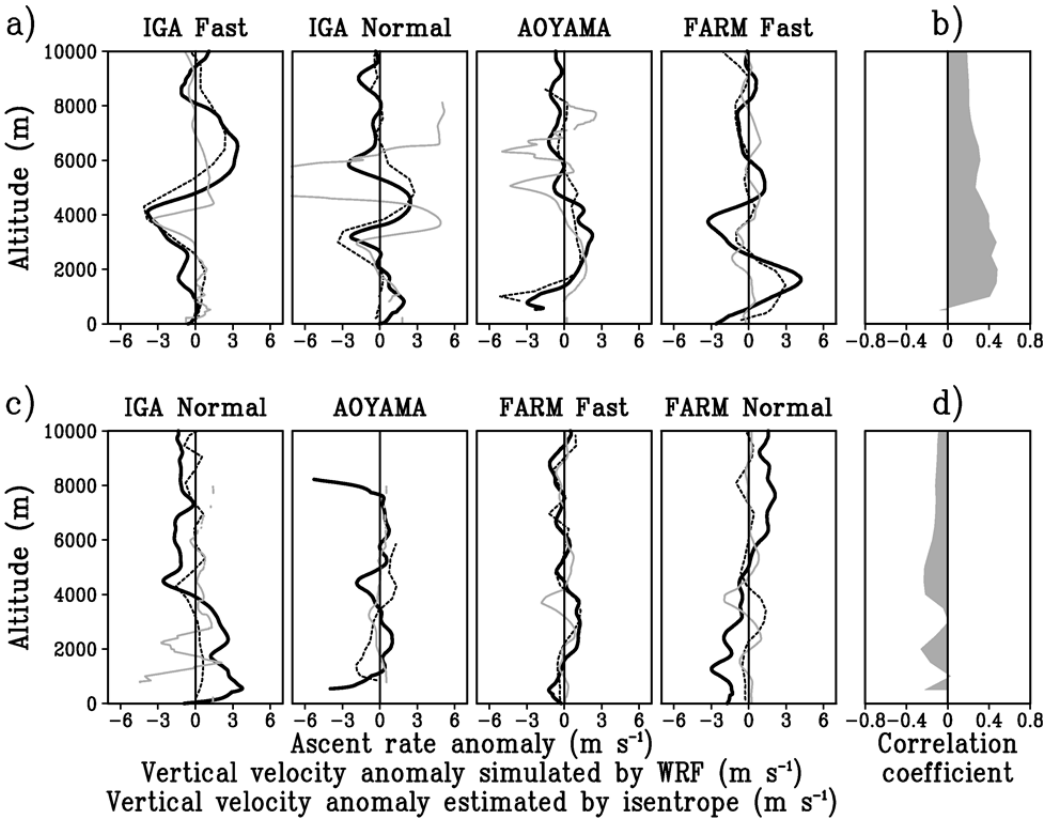

FIG. 1.18. (a) Vertical profiles of observed ascent rate anomaly (solid lines), isentropic vertical wind anomaly (gray lines), and simulated vertical velocity anomaly (dashed lines) at 0530 JST. (b) Correlation coefficient between observed ascent rate anomaly and isentropic vertical wind anomaly from the bottom to each level at 0530 JST. (c) Same as (a) for 1430 JST. (d) Same as (b) for 1430 JST.

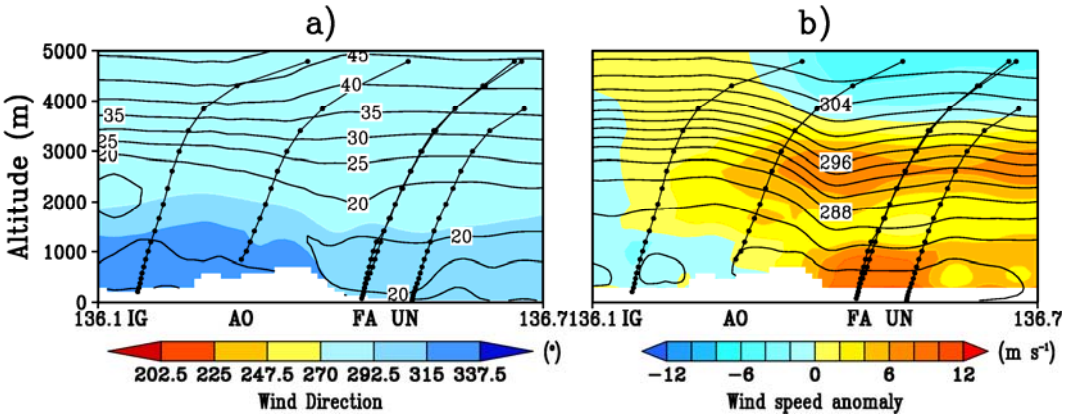

FIG. 1.19. Simulated altitude-distance sections at 1430 JST along the same orientation used for observations (Fig. 1.3b). (a) Wind speed (contours, interval 5 m s^{-1}) and wind direction (color shade) and (b) potential temperature (contours, interval 5 m s^{-1}) and wind speed anomaly with respect to wind speed at 136.1°E (color shade). IG, AO, FA, and UN denote the locations of stations IGA, AOYAMA, FARM, and UNIV, respectively. Black dots and connecting lines approximate the radiosonde trajectories.

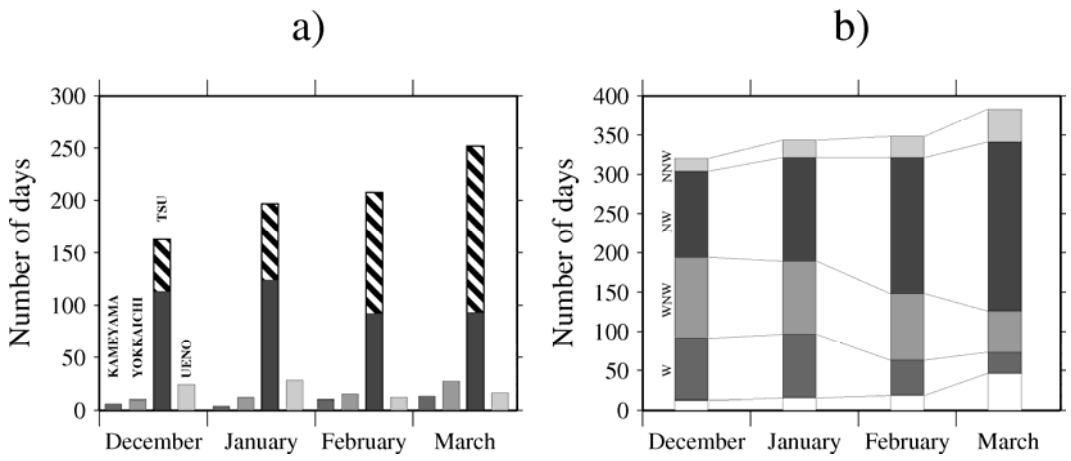

FIG. 1.20. (a) Number of days when hourly-mean wind speed exceeded 10 m s^{-1} during a day at stations Tsu, Kameyama, Ueno, and Yokkaichi during winter months of 1987–2011. Hatching indicates days of northwesterly winds. (b) Number of days when hourly-mean wind speed at Tsu exceeded the average wind speed at Ueno, Kameyama, and Yokkaichi by 5 m s^{-1} during winter months of 1987–2011. The wind direction is indicated by shading.

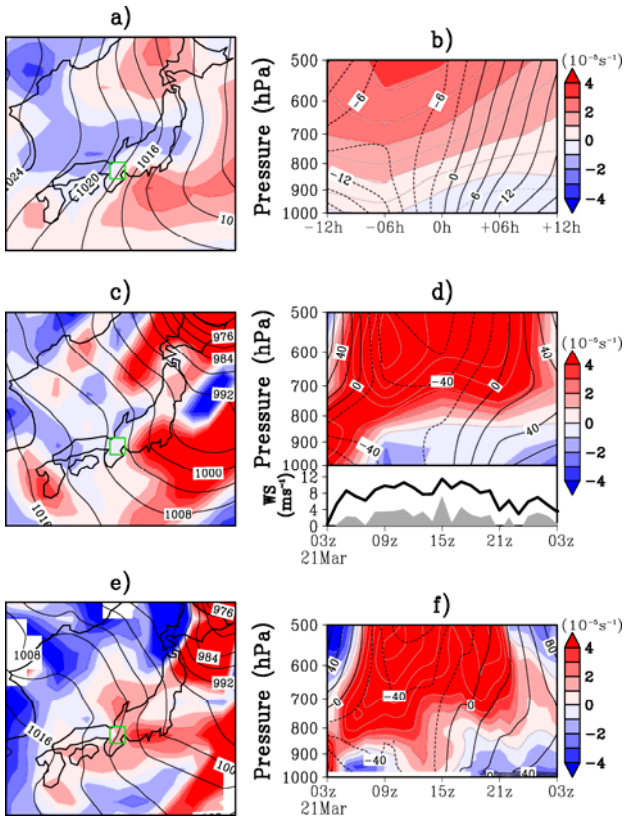

FIG. 1.21. Synoptic maps of the study area (left) and altitude–time sections at Tsu (right). (a) Average sea-level pressure (contours, interval 4 hPa) and relative vorticity at 925 hPa (color) on strong northwesterly days at Tsu (Fig. 1.20b). The green square indicates the grid cell nearest to Tsu in JRA25/JCDAS. (b) Average geopotential height anomaly (contours, interval 20 m) and relative vorticity (color) on strong northwesterly days. The 24-hour period is centered at the time when the wind-speed differential was greatest between Tsu and the average of stations Ueno, Kameyama, and Yokkaichi. (c) Observed sea-level pressure and relative vorticity at 925 hPa at 1500 JST 21 March 2010. (d) Observed geopotential height anomaly and relative vorticity from 0300 JST 21 March to 0300 JST 22 March 2010. Bottom panel is a time series of hourly-mean wind speeds at Tsu (black line) and the wind-speed differential between Tsu and the average of Ueno, Kameyama, and Yokkaichi (shade). (e) Simulated sea-level

pressure and relative vorticity at 925 hPa at 1500 JST 21 March 2010. (f) Simulated geopotential height anomaly and relative vorticity from 0300 JST 21 March to 0300 JST 22 March 2010.

1.7 References

Booker, D. R., and L. W. Cooper, 1965: Superpressure balloons for weather research. *J. Appl. Meteor.,* **4,** 122–129.

Chou, M. D., and M. J. Suarez, 1999: A solar radiation parameterization for atmospheric studies. *NASA Tech. Memo*, **15**, 40 pp

Corby, G. A., 1957: A preliminary study of atmospheric waves using radiosonde data. *Quart. J. Roy. Meteorol. Soc.,* **83,** 49–60, doi: 10.1002/qj.49708335505

Doyle, J. D., M. A. Shapiro, Q. Jiang, and D. L. Bartels, 2005: Large-Amplitude Mountain Wave Breaking over Greenland. *J. Atmos. Sci*., **62,** 3106–3126, doi: 10.1175/JAS3528.1

Durran, D. R., 1990: Mountain waves and downslope winds. *Atmospheric processes over complex terrain*. W. Blumen, Ed., Amer. Meteor. Soc. 59–81.

Durran, D. R., and J. B. Klemp, 1987: Another look at downslope winds. Part II: Nonlinear amplification beneath wave-overturning layers. *J. Atmos. Sci*., **44**, 3402-3412, doi: 10.1175/1520-0469(1987)044<3402:ALADWP>2.0.CO;2

Grisogono, B., and D. Belušić, 2009: A review of recent advances in understanding the meso-and microscale properties of the severe Bora wind. *Tellus A,* **61,** 1–16, doi: 10.1111/j.1600-0870.2008.00369.x

Grubišić, V., and Coauthors, 2008: The Terrain-Induced Rotor Experiment: A field campaign overview including observational highlights. *Bull. Amer. Meteor. Soc.*, **89,** 1513–1533. Doi

Hong, S. Y., Y. Noh, and J. Dudhia, 2006: A new vertical diffusion package with an explicit treatment of entrainment processes. *Mon. Wea. Rev.,* **134**, 2318–2341, doi: 10.1175/MWR3199.1

Iacono, M. J., J. S. Delamere, E. J. Mlawer, M. W. Shephard, S. A. Clough, and W.

D. Collins, 2008: Radiative forcing by long‐lived greenhouse gases: Calculations with the AER radiative transfer models. *J. Geophys. Res. Atmos.,* **113**, 1984–2012, doi: 10.1029/2008JD009944

Jiang, Q., and J. D. Doyle, 2004: Gravity Wave Breaking over the Central Alps: Role of Complex Terrain. *J. Atmos. Sci*. **61,** 2249–2266, doi: 10.1175/1520-0469(2004)061<2249:GWBOTC>2.0.CO;2

Johansson, C., and H. Bergström, 2005: An auxiliary tool to determine the height of the boundary layer. *Boundary-layer meteorology*, **115**, 423–432, doi: 10.1007/s10546-004-1424-5

Kain, J. S., 2004: The Kain-Fritsch convective parameterization: an update. *J. Appl. Meteor.,* **43**, 170–181, doi: 10.1175/1520-0450(2004)043<0170:TKCPAU>2.0.CO;2

Lilly, D. K., and E. J. Zipser, 1972: The Front Range Windstorm of 11 January 1972 a Meteorological Narrative. *Weatherwise*, **25,** 56–63, doi: 10.1080/00431672.1972.9931577

Lim, K. S. S., and S. Y. Hong, 2010: Development of an effective double-moment cloud microphysics scheme with prognostic cloud condensation nuclei (CCN) for weather and climate models. *Mon. Wea. Rev.,* **138**, 1587–1612, doi: 10.1175/2009MWR2968.1

Onogi, K., and Coauthors, 2007: The JRA-25 Reanalysis. *J. Meteor. Soc. Japan.* **85**, 369-432. doi: 10.2151/jmsj.85.369

Owada, M., 1994: *Atmospheric environment around Ise Bay.* The University of Nagoya Press, 219 pp. (in Japanese)

Owada, M., and K. Harada, 1978: Local climatological study on the Suzuka-oroshi in the Ise plain, central Japan. *Bull. Aichi University of*

Education Humanities and Social Science, **27,** 173–182. (in Japanese)

Reeder, M. J., N. Adams, and T. P. Lane, 1999: Radiosonde observations of partially trapped lee waves over Tasmania, Australia. *J. Geophys. Res. Atmos.,* **104,** 16719–16727, doi: 10.1029/1999JD900038

Reid, S. J., 1972: An observational study of lee waves using radiosonde data. *Tellus,* **24,** 593–596, doi: 10.1111/j.2153-3490.1972.tb01587.x

Reinecke, P. A., and D. R. Durran, 2008: Estimating topographic blocking using a Froude number when the static stability is nonuniform. *J. Atmos. Sci*., **65**, 1035–1048, doi: 10.1175/2007JAS2100.1

Saito, K., 1992, Shallow water flow having a lee hydraulic jump over a mountain range in a channel of variable width, *J. Meteorol. Soc. Japan*, **70**, 775–782, doi: 10.2151/jmsj1965.70.3_775

Saito, K., 1993, A numerical study of the Local Down slope Wind “Yamaji-kaze” in Japan Part 2 : Non-Linear Aspect of the 3-D flow over a Mountain Range with a Col, *J. Meteorol. Soc. Japan*, **71**, 247–272, doi: 10.2151/jmsj1965.71.2_247

Shutts, G., 1992: Observations and Numerical Model Simulation of a Partially Trapped Lee Wave over the Welsh Mountains. *Mon. Wea. Rev.,* **120,** 2056–2066, doi: 10.1175/1520-0493(1992)120<2056:OANMSO>2.0.CO;2

Shutts, G., and A. Broad, 1993: A case study of lee waves over the Lake District in northern England. *Quart. J. Roy. Meteorol. Soc.,* **119,** 377–408, doi: 10.1002/qj.49711951102

Shutts, G. J., P. Healey, and S. D. Mobbs, 1994: A multiple sounding technique for the study of gravity waves. *Quart. J. Roy. Meteorol. Soc.,* **120,** 59–77, DOI: 10.1002/qj.49712051506

Skamarock, W. C., and Coauthors, 2008: A description of the Advanced Research WRF version 3. Tech. rep., NCAR Technical Note, Boulder, CO, 125 pp

Smith, R. B., 1987: Aerial Observations of the Yugoslavian Bora. *J. Atmos. Sci*., **44,** 269–297, doi: 10.1175/1520-0469(1987)044<0269:AOOTYB>2.0.CO;2

Tewari, M., F. Chen, W. Wang, J. Dudhia, M. A. LeMone, K. Mitchell, M. Ek, G. Gayno, J. Wegiel, and R. H. Cuenca, 2004: Implementation and verification of the unified NOAH land surface model in the WRF model. 20th conference on weather analysis and forecasting/16th conference on numerical weather prediction, 11–15

Vergeiner, I., and D. K. Lilly, 1970: The dynamic structure of lee wave flow as obtained from balloon and airplane observations. *Mon. Wea. Rev.,* **98**, 220–232.

Vincent, R. A., S. J. Allen, and S. D. Eckermann, 1997: Gravity-wave parameters in the lower stratosphere. *In Gravity Wave Processes,* Springer Berlin Heidelberg, 7-25 pp.

Vosper, S. B., 2004: Inversion effects on mountain lee waves. *Quart. J. Roy. Meteorol. Soc.,* **130**, 1723–1748, doi: 10.1256/qj.03.63

Wang, J., J. Bian, W. O. Brown, H. Cole, V. Grubišic, and K. Young, 2009: Vertical air motion from T-REX radiosonde and dropsonde data. *J. Atmos. Oceanic Technol.,* **26,** 928–942, doi: 10.1175/2008JTECHA1240.1

Watson, D. F., 1982: ACORD: Automatic contouring of raw data. *Computers & Geosciences*, **8**, 97–101.

Wessel, P., W. H. F. Smith, R. Scharroo, J. F. Luis, and F. Wobbe, 2013: Generic Mapping Tools: Improved version released, *EOS Trans. AGU*, 94, 409–410.

Yoshino, M. M., 1975: *Climate in a small area: an introduction to local meteorology*. University of Tokyo Press, 549 pp.

Zhang, D. L., and R. A. Anthes, 1982: A high–resolution model of the planetary boundary layer– sensitivity tests and comparisons with SESAME–79 data. *J. Appl. Meteor.,* **21**, 1594–1609, doi: 10.1175/1520-0450(1982)021<1594:AHRMOT>2.0.CO;2

Chapter 2. Poleward upgliding Siberian atmospheric rivers over sea ice heat up Arctic upper air

2.1 Introduction

The fact that the Arctic is heating up faster than the rest of Earth, referred to as Arctic amplification [e.g. Serreze and Francis 2006, Serreze and Barry 2011], is one of the most significant global environmental concerns. Rapid Arctic warming occurs at the surface [Serreze and Francis 2006, Screen and Simmonds 2010], and numerous processes have been proposed as the causes of this amplification [Serreze and Barry 2011, Vihma 2014]. Whereas the positive feedback between sea-ice reduction and solar absorption seems to be the major contributor to the warming, numerical models in which albedo or sea surface temperature (SST) is kept constant nevertheless predict an amplified warming in the Arctic [Alexeev et al. 2005, Graversen and Wang 2009]. Arctic amplification occurs not only near Earth's surface but also throughout the troposphere during all seasons [Graversen et al. 2008, Screen and Simonds 2012]. One contributor to the mid-tropospheric warming is the changing poleward heat transport from outside the Arctic [Alexeev et al. 2005, Graversen et al. 2008, Screen and Simmonds 2012, Chung and Räisänen 2011, Yang et al. 2011]. Moisture is considered to be an important contributor to this enhanced poleward heat transport [Alexeev et al. 2005, Laliberté and Kushner 2013, Graversen and Burtu 2016] because water vapour absorbs longwave radiation and is the strongest greenhouse gas in the free atmosphere. Water vapour injection also strengthens Arctic amplification at the surface because of the increase of the downward flux of infrared radiation emitted by water vapour [Woods et al. 2013, Alexeev et al. 2017, Baggett and Feldstein 2016]. Poleward moisture transport is therefore a key process that contributes to

surface and mid-tropospheric Arctic warming.

Water vapour transport by transient eddies (i.e., packets of synoptic cyclones) dominates the total transport of water vapour into the Arctic [Oshima and Yamazaki 2004, Jakobson and Vihma 2010]. Evaporation from the surface of the North Atlantic and North Pacific Oceans accounts for much of the moisture in this poleward transport. These intensive northward movements of moisture in mid-latitudes have river-like structures and are referred to as Atmospheric Rivers; they carry large amounts of water vapour within narrow bands over oceans [Zhu and Newell 1998, Gimeno et al. 2014]. The narrow bands form filamentary regions within a warm conveyor belt ahead of the cold front of extratropical cyclones [Ralph et al. 2004, Ralph et al. 2005]. Recent studies of Atmospheric Rivers in the Atlantic and Pacific oceans have indicated that they contribute to the melting of the Greenland ice surface in summer [Neff et al. 2014] and Arctic surface warming in winter [Alexeev et al. 2017, Liu and Barnes 2015]. These two oceanic areas act as an important source of water vapour to the Arctic throughout the year, while North America and Siberia can also play a role as continental source regions in the summer[24]. The atmospheric water vapour and precipitable water over eastern Siberia has been increasing [Serreze et al. 2012], and a positive precipitation trend has also been observed during the summer [Fujinami et al. 2016, Hiyama et al. 2016]. In addition to these recent conditions favouring greater precipitation, atmospheric cyclonic circulation over northern Eurasia has strengthened [Iijima et al. 2016] in association with reductions of sea ice [Serreze et al. 2009]. These previous studies have suggested to us that cyclones from Siberia can transport water vapour to the Arctic and can enhance warming through a certain mechanism during the summer.

In addition to this widely accepted warming mechanism, we here propose an hypothesis about heating mechanisms that potentially contribute to the warming of the Arctic mid-troposphere during the summer viewing from a land-ocean-atmosphere interaction system (Fig. 2.1). The hypothesis is based on radiosonde observations conducted during an expedition in August 2013 from the Russian icebreaker "Akademik Fedorov". We document a new process, referred to as "Siberian atmospheric rivers", which injects moist, warm air from Siberia over the ice-free Arctic Ocean in association with cyclonic weather systems. Because the surface air temperature above sea ice tends to be fixed at about 0 ºC, a cool boundary layer capped by a strong temperature inversion forms in the lower troposphere over sea ice. This cold air near the surface maintains a meridional temperature gradient around the sea ice, and it blocks injection of Siberian atmospheric rivers into the cold boundary layer. This blockage of the boundary layer forces the Siberian atmospheric rivers to upglide. Poleward upglides of Siberian atmospheric rivers over the cold air dome overlying sea ice produce clouds that provide the upper atmosphere with heat via condensation of water vapour. This heating leads to increased buoyancy and further promotes ascent and heating of the mid-troposphere. These processes result in a coupling between the upper and lower atmosphere mediated by moisture injection from Siberian atmospheric rivers in interactions with local sea ice over the Arctic.

The present study focused mainly on documenting the existence of this process based on observations made from an icebreaker. First, we present observational signatures of an injection of warm, humid air over a near-surface cold air above the sea ice. Next, we show that a numerical simulation reproduces the phenomenon of Siberian atmospheric rivers gliding upward over the cold

dome. We also conducted numerical experiment with switching off of latent heat associated with cloud formation, an experiment without Arctic sea ice, and an experiment with a weakened Siberian atmospheric river to test the impact of different components of the model on the robustness of the mechanism. The experiment with switching off of latent heat can evaluate that the condensation of water vapour promotes an additional ascending and heating upper atmosphere. The experiment without sea ice can serve as an evaluation of the impact of near-surface cold air domes on the behaviour of Siberian atmospheric rivers. The experiment with a weakened Siberian atmospheric river can reveal the contribution of water vapour over land in Siberia to the Arctic mid-tropospheric temperature through the injection of the Siberian atmospheric river. Additional statistical analyses with a reanalysis dataset were used to document the historic existence of this process. We further compared the polar cap temperature change associated with Siberian atmospheric rivers between recent and past eras, but a quantitative assessment of the historic contribution of the proposed mechanism to Arctic warming is not a part of this paper.

2.2 Methods

a. Radiosonde launches

6-hourly radiosonde measurements were carried out from 06 UTC, 26 August to 00 UTC, 01 September, with trajectory starting in the ice-free ocean and ending in the ice zone in the Laptev Sea. Radiosonde launches were conducted from a Russian icebreaker "*Akademik Fedorov"* as a part of the 2013 cruise of the Nansen and Amundsen Basins Observational System program.

To obtain a uniform vertical resolution of the radiosonde data, we averaged the data vertically over intervals of 20 m and then smoothed the data by the weighted running mean over intervals of 100 m to remove small perturbations. The ocean temperature was sampled by a conductivity temperature depth profiler (CTD) along the sounding line. A sonic anemometer, mounted on the icebreaker, measured the turbulent heat flux between the air and sea ice surface.

b. Reanalysis product dataset and the detection of the Siberian atmospheric river

A gridded atmospheric reanalysis dataset, ERA-Interim, supplied by the European Centre for Medium-Range Weather Forecasts [Dee et al. 2011], is used. The reproducibility of reanalysis products over the Arctic without in situ shipboard radiosonde observation stations is uncertain, and the values of such datasets differ from those of other products [Inoue et al. 2011]. We verified that the ERA-Interim reproduced the observational results well. ERA-Interim is also used for climatological analyses in the period from 1979 to 2013.

Several methods of detecting atmospheric rivers have been proposed, using

both satellite data and reanalysis products [Gimeno et al. 2014]. The IVT is also often used as a detector of atmospheric rivers, which are typically detected by identifying contiguous regions ≥ 2000 km in length with IVTs ≥ 250 kg m^{-1} s^{-1} in mid-latitude regions. This study uses the IVT values to identify atmospheric rivers using the same methods as previous studies [Neiman et al. 2008, Lavers et al. 2012]; the horizontal moisture flux multiplied by the specific humidity of the zonal and meridional wind components is integrated from 1000 hPa to 300 hPa. To identify Siberia atmospheric river, we checked the daily mean IVT map during summer season (June, July and August) between 1979 and 2013. This identification shows that the IVT over 200 kg m^{-1} s^{-1} can be used as a threshold for capturing the river-like shape of IVT over the Siberian region, but it is not always promise the atmospheric river. The development of more quantitatively detection is beyond the scope of this paper.

c. Numerical simulations

The numerical experiments are based on the polar-optimized version of the Weather Research and Forecasting model [Skamarock et al. 2008, Hines et al. 2015] version 3.5.1, called the Polar WRF. The simulation area, covering the entire Arctic Ocean and expanding into central Siberia, is set on a 561 × 406 polar stereographic grid with a horizontal grid spacing of 10 km and 69 vertical levels, reaching 50 hPa. The simulation is integrated from 12 UTC on 25 August with 40 second time steps. The initial and lateral boundary conditions are supplied by ERA-Interim, which operated every 6 hour on 37 pressure levels, gridded at 0.75°. Bootstrap sea ice concentration from Nimbus-7 SMMR and DMSP SSM/I-SSMIS [Comiso 2015][46] are adopted as the sea ice concentration and boundary condition.

The sea ice thickness is fixed at 2 m. The sea surface temperature (SST) is obtained from the National Oceanic and Atmospheric Administration (NOAA) daily Optimum Interpolation SST version 2 [Reynolds et al. 2007], which is gridded at 0.25°. The choice of physical parameterization is based on previous literature [Hines et al. 2015], but the cumulus parameterization is not used in the simulation.

The experiments were categorized as a control run (CTL), a switching off a latent heat run (DRY), an ice-free run (NoICE), and a reduced Siberian humidity run (RHcut). The CTL was executed under realistic boundary conditions, as shown in the previous paragraph. The DRY turned off an exchange of latent heat through a microphysics after 08 UTC on 29 August at the model time. In this run, the phase change such as a cloud forming occurs by the same manner as in CTL but the latent heat does not released to the atmosphere. The NoICE was executed without the Arctic sea ice in order to observe the influence of the sea ice. The surface boundary condition of the NoICE is that the sea ice for the whole Arctic Ocean was removed, and SST was fixed to the constant value of 4 °C for the area poleward of 65° N. In addition, the air temperature in the initial conditions of the lower troposphere is modified using a simple linear function to

$$\boldsymbol{T_P = \frac{T_{500} - T_{850}}{350}\Delta \mathbf{p} + T_{850}} \qquad (\mathbf{1})$$

Here, T_P is the air temperature (°C) at a pressure level P (hPa). T_{500} and T_{850} are the temperatures at 500 hPa and 850 hPa, respectively. Δp is the pressure difference between 850 hPa to the level of P. This modification is applied from the surface to 850 hPa poleward of 70° N in order to remove the unwanted cold domes from the initial atmospheric conditions. The specific humidity in the NoICE was the same as that of the CTL. The other boundary conditions and the

other initial conditions are also the same as those of the CTL.

For the RHcut, the initial condition of the water vapour above central Siberia, westward of 125° E and south of 64° N, was reduced to one-third of the CTL. Furthermore, the moisture advection from the lateral boundary in this region was set to zero. The initial conditions of the water vapour in the other areas, such as over the Arctic Ocean were the same as in the CTL. The other boundary conditions and the other initial conditions are also the same as those of the CTL.

d. Trajectory analysis

Backward and forward trajectories of the air parcels were calculated by Read/Interpolate/Plot version 4.5. The initial time for the calculation of the trajectories was set to 08 UTC on 29 August. This time was 2 hours later from the actual sounding sample time because the model output at 08 UTC on 29 August was closer to the observation at 06 UTC on 29 August than the model output at the same time. The trajectories of the air parcels initiated at 17 levels (0.13, 0.21, 0.29, 0.38 0.47, 0.59, 0.72, 0.86, 1.03, 1.24, 1.47, 1.75, 2.08, 2.47, 2.92, 3.45, and 4.05 km) over the sounding point were calculated for the preceding 72 hours and the following 36 hours at 30 minute intervals. To evaluate the trajectories of the atmospheric flows from Siberia to the Arctic in RHcut and in CTL, we arranged 500 air parcels at 6 levels (0.5, 1, 2, 3, 4, and 5 km) above central Siberia (small square in Fig. 2.8c). This area is around the origin of the Siberian route in Fig. 2.4b, and the trajectories of the parcels of the 108 hours preceding 08 UTC on 26 August were calculated.

e. Identification of cold air dome

To identify a cold air dome associated with the sea ice, we assumed that the surface of cold air was characterized by the height of an isentropic surface of 278.4 K because the most of the upper air parcels of the Chukchi Sea route arriving at the observation point were lower than this potential temperature with passing over the observation point (Fig. 2.4a). Figure 2.5b shows the horizontal map of time-mean height of the isentropic surface at of 278.4 K estimated by the averaged potential temperature during 06 UTC on 26 and 18 UTC on 31 August. The vertical thermal structures averaged by two regions -- one is the whole area of cold air identified by isentropic surface, and the other is the Laptev Sea (quarter sector in Fig. 2.5b). A strongly stratified layer at about 400 m with large change of relative humidity is seen in the two regions, and they match well to the observed mean structure. Relatively small increase of the potential temperature with height is seen from the surface to at the stably stratified layer formed under the level of 0.5 km for the dry adiabatically, but this layer was saturated. Therefore we can consider this layer as a well- mixed layer for moist adiabatically. The isentropic height surface of 278.4 K averaged in the whole cold air region is located at the nearby the top of the temperature inversion layer (about 0.8 km), which is considered as the interface between the upper free atmosphere and lower Arctic air mass. The isentropic height surface of 278.4 K averaged over the Laptev Sea area is located at near the bottom of the temperature inversion layer, which is the boundary of the warm air advection from outside of the Arctic. These signify that the isentropic surface of 278.4 K can be used as the threshold to roughly distinguish between two air masses.

f. Composite analysis

We used daily mean ERA-interim fields during the summer season (Jun, July and August) between 1979 and 2013 for statistics. To make the composite maps averaged for similar events as our observational period, we firstly defined the normalized daily index associated with the moisture injection to the Laptev Sea which is averaged the vertically integrated meridional moisture flux passed among 100^{o} E and 140^{o} E at 75^{o} N (see Fig. 2.9b). Differences during our observational period exceeded two standard deviations in this definition. Based on this index, we chose the day of anomalous moisture injection which had the highest value around the 5th days with exceedance of one standard deviation. This procedure selected 147 cases in 105 month as the composite members. Finally, we averaged the composite members with 2 day mean and additionally made two kinds of the composite map; one is with 2 days lead and second with 2 days lag. These composite maps depict the transition of synoptic atmospheric condition associated with the anomalous moisture injection events. For remove the global warming signal, the composite members are de-trended at each grid point for long term linear trend estimated by least-squares method in advance. Additionally we evaluate the sensitivity of the Siberian atmospheric rivers in situations when the sea ice decreased. Firstly we estimated the normalized index associated with the inter-annual variability of the summer time mean sea ice concentration over the coastal area in the Laptev Sea by using the three month mean (June, July and August) Bootstrap sea ice concentration from Nimbus-7 SMMR and DMSP SSM/I-SSMIS. The summer time mean sea ice concentration was defined by the area average squared by 75^{o} N ~ 80^{o} N and 100^{o} E ~ 140^{o} E. Based on this index we divided 147 cases to two groups; positive ice year and negative ice year. The

positive ice year contained 73 cases in 19 years (79, 80, 81, 82, 83, 84, 85, 86, 87, 89, 92, 93, 94, 96, 97, 98, 01, 04, 08), and the negative ice year contained 74 cases in 16 years (88, 90, 91, 95, 99, 00, 02, 03, 05, 06, 07, 09, 10, 11, 12, 13). The positive and negative ice year almost corresponded with the past and recent years, respectively. Finally we averaged all the cases for both groups to make composite maps and calculated the anomaly subtracted positive year from negative year. The temperature tendency is also evaluated the difference of the temperature from 2 days before for all cases. The statistical significance is estimated using Student's *t*-test.

2.3 Results

a. Observational results

We carried out 6-hourly global positioning system radiosonde measurements from 06 Coordinated Universal Time (UTC) on 26 August to 00 UTC on 01 September, during which time we observed Arctic sea ice from the ice-free ocean in the Laptev Sea (Fig. 2.2a). Figure 2.2b and 2.2c show atmosphere-ocean vertical sections recorded during our observations. The cross section in the period 26–29 August corresponds to a vertical-latitudinal section from the ice-free ocean to the sea ice zone transecting the ice edge. The change of air temperature near the surface during 26–29 August generally matched well with that of the underlying ocean: the air temperatures below an altitude of approximately 0.5 km above the sea ice were low, whereas the temperatures at the same altitudes over the ice-free ocean were relatively high (Fig. 2.2b). The temperature of the cold surface air over the sea ice stayed nearly constant, and a pronounced temperature inversion formed above the cold air under high surface pressure conditions until 12 UTC on 28 August. At the same time, high relative humidity was capped at the height of the temperature inversion, except for the night of 27 August (Fig. 2.2c). These thermal structures were similar to the dominant thermal structure in the Arctic documented by previous expeditions [Tjernström et al. 2004, Tjernström 2005, Tjernström et al. 2015]: namely, the formation of a well mixed boundary layer with high relative humidity up to a height of 500 m. This well-mixed boundary layer is formed by a process that involves transformation of air masses. Warm air masses intruding from the continent to the sea-ice region are cooled by the release of heat to melt sea ice, and they are transformed into a shallow, well-mixed boundary layer capped by a temperature inversion[33].

After 12 UTC on 28 August, very warm, humid air was observed centred at a height of approximately 1 km, and on 29 August the surface pressure was decreasing. This warm, humid air, which extended to an altitude of approximately 4 km, matched well with the increase in the southerly wind. In contrast, the air temperature near the surface over the sea ice did not rise continuously with downward turbulent heat fluxes. As a result, a strong vertical temperature inversion layer formed. The cloud top height defined by high relative humidity, however, penetrated beyond the temperature inversion layer (Fig. 2.2c and Fig. 2.3). The vertically integrated horizontal water vapour transport (hereafter called the integrated water vapour transport [IVT]; Methods) increased from 12 UTC on 28 August, with the maximum value reaching 344 kg m^{-1} s^{-1} at 06 UTC on 29 August (Fig. 2.2c). This value was more than triple the IVTs on 26 and 31 August.

Synoptic atmospheric conditions for the same time period (Fig. 2.2d) were determined using the gridded reanalysis product dataset ERA-Interim [Dee et al. 2011][34]. The reproducibility of the reanalysis was confirmed via comparisons with observations. Cyclonic and anticyclonic systems were located on the western and eastern sides of the sounding point. An elongated IVT with a maximum greater than 200 kg m^{-1} s^{-1} extended from central Siberia; it covered a large area and was shaped like an atmospheric river. An IVT is much stronger in this state than in its basic state at high latitudes, but its strength is less than the threshold used to determine atmospheric rivers in mid-latitudes [Neiman et al. 2008, Lavers 2012] because the base amount of water vapour at high latitudes is generally less than that at mid-latitudes. At the same time, a warm region, corresponding to a large IVT, extended from central Siberia to the centre of the Arctic (Fig. 2.2e). The injection of moist, warm air was therefore generated by the northward progression

of an IVT resembling a river and trailed by a cyclonic weather system. A recent paper has shown that atmospheric rivers are maintained by convergence within them and local evaporation around a cyclone [Dacre et al. 2015]. At the same time, an IVT resembling a river does not always mean that the water is transported from far away along the IVT [Bao et al. 2006]. To examine the origin of the air masses associated with the moist, warm injection, we carried out a numerical experiment using *Lagrangian* trajectory analysis of air parcels.

b. Numerical simulation and trajectory analysis

We executed a numerical simulation to reproduce the cyclonic episode captured by in situ observation (the design of simulation is in Methods). The simulated values are almost identical to those observed. The trajectories of the air parcels above a sounding point over the sea ice showed two pathways; one from Siberia at altitudes above 0.5 km, and the other from the Chukchi Sea at altitudes below 0.5 km (Fig. 2.4a and b). The vertical structure observed at 06 UTC on 29 August apparently showed the warm air intrusion from continental side by south-easterly wind, but the upper warm and lower cold air masses had quit different origins.

The Siberian route is overlapped by the large IVT area (Fig. 2.4c). This large IVT area could be an atmospheric river transporting water from central Siberia to the Arctic. The air parcels travelling along this route generally followed higher routes over the 12 hour period, and continued rising to further higher levels expect that lower several parcels trapped in the temperature inversion layer (Fig. 2.4a). The vertical time sections along the trajectory of an air parcel originating at 1.2 km above the sounding point (Fig. 2.4d, e and black line in Fig. 2.4c) show the

movement of high specific humidity, i.e., over 5 g kg^{-1}, from land to the Arctic at altitudes below 2 km, and its upward glide over the cold air (light blue shade in Fig. 2.4d). The upward and poleward upgliding of the humid air parcels further promoted the formation of additional upper–level stratus clouds above the low-level clouds (Fig. 2.4e), and they released latent heat into the atmosphere through the condensation of water vapour (Fig. 2.4d). The air parcels, forced to warm via heat release due to condensation, can travel to even higher levels across isentropic lines. This upward slantwise motion after upglide over surface cold air is similar to warm air motion over a warm front associated with the atmospheric river.

In contrast, the air parcels from the Chukchi Sea was confined in the cold air mass and they continued traveling at the same levels after passing the sounding point as before (Fig. 2.4a). The origin of the clockwise Chukchi Sea route was an anomalous cold air region associated with an anticyclonic system over the sea ice on East Siberian Sea (Fig. 2.2e). The tracking of an air parcel initiated at 0.3 km (Fig. 2.4f, g and blue line in Fig. 2.4c) shows that the air parcel was trapped by the strong temperature inversion layer and crawled to the sounding point forming the low-level clouds (Fig. 2.4f and g). The vertical thermal structures along this trajectory were similar to the dominant thermal structure in the Arctic[32], thus the source of surface cold air was over the sea ice rather than over the continent. The isentropic lines below 1 km were gradually descending toward the sounding point with time, indicating that the height of the cold air mass was shrinking via heating from the land and ocean surface and warm air advection. The declining of isentrope was, however, inhibited over the sea ice, thus the cold air masses were kept cold by the sea-ice cooling. These results imply that a cold air dome is

associated with sea ice located over the Arctic Ocean.

In addition to these *lagrangian snapshot-like* views, we show time-averaged ones (Fig. 2.5). The upglide signature seen by cloud water and ice mixing ratio is also detected in time-averaged fields; clouds between 1.2 km and 4km were extended to the higher latitudes along with the strong south-easterly wind from around sounding point (Fig. 2.5a) and this structure can be seen in zonally averaged vertical section (Fig. 2.5b). Dome-like structure of surface cold air mass characterized by an isentropic surface at 278.4K are also seen in Fig. 2.5c (definition of the cold air mass are in Method). Cold air covered not only within the sea-ice region but also spreaded over the whole Arctic Ocean, and strong meridional gradient of the height of the isentropic surface was around the land-ocean boundary. Moreover, we can identify the shape of the cold air like a convex dome centred over the north of the Chukchi Sea, and its peak height reached over 1 km. Over the Laptev Sea, the southerly wind blew along the slope of the cold dome with gaining its altitude, where the release of the condensation heat and the drop of the specific humidity are seen (Fig. 2.5c and d). The prominent condensation heating was also identified at the southern part of the observation points, corresponding with the ice edge rather than the land-ocean boundary. This implies that the warm-humid air mass coming from the outside of the Arctic frequently saturated aloft there with gliding along the slope of isentropes during the observation period because these features were seen by the time average, not by the temporary.

In summary, warm air from Siberia brought by a cyclonic system collided with the area of the cold air dome, which acted like a barrier, and the warm air was forced to glide up over the cold dome. This structure appears to be similar to a

mid-latitude synoptic-scale frontal system. Although the structure appears similar, the contribution from the surface conditions is different: The mid-latitude frontal systems do not necessary develop because of surface conditions such as SST gradient, while, in our case, the surface cooling condition was essential.

c. Sensitivity experiment

Next, we executed numerical experiments with switching-off the latent heat release (DRY), the ice-free ocean surface (NoICE) and reduced Siberian humidity runs (RHcut). In DRY, we switched off the latent heat release after 08 UTC on 29 August, at which forward trajectory calculation stated. In NoICE, the SST, which is a surface boundary condition, was fixed at 4 ^{o}C in the whole Arctic Ocean, and a preexisting cold dome was broken in order to suppress a cold dome development. In RHcut, we extremely reduced the water vapour above land in Siberia (see Methods). Comparisons of the aforementioned simulation (Control run: CTL) with DRY, NoICE, and RHcut further support the process illustrated in Fig. 2.1.

The DRY demonstrates the contribution of latent heat to the upglide and heating the Arctic upper air. No prominent upglides as in CTL were seen in the trajectories of DRY (Fig. 2.6a). Thus the thermal forcing associated with condensation dominantly activated the upglide rather than dynamical forcing such as a large-scale vertical motion. Moreover, a cyclone system in CTL was stronger than in DRY (Fig. 2.6b). Time vertical section following the air parcel (Fig. 2.6c) signifies that the rising of air parcel in CTL started with releasing the latent heat and forming the cloud after 6 h, and the temperature anomaly from DRY reached about 1 K in the cloud. After that, the vertically stepwise temperature anomalies

developed parallel to the top of cloud forming, and the temperature anomaly maxima reached over 3 K. Positive temperature anomalies were also seen between 0.5 and 1 km height, which could contributed to the strengthen of a temperature inversion layer. The strengthened inversion layer hardly trapped the lower air parcels inside its layer and tended to divide the lower and upper air masses (see Fig. 2.4a and 2.6a). These thermal structures forced by condensation were also seen by the zonally averaged latitudinal-vertical section (Fig. 2.6d). The peak of positive anomalies is located between 2 and 3 km height in higher latitudes along with those of lower latitudes. The peaks in higher latitudes correspond with the top of a cloud layer, which is similar structure to those along an air trajectory showing in Fig. 2.6c.

The differences between the NoICE and CTL demonstrate the role of sea ice in this process. The vertical displacements of trajectories in the NoICE differed from or were in the opposite direction to those of CTL (Fig. 2.7a and b): the air parcels below 1 km travelled at constant levels from approximately 12 hours before the observational point of the sounding and 36 hours after without rising, also the upper air parcels moved downward with time rather than upward. The atmosphere above 1 km in the NoICE was simulated as more likely to be cold and dry than that of CTL (middle panel in Fig. 2.7b). In addition, the weakening of the cold dome can lead to weaker baroclinicity over the Arctic Ocean thus the cyclonic system in NoICE could not develop as strong as in CTL (Fig. 2.7c and bottom panel in 2.6d). The trough of sea level pressure in CTL was deeper than NoICE over the Laptev Sea, thus intensified zonal pressure gradient strengthens poleward wind, which encourages the transportation of the warm and humid air mass to higher latitudes (Fig. 2.7c). The centre of the cyclonic system in CTL also

located more northern than NoICE (Fig. 2.7d). The latitudinal vertical section of anomalies of potential temperature and specific humidity indicate that the CTL was warmer and wetter than NoICE in upper levels in high latitudes (Fig. 2.7d). Above 2 km height, positive and negative temperature anomalies in CTL were seen in the northern and southern parts of the cyclonic system respectively. This northern warm and southern cold pair is apparently corresponded with the intensification of the cyclonic system by the existence of the cold air dome. In addition, cloud associated upglide of air parcel was less in NoICE than CTL, and positive anomalies of cloud water and ice mixing ratio in CTL was seen bottom of the positive temperature anomalies (Fig. 2.7d and 2.7e). This implies that weakening the cold air dome damps the cyclonic system, and inhibits the intrusion and upglide of Siberian atmospheric river to the poleward side.

The reduction in water vapour above Siberia resulted in two effects: the weakening of the Atmospheric Rivers and the cyclonic system (Fig. 2.8a and b). The map of time averaged IVT in RHcut resembled a river, but the penetration of the Atmospheric river into the high latitudes was reduced (Fig. 2.8b). The horizontal pathways of air parcels released at 1 km over Siberia in the RHcut showed that the air parcels travelled to the Arctic and rose a level at the ice edge (Fig. 2.8c). The composite vertical displacements, which were derived from averaging trajectories released at each level are shown in Fig. 2.8d: the air parcels that originated below 2 km rose, reaching 4 km in the CTL, whereas in the RHcut, they rose less. We constructed a composite *Lagrangian* vertical time section along 500 trajectories initiated at 1 km over Siberia (see black square of Fig. 2.8c). The middle troposphere, between 3 km and 7 km above the sea ice, was drier and colder in RHcut than in CTL (the latter 60 h shown in Fig. 2.8e). Precipitable

water, which is the vertically integrated specific humidity between 750 hPa to 300 hPa, decreased above the Arctic by up to −0.7 kg m^{-2} in the RHcut from that observed in CTL. The negative anomalies of the condensation heating also corresponded to the negative anomalies of temperature and specific humidity (Fig. 2.8f). In the latter 72 hours, the condensation heating in RHcut was inactive throughout the middle troposphere, with a vertical integral between 750 hPa and 300 hPa reduced by up to −0.12 K h^{-1} compared to CTL. These differences imply that the reduction of water vapour source above central Siberia can result in cooling of the middle troposphere of the Arctic.

This section tested the contribution of each component -- latent heat, cold air dome associated with sea ice, and the water vapour over the Siberia -- to the process illustrated in Fig. 2.1. All the elements contributed to the heating upper air over the Arctic through the intensification of a cyclonic system with poleward upgliding of Siberian atmospheric river. These results suggest that the interaction of land-ocean-atmosphere could amplify the Arctic upper air temperature through the modification of a cyclonic system.

d. Statistical analysis

The observational and numerical results imply that the water vapour was transported by a cyclonic system that injected moisture in a form that resembled a river from central Siberia toward the Arctic Ocean. To demonstrate that the injections have occurred in the past, we executed additional statistical analyses using a reanalysis product. We also evaluated the temperature rise over the Arctic during the recent era as compared with the past, when Siberian atmospheric river events occurred (details are in Methods).

Figures 2.9a–f show the transition of daily composite maps of sea level pressure, IVT, and vertically integrated moisture flux during the time when an anomalous northward meridional moisture flux crossed the coast of the Laptev Sea. We found 147 days with Siberian atmospheric river episodes during the summer (June, July, and August) between 1979 and 2013, an indication that intense moisture intrusions occur at least once per month. When an anomalous moisture intrusion occurs, a cyclonic system tends to move from the northern coast of central Siberia to the centre of the Arctic Ocean and to pass on the west side of the Laptev Sea (Fig. 2.9a, b, and c). A pair of cyclonic and anticyclonic systems is also apparent, a pattern quite similar to our observations (Fig 2.2d and 2.9b). Eastward moisture flux and a large IVT area are always apparent on the west side of Siberia (Fig. 2.9d, e, and f). Along with the movement of the cyclonic system, the large IVT area expanded to the Arctic Ocean from central Siberia and formed a flow resembling a river directed toward the central Arctic (Fig. 2.9e and f). These features look very similar to the features that we observed. The observational and numerical results thus depicted a typical case of Siberian atmospheric rivers.

We next evaluated the sensitivity of the Siberian atmospheric rivers in situations when the sea ice decreased (Methods). We divided the members of the composite into two groups associated with the inter-annual variability of the summer sea-ice concentration in the coastal area of the Laptev Sea (the region was 75–80ºN, 100–140ºE); one group was taken from the years of positive ice anomalies, and the other group was taken from the years of negative ice anomalies. This separation corresponded closely to the distinction between past and recent years. We averaged the zonal mean temperature over the Arctic in positive and

negative years with eliminated the long-term linear trend. Figures 2.9g–i show the anomaly of zonal mean temperature in negative years compared to positive years during Siberian atmospheric rivers episodes. The recent warming signals were retained, but the positive temperature anomaly in the troposphere was increasing with time. This signal implies that the Arctic troposphere tended to be warmed more by the injection of Siberian atmospheric rivers in the years when the sea ice over the Laptev Sea was below normal. We also compared the temperature tendencies during Siberian atmospheric river episodes (Fig. 2.9j, k, l). The positive anomaly of temperature tendencies, corresponding to the growth of the positive temperature anomaly (Fig. 2.9i), tilted northward with height between 75ºN and 85ºN (Fig. 2.9l). A weak statistical significance was apparent in the lower troposphere above 75ºN and in the middle troposphere above 80ºN. This tilted warming pattern might reflect upglide heating by the Siberian atmospheric rivers because the front of the surface cold dome during negative ice years was located around 80ºN. These results led us to conclude that the Siberian atmospheric rivers are potentially an important contributor to the recent Arctic tropospheric warming.

2.4 Discussion and conclusion

This paper documented the existence of Siberian atmospheric rivers on the basis of observational, numerical, and statistical analyses. Numerical simulations indicated that our observations captured one of the episodes of upglides of Siberian atmospheric rivers over the near-surface cold dome. The historical analysis suggests that this process is not unusual and in fact quite common. In addition to the upglide process, there is a possibility of an air mass transformation process [Tjernström et al. 2015], which would be able to keep the boundary-layer air mass cool because of the underlying sea ice, even if the intruded warm air were partially entrained into the boundary layer. The cooling process by melting of sea ice [Tjernström et al. 2015] enables the cold air dome to spread out the ice-free area in a ice-melting season, although the formation and maintenance processes of the cold air dome is beyond the scope of this study. The proposed concept of the upglides over the cold air dome has similar condition to the occurrence of mid-latitude diabatic Rossby waves [Boettcher and Wernli 2013, Parker and Thorpe 1995], in which the positive low-level potential vorticity anomaly induces a poleward low-level jet of warm moist air at its downstream side. This stream ascends along the poleward-sloping isentropes until condensation occurs [Boettcher and Wernli 2013].

The sensitivity experiments revealed that both the presence of sea ice and a sufficient supply of moisture from Siberia are important factors in the formation of upglides of Siberian atmospheric rivers. In all the experiments, the cyclonic intensity was weaker than during the CTL. Both atmospheric rivers and sea ice strengthened the cyclonic system, and they strengthened the tropospheric heating by strengthening the cyclone system. These results imply that a poleward gradient

of surface thermal conditions such as sea-ice concentrations has an influence on synoptic-scale cyclone activity. A similar influence of a surface thermal gradient on synoptic-scale cyclone activity has commonly been found over mid-latitude regions where there are large south-north SST gradients, such as the Kuroshio Current and Gulf Stream [Hirata et al. 2016, Minobe et al. 2008]. Because this sea-ice-induced thermal gradient over the Arctic is probably larger than that of the mid-latitude SST gradient, it is logical to assume that the sea-ice-induced cyclone developing mechanism, such as shown in the present study, is not unusual over the Arctic region.

Local evaporation and moisture convergence are important for the formation and maintenance of atmospheric rivers [Dacre et al. 2015]. There could be a positive feedback link through which Siberian atmospheric rivers could intensify a cyclone and the associated mid-tropospheric poleward heat transport; the intensified cyclone could then further strengthen the atmospheric rivers. Recently, the water vapour and precipitable water over eastern Siberia have been increasing [Serreze et al. 2012], and a positive precipitation trend has also been identified with a change of atmospheric circulation to cyclonic over the northern Eurasia [Fujinami et al. 2016, Hiyama et al. 2016]. The increased humidity of the land surface due to the increase in summer precipitation because of cyclone activity also contributes to further warming and wetting in the active layer of the permafrost [Iijima et al. 2016]. The proposed concept of Siberian atmospheric rivers might link changes in hydrological regimes in Siberia with warming of the Arctic mid-tropospheric temperature. Our statistical analysis (although the statistical significance was weak) implies that the recent Arctic mid-tropospheric temperature increase is likely due to warming caused by Siberian atmospheric

rivers, but we cannot claim that the relationship is robust. Finally we emphasize that our proposed concept includes individual arctic warming mechanisms as a view from a land-ocean-atmosphere interactive system.

2.5 Figures

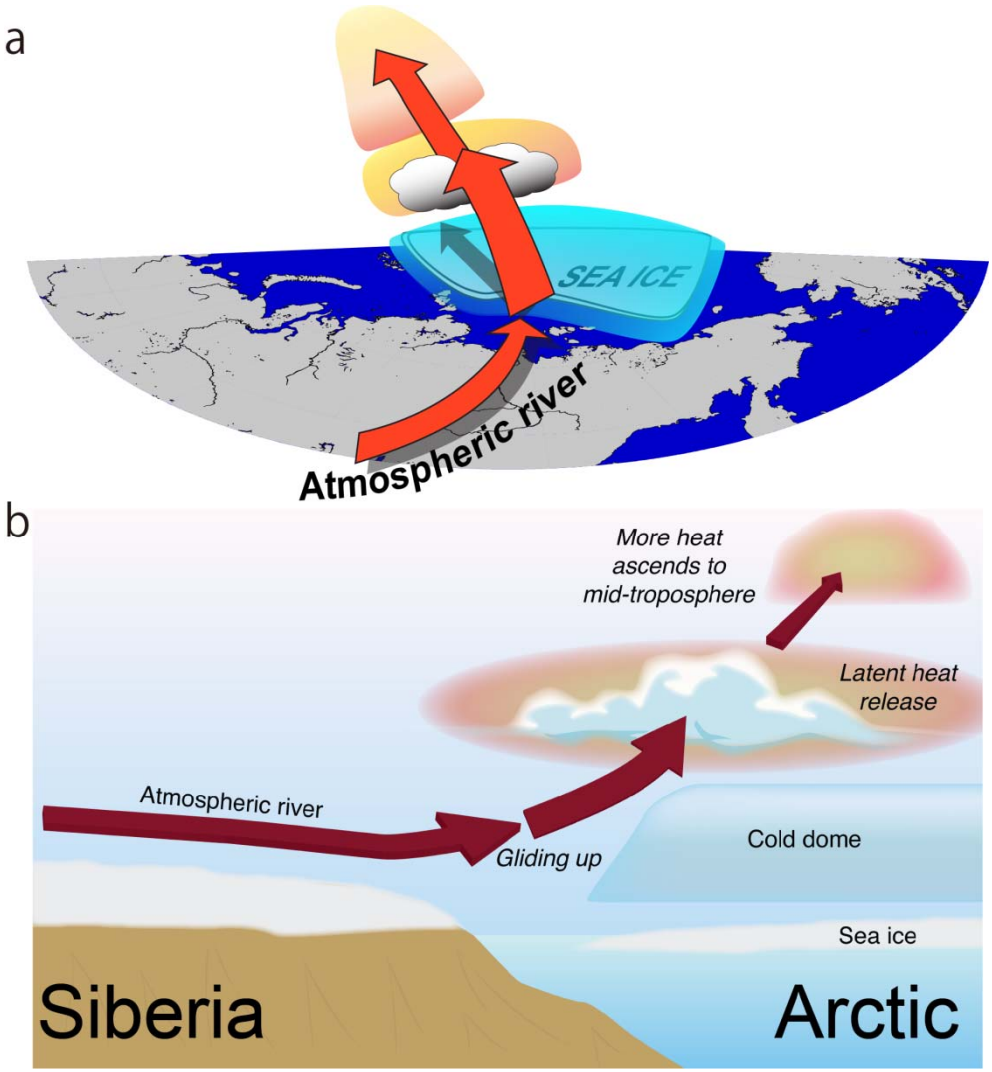

FIG. 2.1. Schematics of tropospheric Arctic heating through the upward glide of Siberian atmospheric river. a) Atmospheric rivers are river-style moisture flows from Siberia into the Arctic. The river-like glide upward and poleward over the cold air dome overlying the sea ice is shown. b) Same as a) but for viewed from the side. The Generic Mapping Tools (GMT) with version 4.5.6 (http://gmt.soest.hawaii.edu) was used to generate the map in this figure.

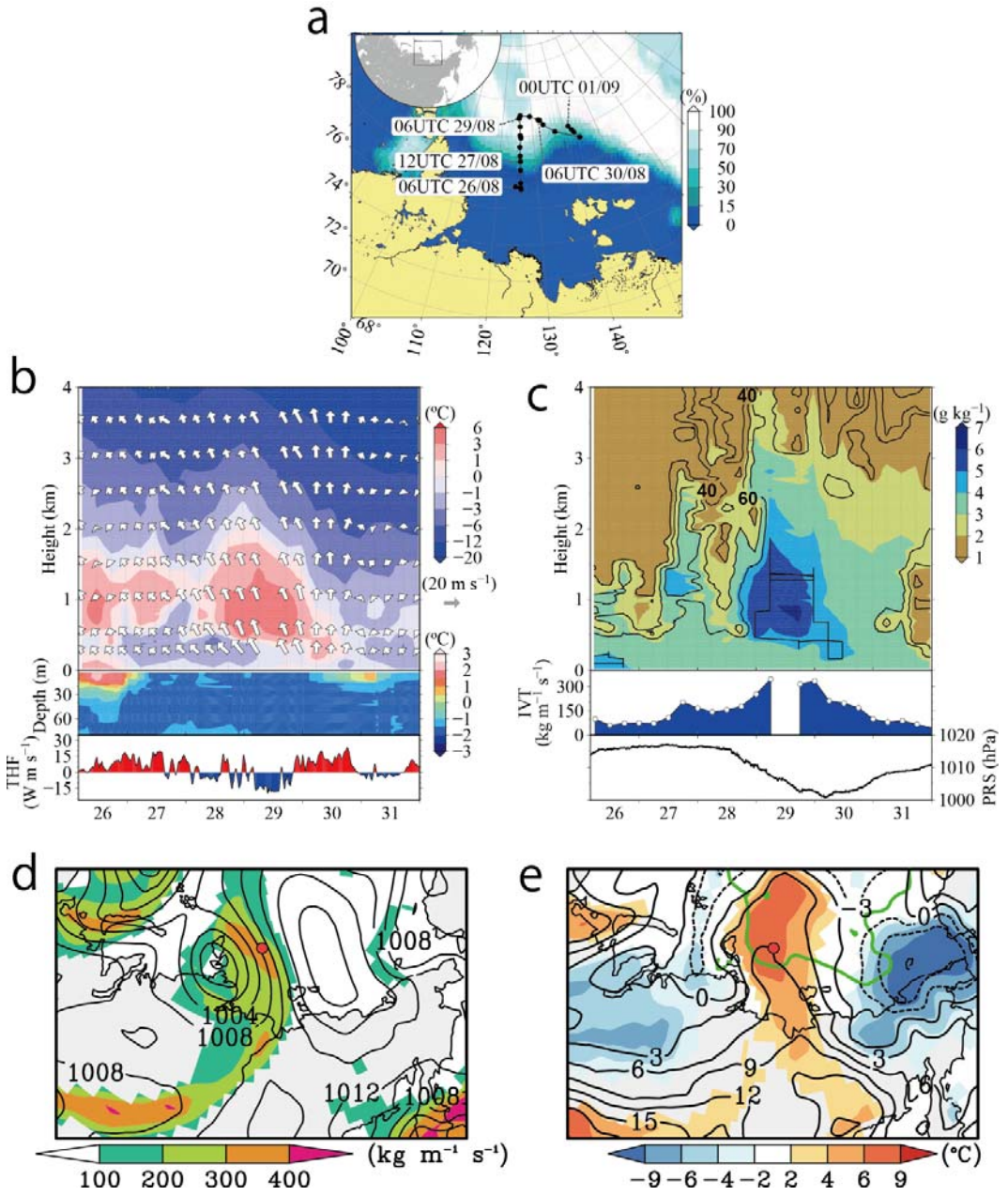

FIG. 2.2. Map of the observational area and the atmospheric-oceanic vertical time section during the whole observation period, and synoptic scale atmospheric conditions at 06 UTC on 29 August. a) Map of the observational area with time-averaged sea ice concentration (colour, %) and sounding points (circles) during the radiosonde observational period. b) The atmospheric height-time section indicates temperature (°C) and horizontal wind vectors (m s^{-1}). The oceanic depth-time section depicted ocean temperature (°C) and the upward

turbulent sensible and latent heat fluxes from the surface (W m^{-2} s^{-1}) are shown middle and bottom panel, respectively. c) The top panel is same as (b) but for specific humidity (colour, g kg^{-1}) and relative humidity (contours, %). The contour interval is 20 %. The integrated water vapour transport (IVT) in the atmosphere was estimated to be between 1000 hPa and 300 hPa (kg m^{-1} s^{-1}) and is presented in the bottom panel of the atmospheric plot. The surface pressure is also shown in bottom panel. d) The map of sea level pressure (contour), IVT (colour). Colours are masked over 100 kg m^{-1} s^{-1}. The contour interval is 4 hPa. Red circle indicates the sounding point at 06 UTC on 29 August. e) Same as (d) but for the temperature at 900 hPa (contours, °C) and the anomaly from the climatological values (colour, °C). The contour interval is 3 °C. The time-averaged ice edge defined by 50 % sea ice concentration for the observation period is depicted using a green line. (d) and (e) use ERA-Interim. The Generic Mapping Tools (GMT) with version 4.5.6 (http://gmt.soest.hawaii.edu) and the Grid Analysis and Display System (GrADS) with version 2.1.a3 (http://cola.gmu.edu/grads) were used to generate the map in this figure.

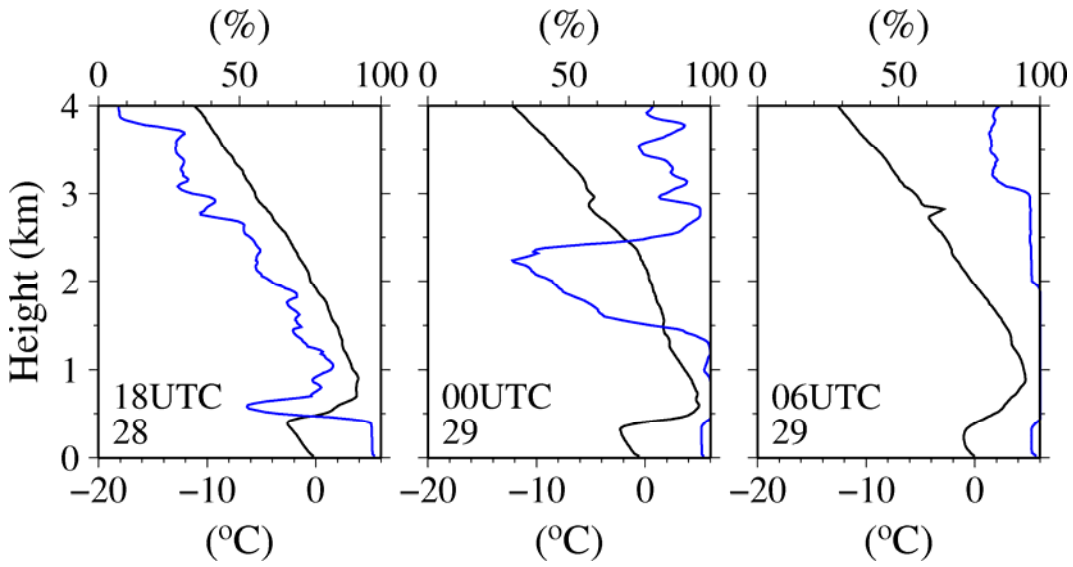

FIG. 2.3. Vertical profiles of observed temperatures and relative humidity. Temperature and relative humidity are shown as black and blue lines, respectively. The left, middle and right panels represent the time evolution of non-trapped cloud tops using strong temperature inversions.

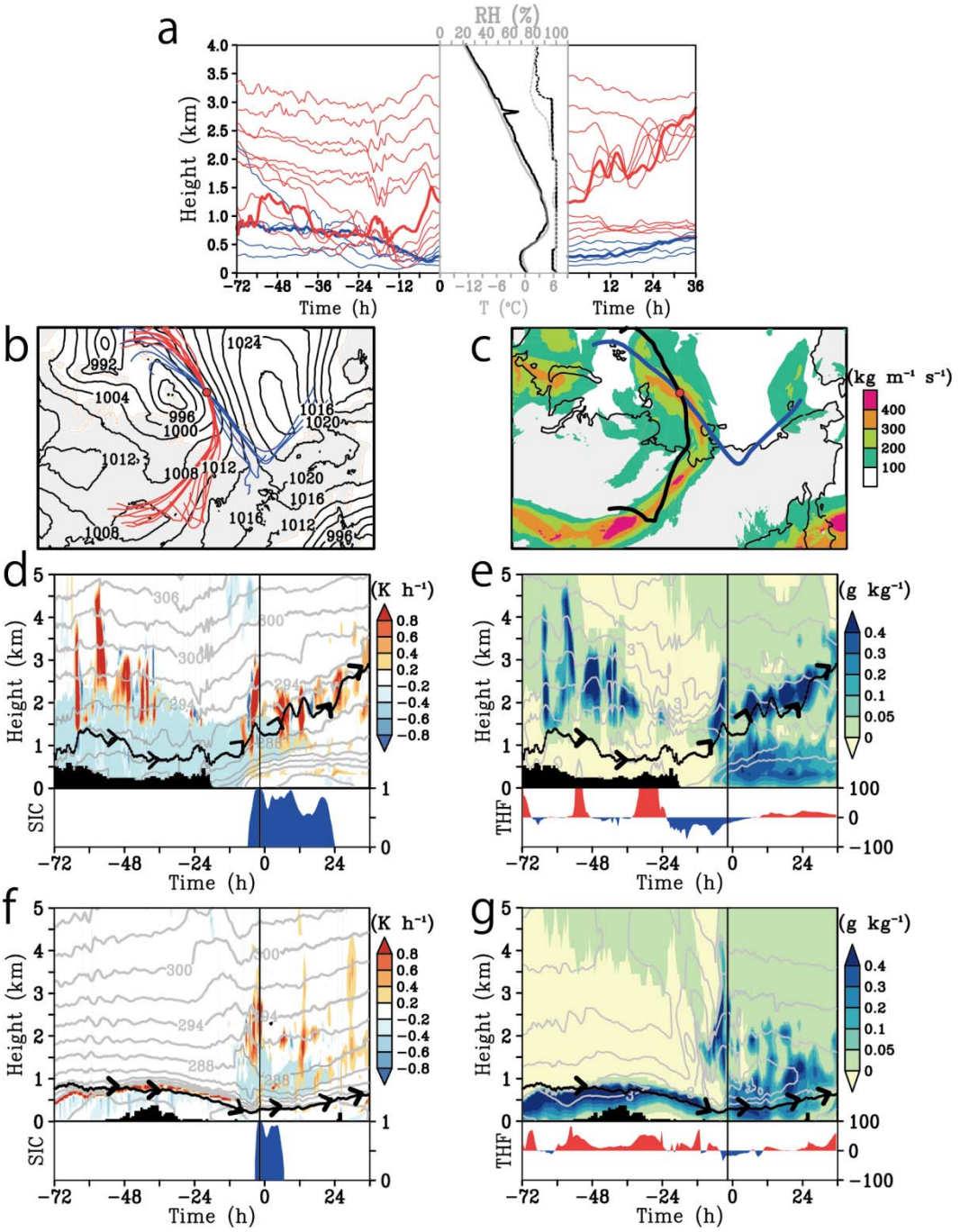

FIG. 2.4. Model simulated backward and forward trajectories of air parcels initiated over the sounding point and time vertical section of the air trajectory along the Siberian route and Chukchi Sea route. a) Time series of vertical displacements of air parcels over previous (to the sounding point) 72 hours and next 36 hours (after the sounding point). The Siberian route and the Chukchi Sea route are shown as red and blue lines respectively. Bold line indicates the air

parcels initiated 1.2 and 0.3 km height. The middle panel indicates the observed (black) and simulated (grey) vertical profiles of temperature (solid line, °C) and relative humidity (dotted line, %) over the sounding point. b) The map of sea level pressures (contours, hPa) at the starting time of the trajectories. The contour interval is 4 hPa. The red and blue lines indicate the horizontal pathways of the Siberian route and Chukchi Sea route, respectively. The red circle indicates the location of sounding. c) Same as (b) but for IVT values. The black and blue lines indicate horizontal pathways of the trajectories initiated at 1.2 km and 0.3 km, respectively. d) Time vertical section along the black line in Figure 2.4c in terms of its potential temperature (grey contours, K), condensation heating rate (colour, K h^{-1}), and specific humidity over 5 g kg^{-1} (blue mark). The contour interval is 3 K. The black lines indicate the trajectories of air parcels, and the black mask shows the topography. The bottom panel indicates the sea ice concentration (10^2 %). e) Same as d) but for the cloud water and ice mixing ratio (colour, g kg^{-1}) and specific humidity (contour, g kg^{-1}). The contour interval is 1 g kg^{-1}. The bottom panel indicates the turbulent sensible and latent heat fluxes from the surface (W m^{-2}). f) and g) are same as d) and e) but along the blue line in Figure 2.4c.The Grid Analysis and Display System (GrADS) with version 2.1.a3 (http://cola.gmu.edu/grads) was used to generate the map in this figure.

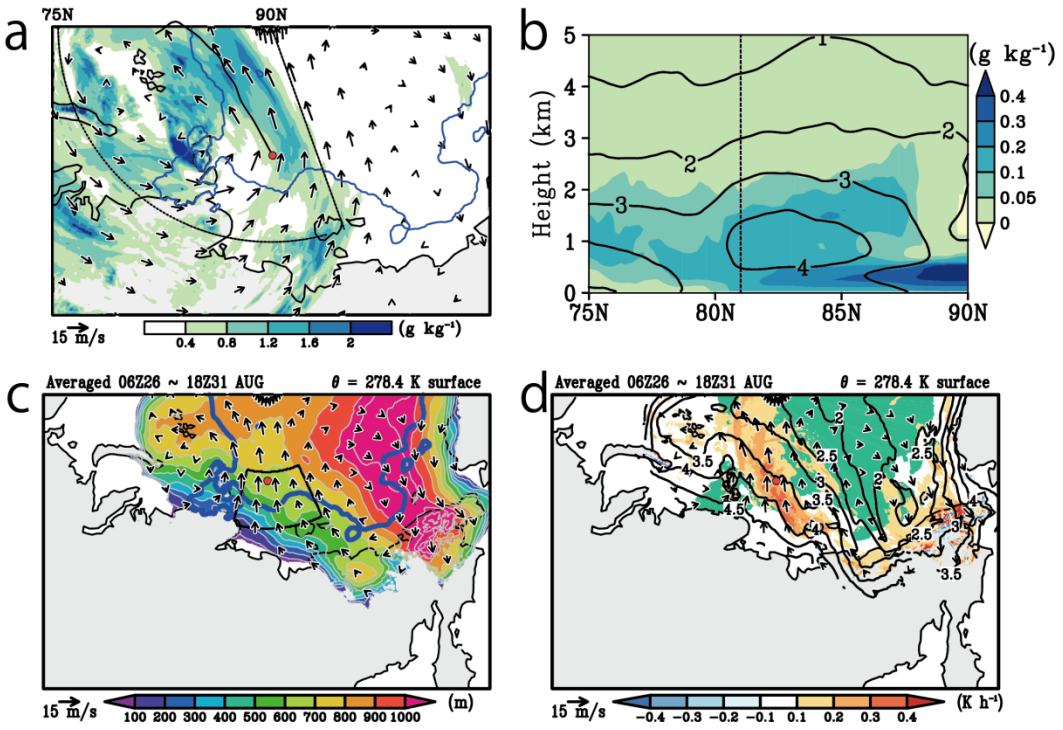

FIG. 2.5. Model simulated map of the 24 hours mean cloud water and ice mixing ratio with horizontal wind and those of the latitude-vertical section averaged from 35 ° E to 140 ° E, and the averaged map of cold air dome characterized by the isentropic surface of 278.4 K. a) The temporary averaged map of the vertically integrated cloud water and ice mixing ratio (colour, g kg^{-1}) and vertically averaged horizontal wind (vector, m s^{-1}). The vertical integrating and averaging spans from 1.2 km to 4 km, and the temporal averaging period spans from 08 UTC on 29 to 08 UTC on 30 August, which is 24 hours from trajectory started time. The blue lines indicate the sea ice concentration of 10 %. The large sector with dotted lines is the region used to estimate Figure 2.5b. b) Temporary averaged latitude-vertical section averaged from 35 ° E to 140 ° E in terms of cloud water and ice mixing ratio (colour, g kg^{-1}) and specific humidity (contours, g kg^{-1}). The temporal averaging period span is same as (a). The contour interval is 1 g kg^{-1}. The black

dots line indicates the latitude of sounding at 06 UTC on 29 August. c) The map of height (colour and contours, m) and horizontal wind (vector, m s^{-1}) along the simulated isentropic surface of 278.4 K averaged from 06 UTC on 26 to 18 UTC on 31 August. The contour interval is 100 m. The blue line indicates the sea ice concentration of 10 %, and the black line shows the area of the Laptev Sea. d) Same as c) but for the condensation heating (colour, K h^{-1}) and specific humidity (contours, g kg^{-1}). The contour interval is 0.5 g kg^{-1}. The green mask indicates the sea ice defined by the sea ice concentration over 10 %. The red circle in (a), (c) and (e) indicates the location of sounding at 06 UTC on 29 August. The Grid Analysis and Display System (GrADS) with version 2.1.a3 (http://cola.gmu.edu/grads) was used to generate the map in this figure.

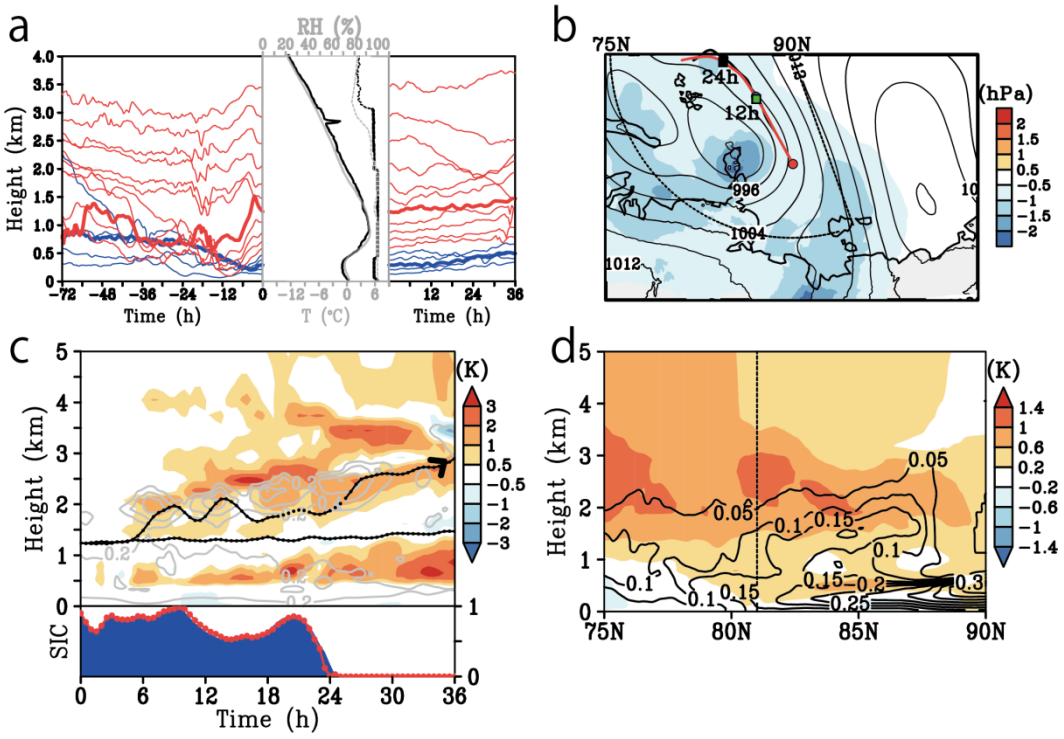

FIG. 2.6. Model-simulated back and forward trajectories of the DRY, and the difference of the averaged sea level pressure and potential temperature fields between the CTL and DRY. a) Same as Figure 2.4a but for DRY. b) Temporally averaged sea level pressure in CTL (contour, hPa) and differences from those of DRY (colour, hPa). Negative value indicates that CTL lower than DRY. The temporal averaging period is from 08 UTC on 29 to 08 UTC on 30 August. The contour interval is 2 hPa. The red circle indicates the location of sounding at 06 UTC on 29 August. Black and red line shows the horizontal pathways of forward trajectories of the CTL and DRY respectively. Green and black squares indicate the location of air parcels at 12 and 24 hours later from trajectory started time. The large sector with dotted lines is the region used to estimate Figure 2.6d. c) Time vertical section along the forward trajectories initiated 1.2 km in terms of its difference of potential temperature between CTL and DRY (colour, K) and cloud water and ice mixing ratio in CTL (grey contours, K). Positive value of the

difference indicates that CTL warmer than DRY. The contour interval is 0.2 g kg^{-1}. Black dots lines show the trajectory of air parcel in CTL and Dry respectively. The bottom panel indicates the sea ice concentration in CTL (blue mask, 10^2 %) and DRY (red line, 10^2 %). d) Same as Figure 2.5b but for the difference of potential temperature between CTL and DRY (colour, K) and cloud water and ice mixing ratio in CTL (contour, g kg^{-1}). Positive value of the difference indicates that CTL warmer than DRY. The Grid Analysis and Display System (GrADS) with version 2.1.a3 (http://cola.gmu.edu/grads) was used to generate the map in this figure.

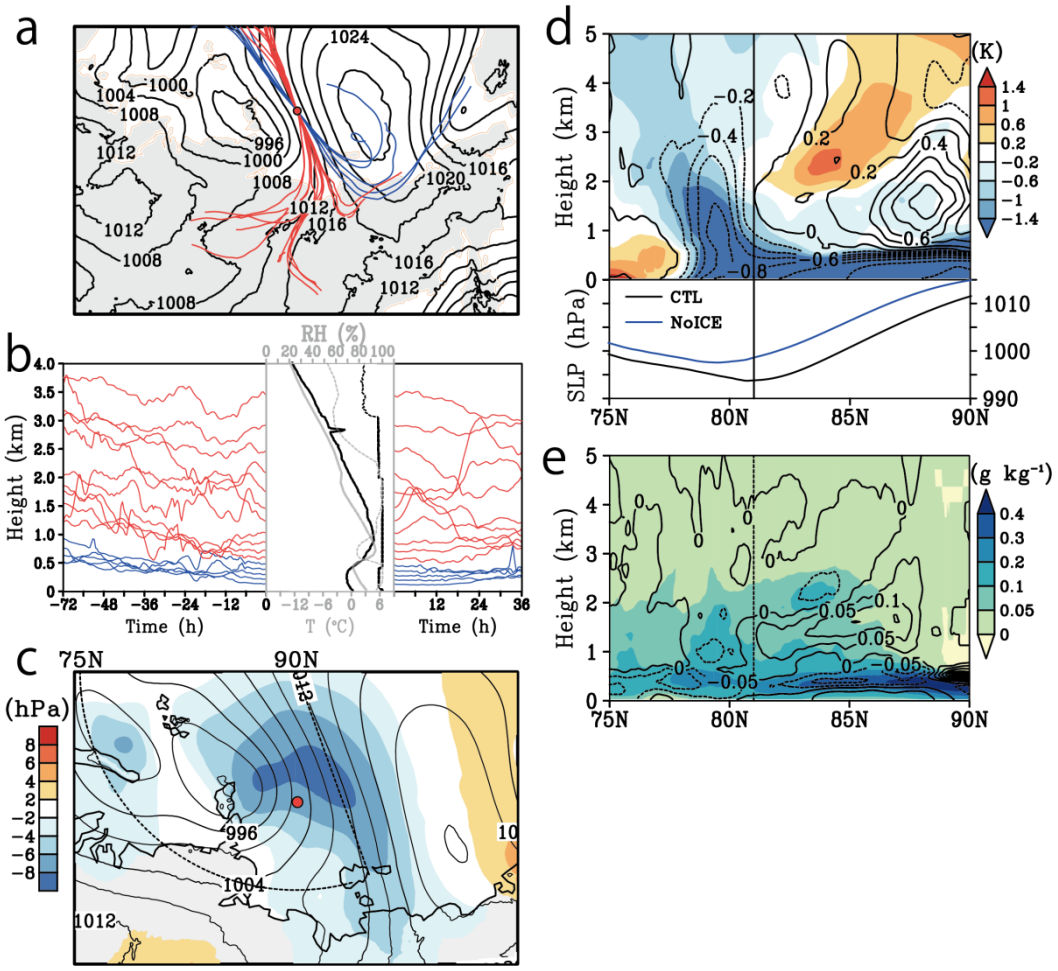

FIG. 2.7. Model-simulated back and forward trajectories of the NoICE, and the difference of the averaged sea level pressure, potential temperature, and water vapour fields between the CTL and NoICE. (a) and (b), same as Figure 2.4a and 2.3b, respectively, but for NoICE. c) Same as Figure 2.6b but for the differences between CTL and NoICE . The negative values indicate that CTL is lower than NoICE. d) Top panel is same as Figure 2.5b but for the difference of potential temperature (colour, K) and specific humidity (contours, g kg^{-1}) between CTL and those of NoICE. Positive value indicates that CTL is warmer and wetter than NoICE. Bottom panel shows the sea level pressure in CTL and NoICE respectively. e) Same as Figure 2.5b but for the cloud water and ice mixing ratio in NoICE (colour, g kg^{-1}) and the difference between those of CTL and NoICE

(contour, g kg^{-1}). Positive value indicates that CTL is cloudier than NoICE. The Grid Analysis and Display System (GrADS) with version 2.1.a3 (http://cola.gmu.edu/grads) was used to generate the maps in this figure.

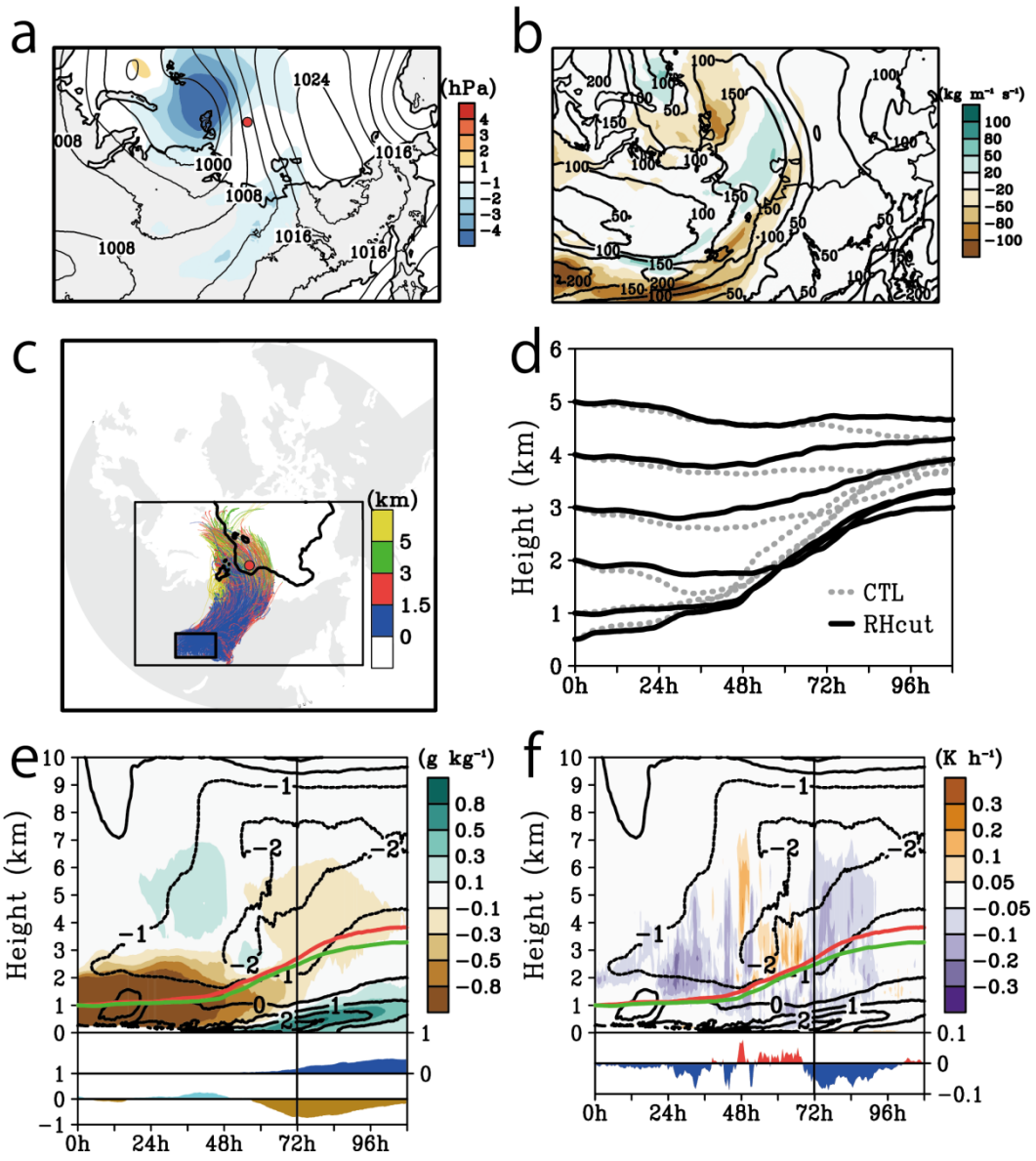

FIG. 2.8. Model-simulated synoptic atmospheric conditions, forward trajectories initiated around central Siberia and the difference in the averaged vertical time section along the trajectories between the CTL and RHcut. a) Same as Figure 2.6b but for the differences between CTL and RHcut (colour, hPa) averaged from 08 UTC on 28 to 20 UTC on 30 August, which is between 48 and 108 hours from trajectory started time. The negative values indicate that CTL is lower than RHcut. b) Map of IVT in the RH (contour) and the difference between those in CTL and

RHcut averaged in same period of (a). Negative values indicate that the RHcut is drier than the CTL. The contour interval is 50 kg m^{-1} s^{-1} c) Horizontal pathway of the 108 hour projections in the RHcut for five hundred air parcels originating at an altitude of 1 km in the small black square. Colour indicates the height of each parcel. d) The composite vertical displacements of the trajectories of the parcels released at 0.5, 1, 2, 3, 4, and 5 km in the CTL (dashed line) and RHcut (solid line). e) Difference in the specific humidity (colour) and temperature (contour) between RHcut and CTL. Negative values indicate that the RHcut is drier and cooler than the CTL. The panel represents a composite Lagrangian vertical time section along the forward trajectory of a parcel released at 1 km. The sea ice concentration in the CTL and the differences of the precipitable waters from 750 hPa to 300 hPa in the RHcut from those in the CTL (bottom panel) are shown in the middle and bottom panels, respectively. f) Same as (e) but for condensation heating scenarios (colour, K h^{-1}) and the difference of the vertically integrated condensation heating from 750 hPa to 300 hPa is shown in the bottom panel. Negative values indicate that the RHcut has less heat than the CTL. The red and green lines in (e) and (f) show the composite vertical displacement of the air parcels of CTL and RHcut, respectively. The Grid Analysis and Display System (GrADS) with version 2.1.a3 (http://cola.gmu.edu/grads) was used to generate the map in this figure.

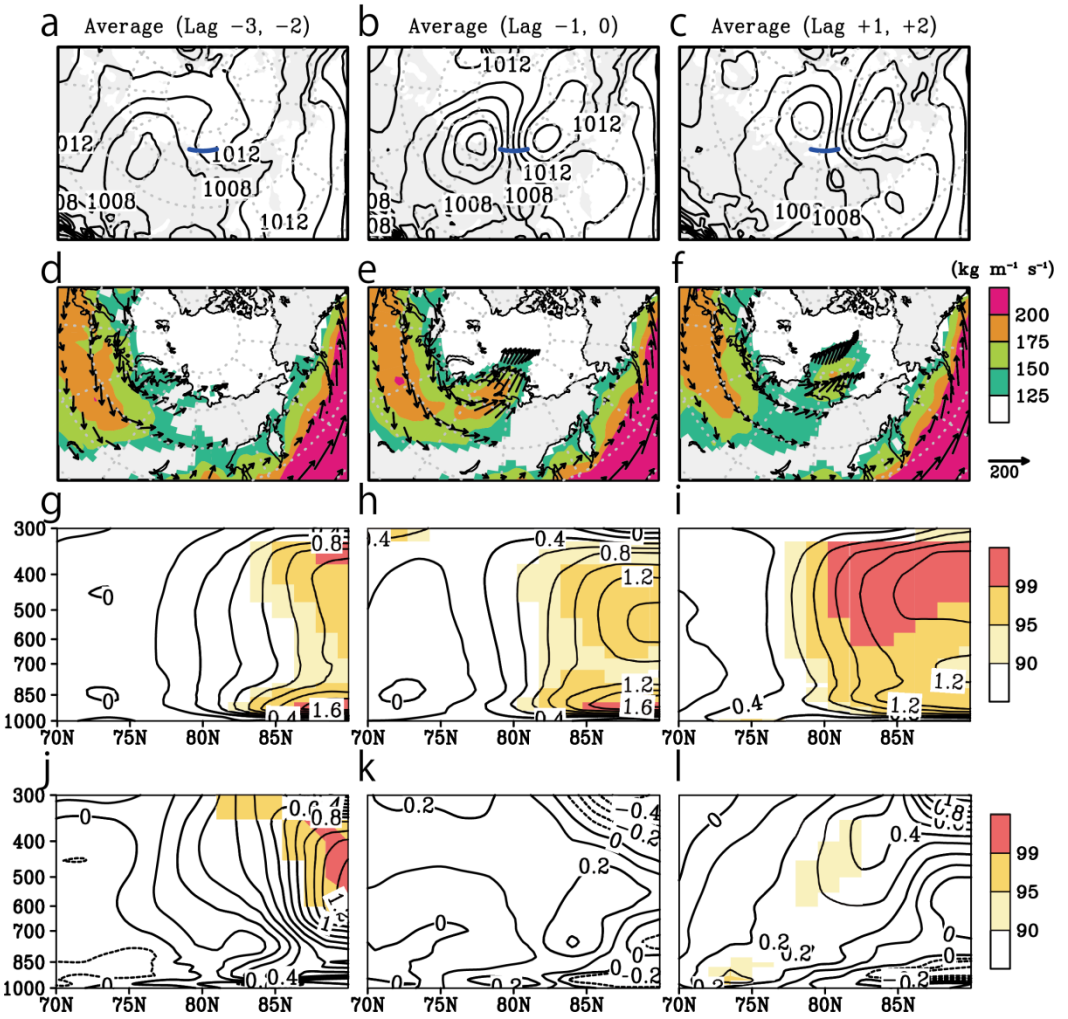

FIG. 2.9. Lag composite map and, the anomaly of zonal mean polar cap temperature and that of tendencies between negative and positive ice year in the Laptev Sea associated with the Siberian atmospheric rivers events. (a) The composite map of sea level pressure (hPa) with 2 days lead from the day of the Siberian atmospheric rivers passed through the blue line at 75° N. The contour interval is 2 hPa. (b) same as (a) but for the day of Siberian atmospheric rivers passed the blue line. (c) same as (a) but for 2 days lag. (d), (e), and (f) are same as (a), (b), and (c) but for the IVT (colour in kg m^{-1} s^{-1}) and vertical integrate moisture flux (vector). (g), (h), and (i) are same as (a), (b), and (c) but for the pressure-latitude section about the anomaly for zonal mean temperature (contour, K) between negative and positive ice year. The contour intervals is 0.2 K. The

colour indicates the confidence level of the anomaly between negative and positive ice year. (j), (k), and (l) are same as (g), (h), and (i) but for the temperature tendency (contours, K $2day^{-1}$). The Grid Analysis and Display System (GrADS) with version 2.1.a3 (http://cola.gmu.edu/grads) was used to generate the map in this figure.

2.6 References

Alexeev, V. A., P. L. Langen and J. R. Bates, 2005: Polar amplification of surface warming on an aquaplanet in “ghost forcing” experiments without sea ice feedbacks. *Clim. Dyn.*, **24**, 655–666

Alexeev, V. A., J. E. Walsh, V. V. Ivanov, 2017: Semenov, V. A. and Smirnov A. V., Warming in the Nordic Seas, North Atlantic storms and thinning Arctic sea ice. *Environ. Res. Lett.*, **12**, 84011

Baggett, C., S. Lee, and S. Feldstein, 2016: An Investigation of the Presence of Atmospheric Rivers over the North Pacific during Planetary-Scale Wave Life Cycles and Their Role in Arctic Warming. *J. Atmos. Sci.*, **73**, 4329–4347

Bao, J.-W., S. A. Michelson, P. J. Neiman, F. M. Ralph and J. M. Wilczak, 2006: Interpretation of Enhanced Integrated Water Vapor Bands Associated with Extratropical Cyclones, Their Formation and Connection to Tropical Moisture. *Mon. Weather Rev.*, **134**, 1063–1080

Boettcher, M., and H. Wernli, 2013: A 10-yr Climatology of Diabatic Rossby Waves in the Northern Hemisphere. *Mon. Weather Rev.*, **141**, 1139–1154

Chung, C. E., and P. Räisänen, 2011: Origin of the Arctic warming in climate models. *Geophys. Res. Lett.*, **38**

Comiso, J. C., 2015: Bootstrap Sea Ice Concentrations from Nimbus-7 SMMR and DMSP SSM/I-SSMIS, Version 2 (NASA National Snow and Ice Data Center Distributed Active Archive Center, 2015).

Dacre, H. F., P. A. Clark, O. Martinez-Alvarado, M. A. Stringer, and D. A. Lavers, 2015: How Do Atmospheric Rivers Form?, *Bull. Am. Meteorol. Soc.*, **96**, 1243–1255

Dee, D. et al., 2011: The era-interim reanalysis: configuration and performance of the data assimilation system. *Q. J. R. Meteorol. Soc.,* **137**, 553–597

Fujinami, H., T. Yasunari, and T. Watanabe, 2016: Trend and interannual variation in summer precipitation in eastern Siberia in recent decades. *Int. J. Climatol.*, **36**, 355–368

Graversen, R. G., and M. Wang, 2009: Polar amplification in a coupled climate model with locked albedo. *Clim. Dyn.*, **33**, 629–643

Graversen, R. G., T. Mauritsen, M. Tjernström, E. Källén, and G. Svensson, 2008: Vertical structure of recent Arctic warming. *Nature*, **451**, 53–56

Graversen, R. G., and M. Burtu, 2016: Arctic amplification enhanced by latent energy transport of atmospheric planetary waves. *Q. J. R. Meteorol. Soc.*, **142**

Gimeno, L., R. Nieto, M. VÃzquez, and D. A. Lavers, 2014: Atmospheric rivers: a mini-review. *Front. Earth Sci.,* **2**, 1–6

Hines, K. M. et al., Sea ice enhancements to polar WRF*. *Mont. Weather Rev.,* **143**, 2363–2385

Hirata, H., R. Kawamura, M. Kato, and T. Shinoda, 2016: Response of rapidly developing extratropical cyclones to sea surface temperature variations over the western Kuroshio-Oyashio confluence region. *J. Geophys. Res. Atmos.*, **121**, 3843–3858

Hiyama, T., H. Fujinami, H. Kanamori, T. Ishige, and K. Oshima, 2016: Recent interdecadal changes in the interannual variability of precipitation and atmospheric circulation over northern Eurasia. *Environ. Res. Lett.*, **11**, 65001

Inoue, J., M. E. Hori, T. Enomoto, and T. Kikuchi, 2011: Intercomparison of surface heat transfer near the Arctic marginal ice zone for multiple reanalyses: a case study of september 2009. *SOLA*, **7**, 57-60

Iijima, Y., T. Nakamura, H. Park, Y. Tachibana, and A. N. Fedorov, 2016: Enhancement of Arctic storm activity in relation to permafrost degradation in eastern Siberia. *Int. J. Climatol.*, **36**, 4265–4275

Jakobson, E., and T. Vihma, 2010: Atmospheric moisture budget in the Arctic based on the ERA-40 reanalysis. *Int. J. Climatol.*, **30**, 2175–2194

Laliberté, F., and P. J. Kushner, 2013: Isentropic constraints by midlatitude surface warming on the Arctic midtroposphere. *Geophys. Res. Lett.*, **40**, 606–611

Lavers, D. A., G. Villarini, R. P. Allan, E. F. Wood, and A. J. Wade, 2012: The detection of atmospheric rivers in atmospheric reanalyses and their links to British winter floods and the large-scale climatic circulation. *J. Geophys. Res. Atmos.*, **117**

Liu, C., and E. A. Barnes, 2015: Extreme moisture transport into the Arctic linked to Rossby wave breaking. *J. Geophys. Res. Atmos.*, **120**, 3774–3788

Minobe, S., A. Kuwano-Yoshida, N. Komori, S.-P. Xie, and R. J. Small, 2008: Influence of the Gulf Stream on the troposphere. *Nature*, **452**, 206–209

Neff, W., G. P. Compo, F. M. Ralph, and M. D. Shupe, 2014: Continental heat anomalies and the extreme melting of the Greenland ice surface in 2012 and 1889. *J. Geophys. Res. Atmos.*, **119**, 6520–6536

Neiman, P. J., F. M. Ralph, G. A. Wick, J. D. Lundquist, and M. D. Dettinger, 2008: Meteorological Characteristics and Overland Precipitation Impacts of Atmospheric Rivers Affecting the West Coast of North America Based on Eight Years of SSM/I Satellite Observations. *J. Hydrometeorol.*, **9**, 22–47

Oshima, K., and K. Yamazaki, 2004: Seasonal Variation of Moisture Transport in Polar Regions and the Relation with Annular Modes. *Polar Meteorol. Glaciol.*, **18**, 1–26

Parker, D. J., and A. J. Thorpe, 1995: Conditional Convective Heating in a Baroclinic Atmosphere: A Model of Convective Frontogenesis. *J. Atmos. Sci.*, **52**, 1699–1711

Ralph, F. M., P. J. Neiman, and R. Rotunno, 2005: Dropsonde Observations in Low-Level Jets over the Northeastern Pacific Ocean from CALJET-1998 and PACJET-2001: Mean Vertical-Profile and Atmospheric-River Characteristics. *Mon. Weather Rev.*, **133**

Ralph, F. M., P. J. Neiman, and G. A. Wick, 2004: Satellite and CALJET Aircraft Observations of Atmospheric Rivers over the Eastern North Pacific Ocean during the Winter of 1997/98. *Mon. Weather Rev.*, **132**, 1721–1745

Reynolds, R. W. et al., 2007: Daily high-resolution-blended analyses for sea surface temperature. *J. Clim.,* **20**, 5473–5496

Screen, J. A., C. Deser, and I. Simmonds, 2012: Local and remote controls on observed Arctic warming, *Geophys. Res. Lett.*, **39**

Screen, J. A., and I. Simmonds, 2010: The central role of diminishing sea ice in recent Arctic temperature amplification. *Nature*, **464**, 1334–1337

Serreze, M. C., and J. A. Francis, 2006: The Arctic Amplification Debate. *Clim. Change* **76**, 241–264

Serreze, M. C., and R. G. Barry, 2011: Processes and impacts of Arctic amplification: a research synthesis. *Glob. Planet. Change* **77**, 85–96

Serreze, M. C., A. P. Barrett, and J. Stroeve, 2012: Recent changes in tropospheric water vapor over the Arctic as assessed from radiosondes and atmospheric reanalyses. *J. Geophys. Res. Atmos.*, **117**

Serreze, M. C., A. P. Barrett, J. C. Stroeve, D. N. Kindig, and M. M. Holland, 2009: The emergence of surface-based Arctic amplification, *The Cryospher*, **3**, 11–19

Skamarock, W. C. et al., 2005: A Description of the Advanced Research WRF Version 3. Vol. 113 (NCAR Technical Note NCAR/TN-468+STR).

Tjernström, M., C. Leck, P. O. G. Persson, M. L. Jensen, S. P. Oncley, and A. Targino, 2004: The Summertime Arctic Atmosphere: Meteorological Measurements during the Arctic Ocean Experiment 2001. *Bull. Am. Meteorol. Soc.*, **85**, 1305–1321

Tjernström, M., 2005: The Summer Arctic Boundary Layer during the Arctic Ocean Experiment 2001 (AOE-2001). *Boundary-Layer Meteorol.*, **117**, 5–36

Tjernström, M. et al., 2012: Meteorological conditions in the central Arctic summer during the Arctic Summer Cloud Ocean Study (ASCOS). *Atmos. Chem. Phys.*, **12**, 6863–6889

Tjernström, M. et al., 2015: Warm-air advection, air mass transformation and fog causes rapid ice melt, *Geophys. Res. Lett.*, **42**, 5594–5602

Vázquez, M., R. Nieto, A. Drumond, and L. Gimeno, 2016: Moisture transport into the Arctic: Source-receptor relationships and the roles of atmospheric circulation and evaporation. *J. Geophys. Res. Atmos.*, **121**, 13493-13509

Vihma, T., 2014: Effects of Arctic Sea Ice Decline on Weather and Climate: A Review. *Surv. Geophys.*, **35**, 1175–1214

Woods, C., R. Caballero, and G. Svensson, 2013: Large-scale circulation associated with moisture intrusions into the Arctic during winter. *Geophys. Res. Lett.*, **40**, 4717–4721

Zhu, Y., and R. E. Newell, 1998: A Proposed Algorithm for Moisture Fluxes from Atmospheric Rivers. Mon. *Weather Rev.*, **126**, 725–735

Yang, X.-Y., J. C. Fyfe, and G. M. Flato, 2010: The role of poleward energy transport in Arctic temperature evolution, *Geophys. Res. Lett.*, **37**

General conclusion

This thesis demonstrated the importance of in-situ atmospheric upper air observation above locally confined surface conditions characterized by their large horizontal gradient. In Chapter 1, the in-situ observation highlighted the structure of local wind called as “Suzuka-oroshi”, which has two flow regimes of downslope wind and low-level jet respectively. The multiple sounding method proposed in this study permitted us to distinguish two flow regimes. The method is able to simultaneously capture the horizontal-vertical atmospheric structure between the windward and leeward side of a steep mountain. A regional numerical model well reproduced the observed downslope wind regime. Unfortunately, the regional modeling failed to replicate the low-level jet regime. The observation limited to depict the detail structure of this regime. Statistical analyses, however, provided us an insight of Suzuka-oroshi. If a single site observation had operated at just windward or leeward side, the existence of low-level jet could not have been identified.

In Chapter 2, the in-situ observation cooperated with a numerical model revealed an upgliding process of atmospheric rivers forced by cold air dome over sea ice. Moreover this study proposed that the upgliding process of atmospheric rivers could contribute to heating the Arctic mid-troposphere as a part of a land-atmospheric-ocean interacted system. These results imply local boundary conditions affects large-scale atmospheric fields. The evidence of the interaction between atmosphere and sea ice over the marginal ice zone in the Arctic had not been clear owing to the lack of measurement until our ice breaker observation, thus the observational data using this study is especially valuable. The in-situ observational data highly promised the validity of the numerical model that we

executed. Thus, without the in-situ observation, the concept of the upgliding process and the interacting system could have never been built up.

Although both case studies in Chapter 1 and 2 addressed different phenomena, different scales and different locations, both studies commonly found hidden phenomena driven by locally confined surface conditions that were unresolved by reanalyses or numerical models. To detect these surface-driven atmospheric phenomena accurately, the in-situ observation is absolutely needed. Moreover the finding of the latter case implies the potential impact of local boundary condition to large-scale atmospheric circulations. This suggests that increase of the knowledge about local phenomena should deepen the understanding of the climate change. Although the reanalyses and numerical models are useful for the climatic assessment, we must reconsider the importance of small-scale phenomena driven by individual boundary conditions for the formation of large-scale climate.

Acknowledgement

I am grateful to Prof. Yoshihiro Tachibana who gave me the chance to participate very interesting observations, and constantly supported and encouraged. I am also grateful to Prof. Sekine, Prof. Matumura, Prof. Sakamoto, Associate Prof. Iijima, Associate Prof. Nishii, and Associate Prof. Manda of Mie University, and Prof. Hiyama of Nagoya University, Dr. Saito of Meteorological Reseach Insititure, Prof. Vladimir Alexeev of University of Alaska and Dr. Irena Repina for fruitful discussion. I thank Mr. Yuji Yamada and the employees of Aoyama-kogen Wind Farm Co., Ltd., for their cooperation and the use of their observatory at Mt.Kasatori, without which I could not have made the observations in chapter 1. I also thank the staff of the Experimental Farm of Mie University and the Iga Research Institute of Mie University, who made their facilities available as observational points. The assistance of numerous undergraduate and graduate students of the Earth System Science Course in Mie University was crucial for making these demanding observations. Discussion with the students were also suggestive. I also thank the crew members of the R/V icebreaker, Akademik Fedorov, and all the participants in NABOS campaign for their assistance. I also thank the crew members of the R/V Seisui of Mie University. R/V Seisui also took part in Suzuka-Oroshi observation along with the land observatories. Unfortunately, I could not include the data measured by R/V Seisui in the thesis, because strong wind events did occurred when the R/V was in the lee-side ocean.